



# **Development of Directed Energy Deposited NASA HR-1 to Optimize Properties for Liquid Rocket Engine Applications**

*P.S. Chen,<sup>1</sup> C.C Katsarelis,<sup>2</sup> W.M. Medders,<sup>2</sup> P.R. Gradl,<sup>2</sup> and C.H. Su<sup>2</sup>*

*<sup>1</sup>Jacobs ESSCA Group, Huntsville, Alabama*

*<sup>2</sup>Marshall Space Flight Center, Huntsville, Alabama*

## The NASA STI Program...in Profile

The NASA STI Program collects, organizes, provides for archiving, and disseminates NASA's STI. The NASA STI program provides access to the NTRS Registered and its public interface, the NASA Technical Reports Server, thus providing one of the largest collections of aeronautical and space science STI in the world. Results are published in both non-NASA channels and by NASA in the NASA STI Report Series, which includes the following report types:

- **TECHNICAL PUBLICATION.** Reports of completed research or a major significant phase of research that present the results of NASA programs and include extensive data or theoretical analysis. Includes compilations of significant scientific and technical data and information deemed to be of continuing reference value. NASA's counterpart of peer-reviewed formal professional papers but has less stringent limitations on manuscript length and extent of graphic presentations.
- **TECHNICAL MEMORANDUM.** Scientific and technical findings that are preliminary or of specialized interest, e.g., quick release reports, working papers, and bibliographies that contain minimal annotation. Does not contain extensive analysis.
- **CONTRACTOR REPORT.** Scientific and technical findings by NASA-sponsored contractors and grantees.
- **CONFERENCE PUBLICATION.** Collected papers from scientific and technical conferences, symposia, seminars, or other meetings sponsored or cosponsored by NASA.
- **SPECIAL PUBLICATION.** Scientific, technical, or historical information from NASA programs, projects, and mission, often concerned with subjects having substantial public interest.
- **TECHNICAL TRANSLATION.** English-language translations of foreign scientific and technical material pertinent to NASA's mission.

Specialized services also include organizing and publishing research results, distributing specialized research announcements and feeds, providing information desk and personal search support, and enabling data exchange services.

For more information about the NASA STI program, see the following:

- Access the NASA STI program home page at <http://www.sti.nasa.gov>
- Help desk contact information:

<https://www.sti.nasa.gov/sti-contact-form/> and select the "General" help request type.



# **Development of Directed Energy Deposited NASA HR-1 to Optimize Properties for Liquid Rocket Engine Applications**

*P.S. Chen,<sup>1</sup> C.C Katsarelis,<sup>2</sup> W.M. Medders,<sup>2</sup> P.R. Gradl,<sup>2</sup> and C.H. Su<sup>2</sup>*

*<sup>1</sup>Jacobs ESSCA Group, Huntsville, Alabama*

*<sup>2</sup>Marshall Space Flight Center, Huntsville, Alabama*

National Aeronautics and  
Space Administration

Marshall Space Flight Center • Huntsville, Alabama 35812

## Acknowledgments

Additive manufacturing and new materials are advancing, and multiple colleagues and organizations are responsible for the development and advancement of NASA HR-1. The authors would like to thank the SLS Liquid Engines Office (LEO) program and Rapid Analysis and Manufacturing Propulsion Technology (RAMPT) project for providing funding and support to develop the processes and advancing this alloy. We would like to thank Johnny Heflin, Keegan Jackson, and John Fikes who provided project leadership. We would like to acknowledge our industry and academia partners including RPM Innovations (RPMI), BeAM, Fraunhofer, Formalloy, and Nima Shamsaei at Auburn University (RAMPT Public Private Partner), and Judy Schneider at University of Alabama Huntsville (UAH) for partnering to develop the process, development and characterizing samples. We would also like to acknowledge various vendors providing feedstock powder including Homogenized Metals Inc (HMI), Praxair, and Powder Alloy Corporation (PAC). Heat treating is a critical operation, and our experts Pat Salvail, Kenny Webster, and David Cole provided outstanding support. We would also like to thank the NASA GRC counterparts including David Ellis, Justin Milner, Chris Kantzios, Ivan Locci, and many others who have helped evaluate and characterize samples. Additionally, we recognize the other engineers who have provided inputs throughout development and testing including Thomas Teasley, Chris Protz, Will Tilson, Brian West, Catherine Bell, Samantha McLeroy, and the many others at MSFC, GRC, and industry.

Available from:

NASA STI Information Desk  
Mail Stop 148  
NASA Langley Research Center  
Hampton, VA 23681–2199, USA  
757–864–9658

This report is also available in electronic form at  
<http://www.sti.nasa.gov>

## TABLE OF CONTENTS

1. INTRODUCTION .....	1
2. PROCEDURES AND METHODS .....	4
2.1. Materials and LP-DED Process .....	4
2.2. Differential Thermal Analysis (DTA) .....	6
2.3. Heat Treatment .....	7
2.4. Metallography and SEM Analysis .....	7
2.5. Mechanical Testing .....	7
3. RESULTS/DISCUSSION .....	10
3.1. Melting and Solidification Characteristics .....	10
3.2. Microstructure Evolution.....	15
3.3. Obtaining an Optimal Balance of Five Important Material Properties Effects of Heat Treatment on Tensile Properties.....	21
3.4. Key Material Properties .....	39
3.5. Hardware Fabrication .....	84
4. CONCLUSIONS .....	87
REFERENCES .....	89

## LIST OF FIGURES

1.	Material being deposited using LP-DED.....	2
2.	A SEM image showing NASA HR-1 powder particle morphology .....	5
3.	(a) An illustration of NASA HR-1 round bar and block fabrication via LP-DED process, (b) round bars with a length of 4 inches and diameter of 0.6 in fabricated at a laser power of 1070 watts, (c) 4 × 4 × 0.04 in single-pass thin panels fabricated with 350 watts laser power.....	6
4.	Geometry of the smooth specimen used for tensile testing in 5 ksi gaseous helium and hydrogen environments at ambient temperature. All dimensions are in inches. The reduced section (C) is required to have slight taper to center, 0.002 Max .....	8
5.	Geometry of the smooth specimen used for LCF testing in 5 ksi gaseous hydrogen environment at ambient temperature. All dimensions are in inches. The reduced section (C) is required to be low stress ground to final diameter .....	9
6.	DTA heating and cooling curves for NASA HR-1 powder. The solidification temperature range for NASA HR-1 powder is determined to be 196 °F .....	11
7.	DTA heating and cooling curves for as-built LP-DED NASA HR-1. The solidification temperature range for as-built LP-DED NASA HR-1 is determined to be 151 °F.....	12
8.	DTA heating and cooling curves for as-built LP-DED JBK-75. The solidification temperature range for as-built LP-DED JBK-75 is determined to be 196 °F .....	13
9.	Solidification behaviour analysis for (a) as-built LP-DED NASA HR-1; and (b) as-built LP-DED JBK-75. LP-DED NASA HR-1 has a more distinct terminal liquid solidification peak at around 2370 °F .....	14
10.	Optical micrographs showing the cross section microstructure of as-built LP-DED NASA HR-1. This single pass LP-DED panel was deposited with a thickness of approximately 3.175 mm (laser power 1070 watts); the build direction is vertically upward.....	16

## LIST OF FIGURES (Continued)

11.	Close-up view of the dendritic structure in an as-built single-pass LP-DEN NASA HR-1 panel. Fine grains are observed on the outer wall due to the rapid solidification .....	16
12.	Effects of Stress relief temperatures on microstructure evolution for single-pass LP-DEN NASA HR-1. The stress relief conditions are (a) as-built, (b) 1700 °F/1.5h, (c) 1800 °F/1.5h, and (d) 1900 °F/1.5h. These single-pass LP-DEN panel was deposited was deposited at a laser power of 1070 watts with a thickness of approximately 3.175 mm .....	17
13.	Macrostructure of a 3.175 mm thick single-pass LP-DEN NASA HR-1 panel after homogenization at 2175 °F/3h. The as-homogenized sample appears free of $\eta$ -phase .....	18
14.	Macrostructure of 3.175 mm thick LP-DEN NASA HR-1 after (a) solution anneal at 1800 °F/1h, and (b) aging treatment at 1325 F/16h. Copious $\eta$ -phase precipitated along some grain boundaries after aging at 1325 °F/16h .....	19
15.	Closeup views of a LP-DEN NASA HR-1 single-pass (3.175 mm thick) panel showing uneven distribution of grain-boundary $\eta$ -phase after being aged at 1325 °F/16h .....	20
16.	Grain-boundary $\eta$ -phase is more evenly distributed in a thin single-pass LP-DEN NASA HR-1 panel (91 mm thick) after being aged at 1325 °F/16h. This 1 mm thick single-pass LP-DEN panel was deposited at a laser power of 350 watts .....	20
17.	(a) The five (5) important material properties and (b) key trades to optimizing for a LRS nozzle application. The original formulation and heat treatment for LP-DEN NASA HR-1 has been optimized to obtain an optimal comprise of these five materials properties .....	23
18.	Md comparison for wrought NASA-HR-1, LP-DEN NASA HR-1 initial formulation, final formulation, wrought A-286, and wrought JBK-75.....	26
19.	Varying degree of recyrstallization occurred when the material was HIPed at 2125 °F after stress relief. These samples were stress relieved at 1700 °F for (a) and (b), 1800 °F for (c) and (d), and 1900 °F for (e) and (f) before HIP .....	28

## LIST OF FIGURES (Continued)

20.	The predicted homogenization kinetic curves for LP-DED NASA HR-1 to reach the residual segregation index ( $\delta$ ) of 0.1. The homogenization time decreases with an increase of the homogenization temperature for the same grain size .....	30
21.	(a) An EDS line scan on an as-built 1.0 mm thick single-pass LP-DED NASA HR-1 panel (built with 350 watts laser power) showing titanium concentration fluctuates intensely between 0 to 10% in some locations. (b) A close-up view of EDS line scan data revealing titanium concentration fluctuates intensely between 0.3 to 8% in many locations .....	31
22.	The evolution of titanium concentration profile for a 1.0 mm thick single-pass LP-DED NASA HR-1 panel (built with 350 watts laser power) after homogenization at (a) 2125 °F/3h, (b) 2125 °F/6h, and (c) 2125 °F/12h .....	33
23.	Precipitation of grain-boundary $\eta$ -phase after (a) solution anneal, (b) aging at 1325 °F/24h, (c) aging at 1300 °F/24h, and (d) aging at 1275 °F/16h.....	35
24.	Overlaid stress-strain curves for the round bar samples (1070 W –0.6' diameter) that have the highest tensile strength from each aging treatment group .....	38
25.	The evolution of post-processing heat treatment for LP-DED NASA HR-1.....	39
26.	Cross-section of as-built LP-DED NASA HR-1 in (a) x-z plane showing melt pool morphologies, (b) x-y plane showing scanning strategy. Close-up view showing microstructure features in x-z plane in (c) as-built condition and (d) fully heat treated condition .....	40
27.	Engineering stress-strain curves of LP-DED NASA HR-1 tensile at (a) -320 °F, (b) ambient air, and (c) 1200 °F. (d) Stressed stress-strain flow behavior is observed in the 2-step aged sample during tensile testing at 1200 °F. Scales are kept in identical ranges from (a) through (c) to illustrate the variation in engineering stress and strain curves as a function of temperature .....	43
28.	Cross-sectional view of the fractured tensile samples after testing at three different temperatures, -320 °F, ambient air, and 1200 °F. The samples were heat treated using 2-step aging cycle .....	44

## LIST OF FIGURES (Continued)

29.	Fracture surfaces of LP-DED NASA HR-1 tensile tested at 1200 °F. The sample were in (a) and (b) 1-step aged condition and (c) and (d) 2-step aged condition. The near gauge surface areas have some isolated intergranular fracture zones, while ductile dimple fracture predominates away from the specimen gauge surface .....	45
30.	Comparison of (a) tensile and yield strengths and (b) fracture elongation for LP-DED and wrought NASA HR-1 as a function of testing temperature .....	46
31.	The typical hysteresis loops of the first cycle, the near peak stress cycle (cycle 30), and the cycle that is the near half-life at 1.0% total strain in (a) 1-step aged condition and (b) 2-step aged condition .....	48
32.	The typical hysteresis loops of the first cycle, the near peak stress cycle (cycle 20), and the cycle that is near half-life at 2.0% total strain in (a) 1-step aged condition and (b) 2-step aged condition .....	49
33.	Variations of peak tensile stress ( $\sigma_{\max}$ ) and compressive stress ( $\sigma_{\min}$ ) with number of cycles (N) at (a) 1% total strain (.05% strain amplitude) and (b) 2% total strain (1.0% strain amplitude). The LCF samples were heat treated with two different aging cycles .....	50
34.	Variations of cyclic hardening ratio (HR) and softening ratio (SR) as function of total strain for LP-DED NASA HR-1 in (a) 1-step aged and (b) 2-step aged conditions.....	52
35.	LCF fracture surface of LP-DED NASA HR-1 tested at 1% total strain in (a) 1-step and (b) 2-step aged conditions. (c) Crack initiation from the surface and (d) distinct fatigue striation marks showing early stages of crack propagation in the 1-step aged specimen .....	54
36.	LCF fracture surface of LP-DED NASA HR-1 tested at 2% total strain in (a) 1-step and (b) 2-step aged conditions. (c) Crack initiation from the surface and (d) distinct fatigue striation marks showing early stage of crack propagation in the 2-step aged specimen.....	55
37.	LCP life comparison by superimposing strain-life curves for LP-DED and wrought NASA HR-1. The LP-DED LCF specimens were heat treated with two different against cycles (1-step and 2-step aging), while the wrought specimens were heat treated with the standard 1-step again at 1325 °F/16h.....	56

## LIST OF FIGURES (Continued)

38. The typical microstructure (in x-y plane) of the LP-DED NASA HR-1 samples used for tensile testing in 5ksi gaseous hydrogen environment. The average grain size is approximately 75  $\mu\text{m}$  ..... 57
39. Engineering stress-strain curves of LP-DED NASA HR-1 tensile tested in high pressure helium and hydrogen environment in (a) 1-step aged and (b) 2-step aged conditions. Serrated stress-strain flow behavior is observed for samples tested in high pressure hydrogen environment..... 60
40. Macrographs of LP-DED NASA HR-1 tensile tested in hydrogen showing:  
(a) orange peel appearance on the surface along the gauge length,  
(b) many sufrace cracks are present along the machining marks,  
(c) close-up views of surface cracks. This specimen was in 2-step aged condition..... 61
41. Optical images showing (a) cross-sectional view of a fractured tensile sample tested in 5ksi gaseous hydrogen environment, (b) noticeable surface cracks and plastic deformation are present in the shoulder region (region A in (a)), (c) 20 – 60  $\mu\text{m}$  deep surface cracks are present along the machining marks (region B in (a)), (d) and (e) the fracture surface is oriented at approximately 45° with respect to the loading direction and the fracture mode is predominantly ductile transgranular (regions C and D in (a)). This tensile specimen was in 2-step aged condition ..... 62
42. Optical micrographs showing (a) cross-sectional view of a fractured LP-DED NASA HR-1 tensile sample tested in 5ksi gaseous hydrogen environment, (b) numerous slip lines are present, and surface cracks are inclined approximately 45° with respect to the tensile loading axis that corresponds to the planes of near maximum sheer stress (from region A in (a)), (c) signs of heavy deformation near the fracture surface and the fracture mode is ductile trangranular (from region B in (a)). This tensile specimen was in 1-step aged condition ..... 63
43. SEM fractography of a 1-step aged LP-DED NASA HR-1 sample tensile tested in hydrogen showing (a) the overall fracture surface, (b) the HEE affected quasi-cleavage zone near surface (from the yellow box in (a)), (c) closeup view of the yellow box in (b), (d) the mixed quasi-cleavage and dimple fracture in the transition region..... 66
44. SEM fractography of a 2-step aged sample tensile tested in hydrogen showing (a) the overall fracture surface, (b) the near surface hydrogen affected zone from the blue box in (a), (c) the mixed quasi- cleavage and

## LIST OF FIGURES (Continued)

ductile dimple fracture from the red box in (b), (d) predominant ductile dimple fracture outside of the quasi-cleavage zone from the yellow box in (b) .....	67
45. LP-DED NASA HR-1 LCF tested in 5ksi gaseous hydrogen environment at 2% total strain showing the sypical hysteresis loops of the first cycle, the peak stress cycle (cycle 15), and the half-life cycle in (a) 1-step aged condition and (b) 2-step aged condition.....	70
46. Variations of peak tensile stress ( $\sigma_{\max}$ ) and compressive stress ( $\sigma_{\min}$ ) with number of cycles (N) at 2% total strain (1% strain amplitude) in high pressure gaseous hydrogen envirnoment. The LCF specimens were heat treated with two different aging cycles .....	71
47. LCF fracture surfaces of LP-DED NASA HR-1 tested at 2% total strain in 5ksi high pressure hydrogen environment in (a) 1-step and (b) 2-step aged condition .....	72
48. SEM fractographs of a 1-step aged specimen showing (a) LCF crack initiation in multiple sites and (b) distinct striation marks showing directions of early stage of crack propagation in the fatigue crack propagation region.....	73
49. LCF life comparison for LP-DED NASA HR-1 in air vs. in hydrogen. The LP-DED LCF specimens were heat treated using two different aging cycles, 1-step and 2-step aging .....	74
50. Effects of high pressure hydrogen on LCF life of LP-DED and wrought NASA HR-1. Aging for NASA HR-1 was conducted at 1325 °F/16h. LP-DED NASA HR-1 was aged with two different cycles, 1-step aging at 1325 °F/16h and 2-step aging at 1275 °F/16h + 1150 °F/16h. LCF resistance of LP-DED NASA HR-1 in hydrogen is significantly better than that of the wrought alloy .....	75
51. Compairson of thermal conductivity for LP-DED NASA HR-1 (inital composition), the wrought alloy, and the known literature date for DED NASA HR-1 (final composition).....	80
52. Comparison of thermal diffusivity for LP-DED NASA HR-1 (inital composition), the wrought alloy, and the known literature data for DED NASA HR-1 (final composition).....	81

## LIST OF FIGURES (Continued)

53.	Comparison of specific heat capacity for LP-DED NASA HR-1 (initial composition), the wrought alloy, and the known literature date for LP-DED NASA HR-1 (final composition) .....	82
54.	Comparison of predicted specific heat capacity obtained by using the mass-weighted Neumann-Kopp rule (Equation 9) for LP-DED NASA HR-1 (initial composition), the wrought alloy, and the known literature data for LP-DED NASA HR-1 (final composition) .....	83
55.	Examples of various NASA HR-1 LP-DED components. (a) Comes for powerhead, (b) 35K-lb nozzle with integral channels and welded manifolds, (c) Integral channel wall nozzle, (d) Powerhead half shell, (e) Hot-fire testing of regeneratively-cooled nozzle for LLAMA, (f) 7K-lb <sub>f</sub> nozzle for LLAMA, (g) High duty cycle testing of integral channel nozzle to 207 starts .....	85

## LIST OF TABLES

1.	Nominal chemical composition (wt%) of NASA HR-1 powder and its specification.....	4
2.	Nominal powder composition of NASA HR-1 and JBK-75.....	10
3.	Melting solidification behavior comparison for LP-DED NASA HR-1 and JBK-75 .....	14
4.	List of Md values for various elements in FCC Ni.....	24
5.	Nominal chemical composition (wt%) for wrought and LP-DED NASA HR-1. The Md levels of A-286 and JBK-75 were used as the estimated critical threshold value for LP-DED NASA HR-1 .....	26
6.	Heat treatment investigation plan intended to reduce Ti segregation in $\eta$ -phase precipitation at grain boundaries for LP-DED NASA HR-1 .....	27
7.	Effects of aging treatment on tensile properties for LP-DED NASA HR-1 .....	37
8.	Summary of tensile properties for LP-DED NASA HR-1, 1 as a function of testing temperature .....	41
9.	Room temperature LCF tests results for LP-DED NASA HR-1. LCF was conducted at ambient air at total strain range of 1% and 2%, and R= -1.....	47
10.	Comparison of the stress amplitudes at the maximum ( $\Delta\sigma_{max}$ ), first cycle ( $\Delta\sigma_{first}$ ) and half-life ( $\Delta\sigma_{half}$ ) for LP-DED NASA HR-1 tested at 1% and 2% total strain in both 1-step and 2-step aged conditions. HR and SR values are also given in Table 10 .....	52
11.	The average tensile properties, strain hardening exponent and testing duration for the tensile tests performed in high pressure helium and hydrogen environments .....	58

## LIST OF TABLES (Continued)

12.	The GH <sub>2</sub> /GHe ratios of yield stress (YW), ultimated tensile stress (UTS), and ductility (fracture elongations) for LP-DED and wrought NASA HR-1 .....	59
13.	LCF test results for LP-DED NASA HR-1 in 5ksi high pressure hydrogen environment at room temperature .....	68
14.	Comparison of the stress amplitudes at the maximum ( $\Delta\sigma_{\max}$ ), first cycle ( $\Delta\sigma_{\text{first}}$ ) and half-life ( $\Delta\sigma_{\text{half}}$ ) cycles for LP-DED NASA HR-1 tested at 2% total strain in 5ksi gaseous hydrogen environment. The LCF specimens were heat treated with two different aging cycles. HR and SR values were also given in this Table .....	69
15.	The average tensile properties for LP-DED and wrought NASA HR-1 in high pressure helium and hydrogen environments .....	77
16.	Nominal chemical composition (wt%) of wrought and LP-DED NASA HR-1 and the aging cycle used for thermal conductivity analysis.....	77
17.	Thermal diffusivity, thermal conductivity, and specific heat of LP-DED NASA HR-1 (initial formulation) as a function of temperature .....	78
18.	Thermal diffusivity, thermal conductivity, and specific heat of wrought NASA HR-1 as a funtion of temperature.....	79
19.	Thermal diffusivity, thermal conductivity, and specific heat of LP-DED NASA HR-1 (final formulation) as a function of temperature .....	79

## **LIST OF ACRONYMS AND SYMBOLS**

Al	Aluminum
AM	Additive Manufacturing
BP-DED	Blown Powder Directed Energy Deposition
C	Degree Celsius
$C_A$	The Amplitude of Ti concentration variation at time = t
$C_m$	Mean Ti Concentration
$C_{max}$	Grain Boundary Solute Atom Concentration after Homogenization
$C_{min}$	Grain Center Solute Atom Concentration after Homogenization
$C_{0max}$	Grain Boundary Solute Atom Concentration before Homogenization
$C_{0min}$	Grain Center Solute Atom Concentration before Homogenization
Co	Cobalt
Cr	Chromium
D	Diffusivity (Diffusion Coefficient)
$D_o$	Diffusion Constant ( $m^2/s$ )
DTA	Differential Thermal Analysis
DX	The Discrete Variational (DX)-X $\alpha$ cluster method cluster method
EDS	Energy-dispersive X-ray Spectroscopy
F	Degree Fahrenheit
FCC	Face Centered Cubic
Fe	Iron

## LIST OF ACRONYMS AND SYMBOLS (Continued)

GCP	Geometrically-Closed-Pack intermetallic phases (e.g. $\eta$ , $\delta$ phases)
HEE	Hydrogen Environment Embrittlement
HIP	Hot Isostatic Press
in	Inch(es)
K	Degree Kelvin
L	Half Wavelength of Ti Concentration
LCF	Low Cycle Fatigue
LEO	Liquid Engines Office
L-PBF	Laser Powder Bed Fusion
LP-DED	Laser Powder Directed Energy Deposition
LRE	Liquid Rocket Engine
Md	The d-orbital Energy Level
mm	Millimeter(s)
mm	Millimeter or 0.001 of a Meter
Mo	Molybdenum
MSFC	Marshall Space Flight Center
NASA	National Aeronautics and Space Administration
Ni	Nickel
PHACOMP	Phase Computation
psi	Pounds per square inch, an English pressure unit
Q	Diffusion Activation Energy (J/mole)

## **LIST OF ACRONYMS AND SYMBOLS (Continued)**

R	Gas Constant (8.31 J/mole-K)
RAMPT	Rapid Analysis and Manufacturing Propulsion Technology
SEM	Scanning Electron Microscopy
SLS	Space Launch System
STR	Solidification Temperature Range
TCP	Topologically-Closed-Pack intermetallic phases (e.g. $\sigma$ , $\chi$ , Laves phases)
Ti	Titanium
TM	Technical Memorandum
TRL	Technology Readiness Level
V	Vanadium
W	Tungsten
$\delta$	Residual Segregation Index
$\eta$ phase	$\text{Ni}_3\text{Ti}$
$\mu\text{m}$	Micrometer or 0.000001 of a Meter
$\sigma_y$	Flow stress at a specific temperature and strain rate



## TECHNICAL MEMORANDUM

# DEVELOPMENT OF DIRECTED ENERGY DEPOSITED NASA HR-1 TO OPTIMIZE PROPERTIES FOR LIQUID ROCKET ENGINE APPLICATIONS

### 1. INTRODUCTION

Metal additive manufacturing (AM) has been demonstrated to reduce the cost and lead time associated with manufacturing of complex components with internal features and novel alloys. The AM processes are changing the design and manufacturing of liquid rocket engines components such as injectors, combustion chambers, nozzles, valves, and other fluid and structural systems. While additive manufacturing is continuing to evolve, it is still in its infancy, and over the past 10 years, the materials available have been limited.<sup>1</sup> As AM is considered for a design application, the designer has been forced to use the limited available materials, which may not be the optimal material for performance. The National Aeronautics and Space Administration (NASA) has identified the need to develop and advance new materials for liquid rocket engine (LRE) applications such as hydrogen environments. One such material being developed is NASA HR-1.<sup>2-4</sup> NASA HR-1 is a high-strength Fe-Ni superalloy designed to resist high pressure, hydrogen environment embrittlement, oxidation, and corrosion.<sup>5</sup>

Combustion device components on liquid rocket engines operate in extreme environments that challenge the functional design, materials, and fabrication as part of an engine system. These components include combustion chambers, nozzles, injectors, gas generators, and igniter systems. Each of these components serves different functions but have some commonality in requirements. They must endure high pressure propellants, high temperature, and high pressure gases, while maintaining positive structural margins but low mass as part of the engine system and launch vehicle. Component structures used in LREs can require very thin walls, in regeneratively-cooled nozzles for instance, that provide challenges for materials to sustain high thermal and structural loads. Additionally, combining the environment with liquid and gaseous hydrogen propellant to the thermal and structural loads leads to an even more complex challenge. For these applications, materials must be designed to resist Hydrogen Environment Embrittlement (HEE).<sup>2-4</sup> Furthermore, these components also have other key requirements to consider for materials selection, including mechanical strength, ductility, low cycle fatigue (LCF), and thermophysical properties such as thermal conductivity.<sup>2-3</sup>

The regeneratively-cooled, or channel-cooled nozzle, is a key component in various engine systems that expands combustion gases and increases the exhaust gas velocity. The cooled nozzle is often the largest structure on the liquid rocket engine but must maintain small internal channels for proper cooling of the hot-wall to maintain adequate structural margins. The design is balanced among extreme temperature environments, high pressure fluids, and structural loads from pres-

sure, thrust, and sideloads during startup and shutdown. A common heritage design for regeneratively-cooled nozzles is the use of brazed tubes, but this technique presents challenges in the lead time and number of piece-parts, tube-stacking and assembly operations, brazing, and tooling.<sup>6</sup> The manufacturing of large channel wall nozzles have been explored using various technologies including hot isostatic pressing (HIP) assisted brazing, laser welding, plating, and laser wire direct closeout.<sup>7,8</sup> NASA and other organizations have discussed the use of AM and advanced manufacturing techniques to solve some of the traditional manufacturing challenges for combustion chambers and nozzles.<sup>9–13</sup> Many of these techniques focus on the reduction in cost and schedule for fabrication but have also put an emphasis on increasing the scale, specifically AM processes.

The laser powder directed energy deposition (LP-DED) process uses concentrated thermal energy, achieved with a laser, to fuse metals by melting locally as the material is injected into a melt pool.<sup>3</sup> This process allows for freeform fabrication of components or addition of material to components for the purposes of coating, repair, or modification using local deposition. Freeform components are formed by the precise control of toolpath parameters created from a CAD model that creates individual (weld) beads that are deposited to take a final geometric shape. LP-DED uses powder feedstock as the filler material and a laser as the energy source. The powder and laser optics are mounted on an integrated deposition head, which allows for the convergence of the laser and powder at a defined focus at the surface of the substrate where material is melted and cooled to form the bead. The build substrate can be a sacrificial build plate or an existing component. The deposition head is mounted to a robotic arm or gantry system to control the motion through programmed or logic tool paths to deposit material or create features. An example of the process can be seen in Figure 1.

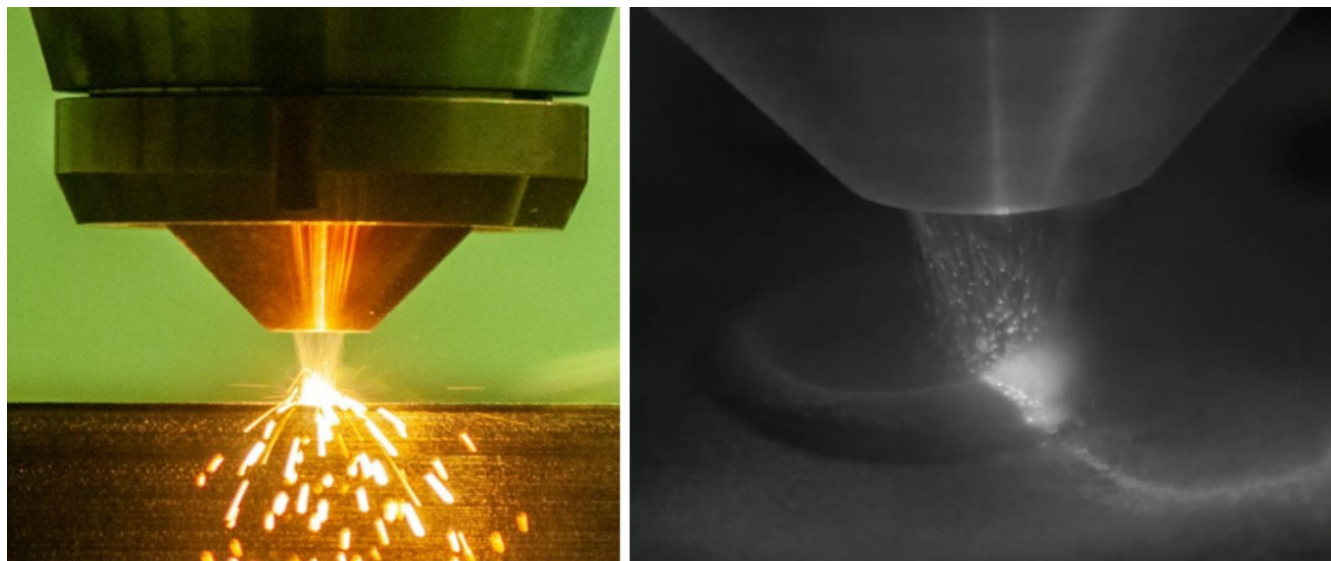


Figure 1. Material being deposited using LP-DED.<sup>3</sup> Images used with permissions from: (Left) Addup, and (Right) Formalloy.

The LP-DED processed NASA HR-1 requires several post-processing heat treatment steps to attain the material's properties that are desirable for the application. These steps often include a stress relief, homogenization, solution anneal, and aging treatment for precipitation hardened alloys.<sup>2-4</sup> An effective stress relief mitigates residual stresses built up in the part during the LP-DED process and minimizes the potential distortions. The second step, homogenization, is a common treatment for AM materials to reduce elemental segregation and promote recrystallization to achieve a more equiaxed grain structure in the material. The third step, solution treatment, brings the part to a solid solution temperature to dissolve undesirable  $\eta$ -phase that forms during cooling from homogenization treatment, and then is rapidly cooled to maintain  $\eta$ -phase free solid solution. Finally, the aging treatment promotes the precipitation of the strengthening phase in the alloy, the  $\gamma'$  phase for NASA HR-1.<sup>2,5</sup>

There are five key requirements to consider for LRE nozzle material selection, including mechanical strength, ductility, low cycle fatigue (LCF), and thermal conductivity.<sup>3</sup> These five material properties are all interrelated and must be taken into consideration when optimizing the alloy composition and heat treatment for the LP-DED NASA HR-1 alloy. This Technical Memorandum addresses the development of LP-DED NASA HR-1 through optimization of chemical composition and heat treatment to obtain an optimum balance of key material properties for liquid rocket engine applications. To date, the composition of NASA HR-1 has been successfully modified for use with the LP-DED technique. The PHACOMP method was applied to guide composition modification in order to obtain an optimum balance of the five key material properties.<sup>3</sup> Improved homogenization and 2-step aging treatments were also developed to reduce Ti segregation to an acceptable level that is essential for mitigation of  $\eta$ -phase precipitation at grain boundaries. There were many observations and lessons learned from the development of LP-DED NASA HR-1. The combined effects of composition modification and heat treatment optimization enable high quality NASA HR-1 components to be fabricated via the LP-DED technique. The improved chemical and microstructural homogeneities make LP-DED NASA HR-1 components more ductile and have higher resistance to LCF in high pressure hydrogen environment, which is vital for the success and safety of LRE nozzles.

## 2. EXPERIMENTAL PROCEDURES AND METHODS

### 2.1 Material and LP-DED process

The material used for the heat treatment study was single-pass and multi-pass LP-DED NASA HR-1 panels and round bars deposited on an RPM Innovations (RPMI) 557 machine. The feedstock NASA HR-1 powder used for the LP-DED process was a pre-alloyed rotary-atomized powder produced in vacuum or by inert induction melting utilizing rotary atomization in argon. The nominal composition of the LP-DED NASA HR-1 powder and its specification is shown in Table 1. The powder size distribution was between 45 and 105  $\mu\text{m}$  ( $-140$  mesh/ $+325$  mesh). A SEM image of NASA HR-1 powder is shown in Figure 2. NASA HR-1 powder is mostly spherical shape with a few oblong ellipsoidal particles and some traces of satellites.

Table 1. Nominal chemical composition (wt%) of NASA HR-1 powder and its specification.

Element	Nominal	Minimum	Maximum
Iron	BAL	-	-
Nickel	34.00	33.70	34.30
Chromium	14.60	14.30	14.90
Cobalt	3.80	3.60	4.00
Molybdenum	1.80	1.60	2.00
Tungsten	1.60	1.40	1.80
Titanium	2.40	2.20	2.60
Vanadium	0.30	0.28	0.32
Aluminum	0.25	0.23	0.27
Sulfur	-	-	0.005
Phosphorus	-	-	0.005
Carbon	-	-	0.03
Silicon	-	-	0.05
Boron	-	-	0.005
Manganese	-	-	0.05
Hydrogen	-	-	<50 ppm
Oxygen	-	-	<100 ppm ( $-140/+325$ mesh) <200 ppm ( $-325$ mesh/ $+10$ $\mu\text{m}$ )
Nitrogen	-	-	<50 ppm

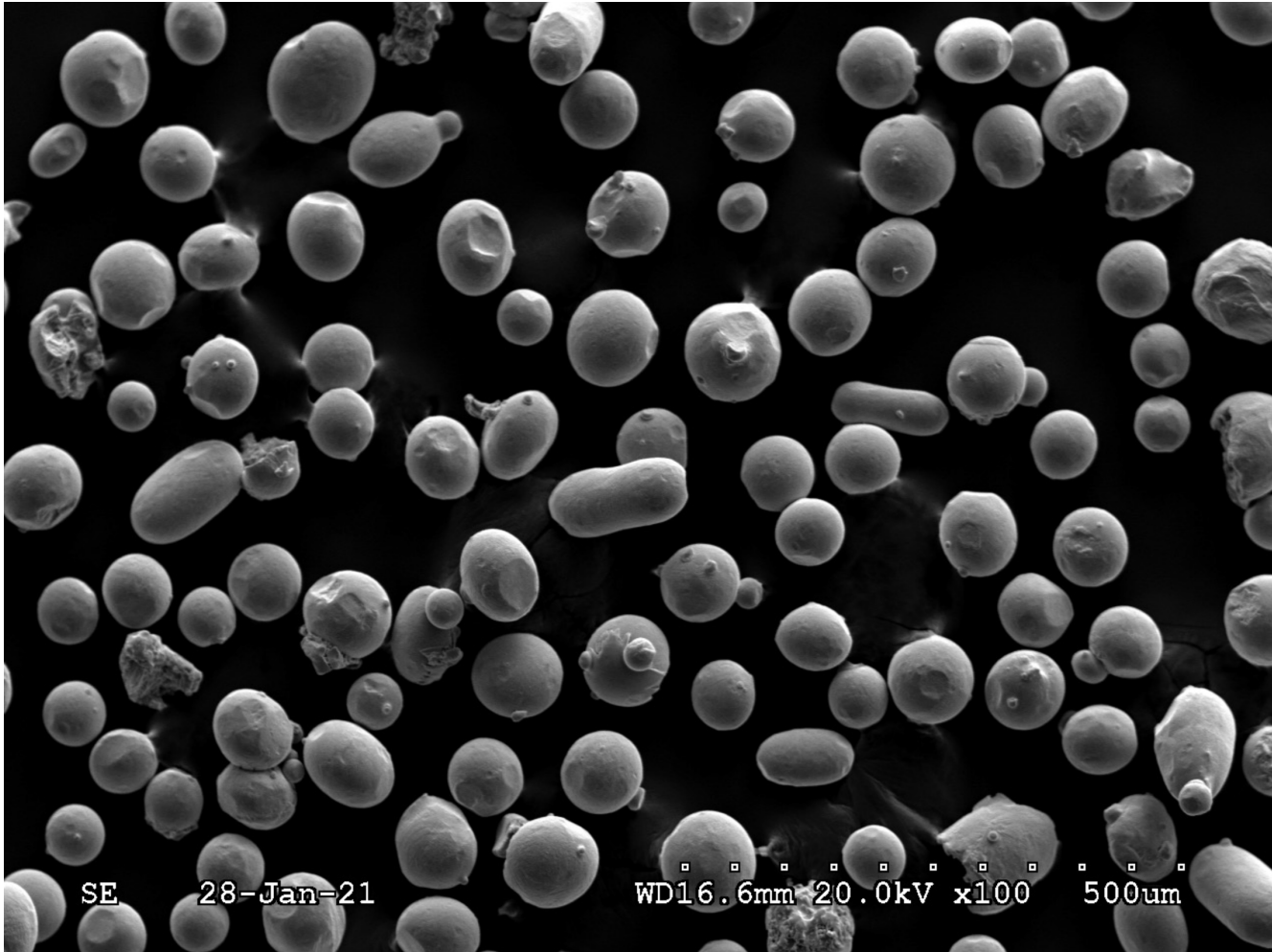


Figure 2. A SEM image showing NASA HR-1 powder particle morphology.

LP-DED samples for heat treatment optimization and mechanical testing were furnished by RPM Innovations (RPMI). The 0.125 inches (3.175 mm) and 0.047 inches (1.194 mm) thick panels were deposited at a laser power of 1070 watts and 350 watts, respectively. The LP-DED process for both 0.125 inches and 0.047 inches thick panels was conducted with single passes per layer that are parallel to the previous layer. The samples for tensile and low cycle fatigue (LCF) testing are multi-pass round bars. The LP-DED round bar samples were deposited at a laser power of 1070 watts to a length of 4 inches and 0.6 inch in diameter. An illustration of NASA HR-1 round bar and block fabrication via LP-DED process is shown in Figure 3(a). The multi-pass round bars and single-pass panels used in this study are shown in Figure 3(b) and (c).

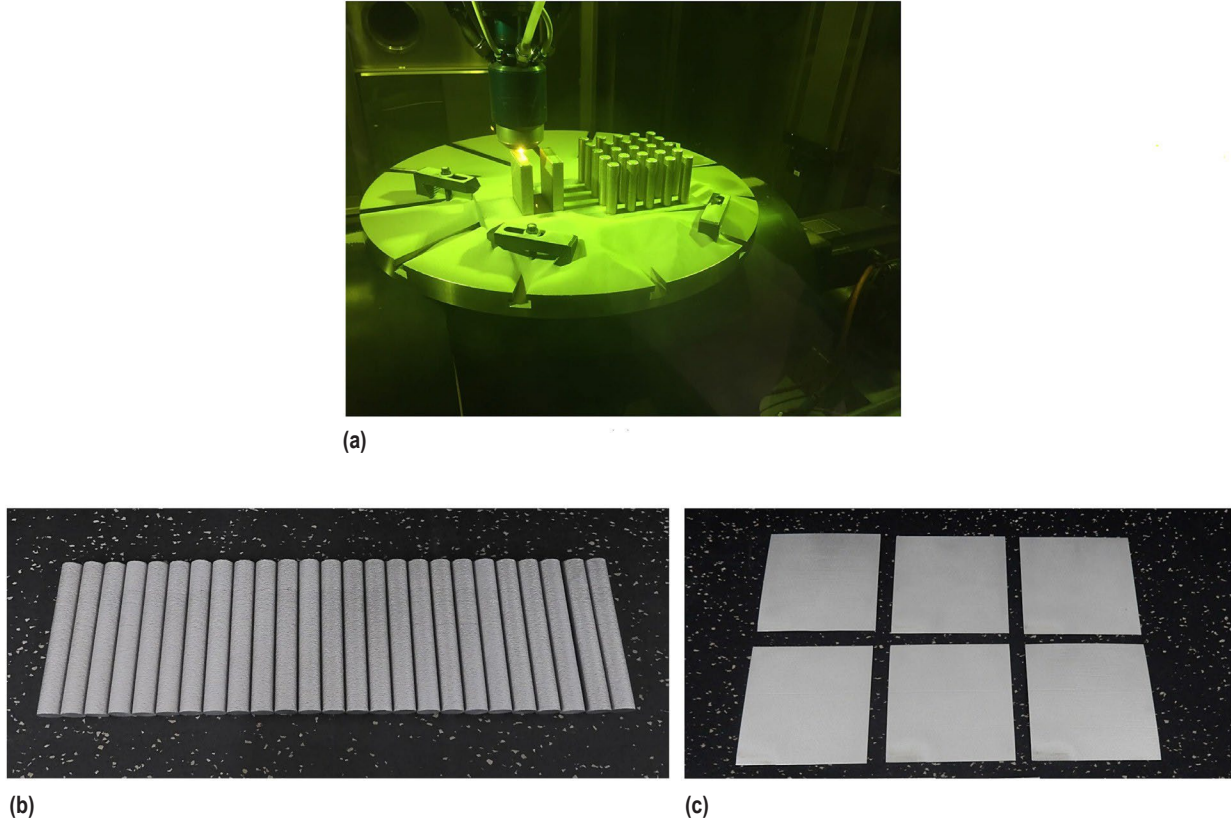


Figure 3. (a) An illustration of NASA HR-1 round bar and block fabrication via LP-DED process, (b) round bars with a length of 4 inches and diameter of 0.6 inches fabricated at a laser power of 1070 watts, (c)  $4 \times 4 \times 0.04$  inches single-pass thin panels fabricated with 350 watts laser power.

## 2.2 Differential Thermal Analysis (DTA)

Differential Thermal Analysis (DTA) was used to analyze the melting-solidification behavior of LP-DED NASA HR-1 and JBK-75. NASA HR-1 was originally developed at NASA in the 1990's by deriving from JBK-75 to increase strength and ductility in high-pressure hydrogen environments. DTA analyses were performed using virgin NASA HR-1 powder and as-built LP-DED bars on a Netzsch STA 409CD thermal analyzer. The atmosphere was high purity Ar gas and an  $\text{A}_2\text{O}_3$  empty crucible was used as the reference sample. Samples were heated from room temperature to  $1550^\circ\text{C}$  at  $10^\circ\text{C}/\text{min}$ , and cooling was also performed using the same rate. The endothermic peaks indicate melting reaction, while exothermic peaks signify solidification reaction. The DTA effort aims at obtaining a better understanding of melting and solidification characteristics of LP-DED NASA HR-1.

### **2.3 Heat Treatment**

After deposition, parts require post-processing heat treatment to attain the desirable materials properties. For LP-DED NASA HR-1 parts, the heat treatment steps include a stress relief, homogenization, solution anneal, and aging treatment. The as-built samples received stress-relief treatment at 1950 °F/1.5h with a slow furnace cool. After stress relief, the samples were subjected to a homogenization treatment at 2125 °F/6h in a vacuum furnace. At the end of homogenization treatment, the samples were Ar quenched to minimize  $\eta$ -phase precipitation. Then, the samples were solution annealed at 1950 °F/1h in vacuum with an Ar quench and followed by aging at 1325 °F/16h or 1275 °F/16h + 1150 °F/16h in vacuum to complete the heat treatment process.

### **2.4 Metallography and SEM analysis**

Selected LP-DED NASA HR-1 specimens were metallurgically characterized after heat treatment and mechanical testing. Specimens were sectioned, mounted, ground, and polished using standard metallographic procedures with a series of 220-2,000 grit paper and 3  $\mu\text{m}$  diamond suspension – 0.05  $\mu\text{m}$  alumina pads. Chemical etching was conducted with waterless Kaling's reagent immersed for 5–10 seconds. Microstructures of as-deposited and heat treated NASA HR-1 were examined via optical (Leica DMi8 A) and scanning electron microscopy (SEM) (Hitachi S-3700N) equipped with an energy-dispersive X-ray spectroscopy (EDS) detector (Oxford Instruments X-maxN 80). High resolution optical montage images were taken to document the microstructure for the entire sample. Elemental analysis was conducted using EDS line scans at 15 kV and 0.5  $\mu\text{m}$  between spectra.

Investigation of titanium segregation was carried out using an EDS detector attached to an SEM. For as-deposited samples, EDS line scans were performed across the solidification structure that has a minimum distance of 250  $\mu\text{m}$  to reveal the concentration profile of titanium. For heat treated samples, the EDS line scans were greater than 250  $\mu\text{m}$  and across at least one grain (two grain boundaries) to see the fluctuation of titanium concentration between grain boundaries and grain interior. Homogenization kinetic calculations were performed to determine the titanium concentration distribution between grain boundaries as a function of homogenization temperature, time and grain size.

### **2.5 Mechanical Testing**

Initial tensile testing was performed in ambient air with a strain rate of 0.5 in/in/min at three different temperatures, –320 °F, room temperature, and 1200 °F. Elevated temperature tensile testing was conducted using a Mayes elevated temperature extensometer (Model: R3/8 Block 2) on a Instron load frame equipped with a 250 kN load cell according to guidelines established in ASTM E21, Standard Test Methods for Elevated Temperature Tension Tests of Metallic Materials. Room temperature testing was conducted using an Instron 5582 load frame equipped with a 100 kN load cell and a Instron model 2620 extensometer according to guidelines established in ASTM E8, Standard Test Methods for Tension Testing of Metallic Materials. Tensile testing was also performed in 5 ksi high pressure gaseous helium (GHe) and gaseous hydrogen (GH<sub>2</sub>) environments at room temperature. In 5 ksi GHe environment, the specimens were tensile tested at a strain rate

of 0.02 in/in/min (in/in/min) until 2.0% elongation; then the strain rate was increased to 0.05 in/in/min to failure. In 5 ksi GH<sub>2</sub> environment, tensile testing was conducted at a very slow strain rate of 0.0001 in/in/min until failure. The slower strain rate was intended to closely gauge the HEE susceptibility, which generally increases with decreasing strain rates. Geometry of the smooth tensile specimen used for testing in 5 ksi GHe and GH<sub>2</sub> environments at ambient temperature is shown in Figure 4. Final machining of the gauge section was performed by turning and the specified surface finish for the gauge section was 32  $\mu$ in.

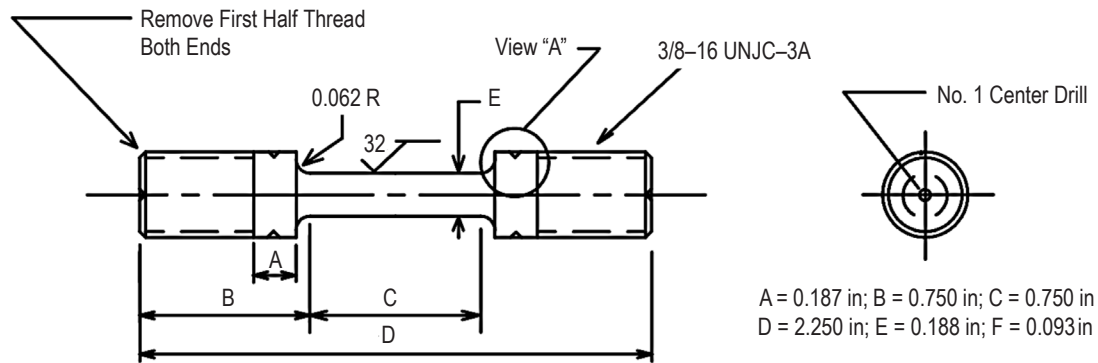


Figure 4. Geometry of the smooth specimen used for tensile testing in 5 ksi gaseous helium and hydrogen environments at ambient temperature. All dimensions are in inches. The reduced section (C) is required to have slight taper to center, 0.002 Max.

Fully reversed tension-compression ( $R = -1$ ) type low cycle fatigue (LCF) tests were conducted in air at ambient temperature in a strain controlled mode at a frequency of 30 cycles per minute (0.5 hz) and two total strain amplitudes (1.0% and 2.0%). LCF tests were also conducted in 5 ksi gaseous hydrogen environment at ambient temperature to investigate the effect of high pressure hydrogen on LCF behavior of LP-DED NASA HR-1. The LCF tests in 5 ksi gaseous hydrogen environment were conducted at  $R = -1$  and a total strain amplitude of 2%. Geometry of the fatigue specimen for LCF testing in 5 ksi gaseous hydrogen environment is shown in Figure 5. The LCF specimen has a nominal diameter of 0.25 inches, and the method of final machining of the gauge section is low stress grinding. Final polish was performed in longitudinal direction to remove circumferential machining marks to have a surface finish of approximately 4 RMS (root mean square). Low cycle fatigue specimens were tested in accordance with fatigue testing guidelines ASTM E606, Standard Test Method for Strain-Controlled Fatigue Testing.

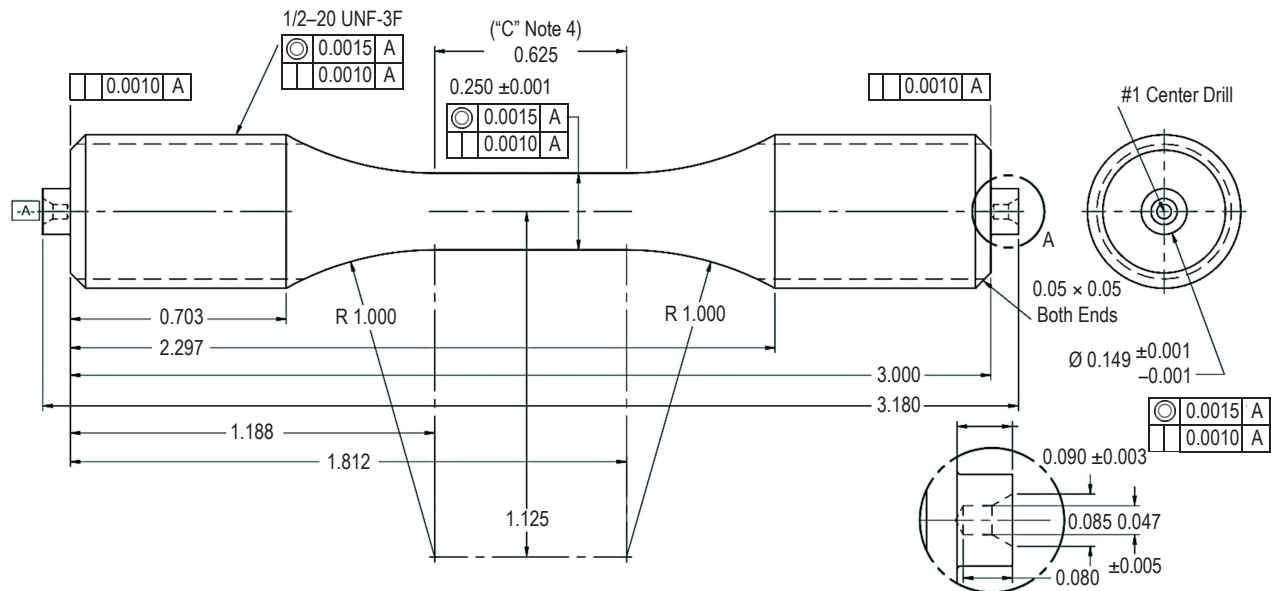


Figure 5. Geometry of the smooth specimen used for LCF testing in 5 ksi gaseous hydrogen environment at ambient temperature. All dimensions are in inches. The reduced section (C) is required to be low stress ground to final diameter.

### 3. RESULTS AND DISCUSSIONS

#### 3.1 Melting and solidification characteristics

DTA (Differential Thermal Analysis) can precisely determine solids/liquids temperatures and detect precipitate formation/dissolution reactions for an alloy in a timely fashion without laborious heat treating and metallographic analysis. In addition, DTA can compare alloy solidification temperature range (STR) and volume fraction of terminal eutectic phase that can provide insights into weldability and printability in additive manufacturing. During the early stage of LP-DED NASA HR-1 development, little data was available to help understand the solid-liquid transition temperatures during AM heating and cooling processes. Therefore, DTA was used to analyze the melting and solidification behaviors for NASA HR-1. The nominal powder composition of NASA HR-1 and JBK-75 is shown in Table 2.

Table 2. Nominal powder composition of NASA HR-1 and JBK-75.

Alloy Powder	Fe	Ni	Cr	Mo	V	W	Co	Ti	Al
NASA HR-1	39.80	34.00	15.50	2.20	0.32	2.10	3.30	2.50	0.25
JBK-75	51.13	30.20	14.75	1.25	0.30	-	-	2.10	0.25

Figure 6 shows the typical DTA heating and cooling curves for NASA HR-1 powder. On heating, there are two distinct endothermic peaks. The first peak represents the melting temperature (on-heating liquidus at 2516 °F) of  $\gamma$  matrix, whereas the second peak is close to the melting temperature of pure iron (Fe) at 2737 °F. The presence of two endothermic melting peaks indicates that there was appreciable elemental segregation in the powder particles. During the cooling cycle, there is a distinct solidification peak at 2455 °F (on-cooling solidus) and a smaller exothermic peak that represents terminal liquid solidification at 2320 °F. The solidification temperature range for NASA HR-1 powder is determined to be 196 °F, which is taken as the difference between the on-heating liquidus temperature (2516 °F) and the on-cooling terminal liquid solidification temperature (2320 °F).

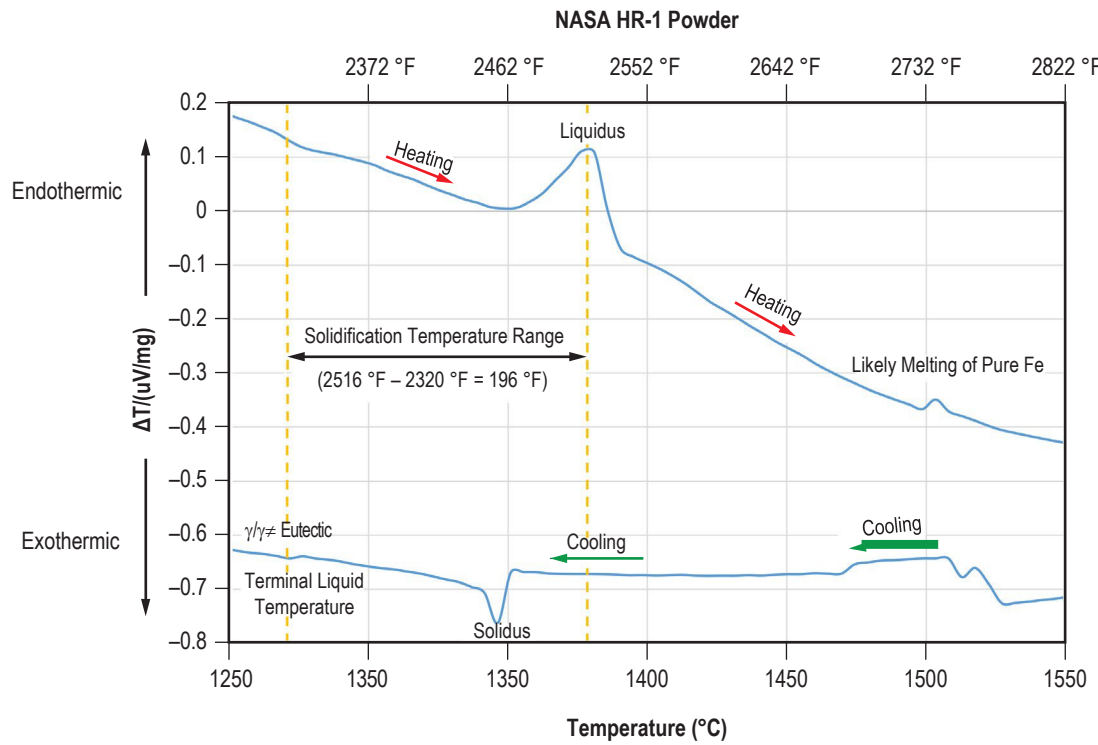


Figure 6. DTA heating and cooling curves for NASA HR-1 powder. The solidification temperature range for NASA HR-1 powder is determined to be 196 °F.

The heating and cooling DTA curves for as-built LP-DED NASA HR-1 are shown in Figure 7. On heating, the as-built material has only one distinct endothermic peak that represents the on-heating liquidus at 2521 °F. The peak that corresponds to the melting temperature of pure iron (at around 2737 °F) is not present. It is evident that LP-DED NASA HR-1 sample has a lower degree of elemental segregation than the powder sample as the Fe melting peak is present in the powder sample only. During the cooling cycle, there is a distinct solidification peak at 2446 °F (on-cooling solidus) and a smaller peak that represents terminal liquid solidification at 2370 °F. The solidification temperature range for as-built LP-DED NASA HR-1 is determined to be 151 °F, which is the difference between the on-heating liquidus temperature (2521 °F) and the on-cooling terminal liquid solidification temperature (2370 °F).

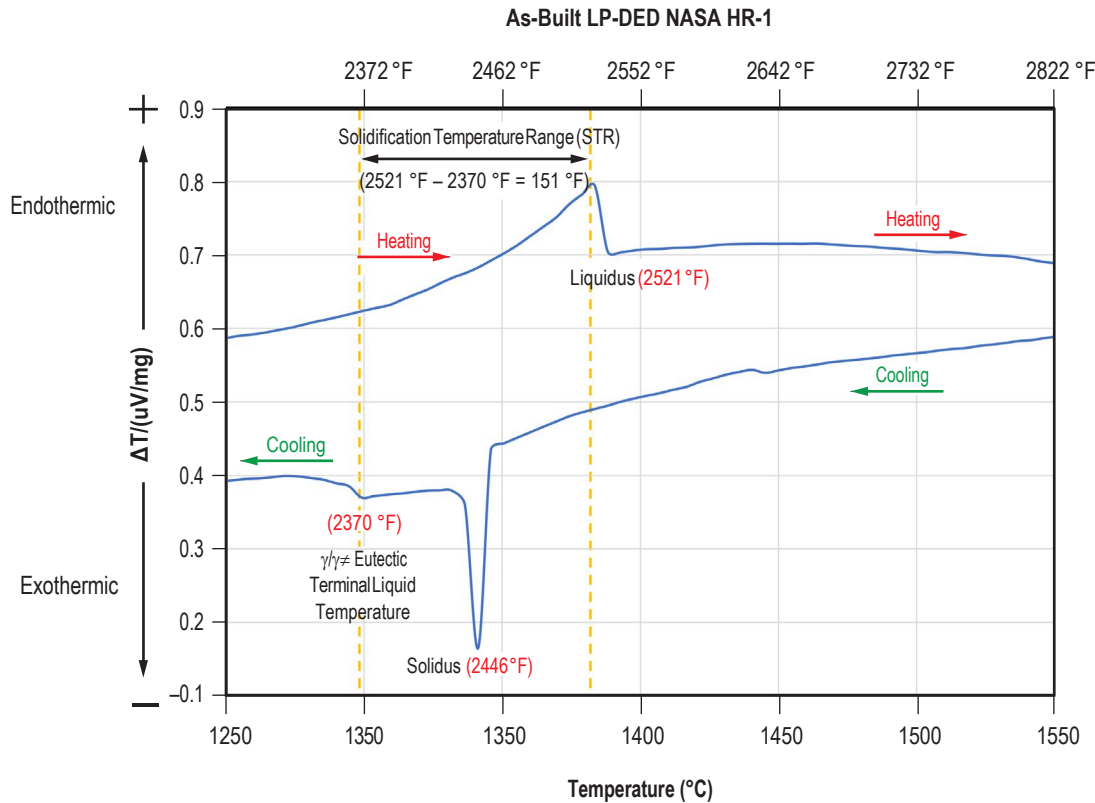


Figure 7. DTA heating and cooling curves for as-built LP-DEN NASA HR-1. The solidification temperature range for as-built LP-DEN NASA HR-1 is determined to be 151 °F.

DTA was also performed for JBK-75, a Fe-Ni-based superalloy that NASA HR-1 was derived from, to compare the melting and solidification behaviors between these two alloys. The DTA curves for as-built LP-DEN JBK-75 are shown in Figure 8. The melting and solidification characteristics of LP-DEN JBK-75 are similar to that of the as-built LP-DEN NASA HR-1. On heating, the as-built material has one distinct endothermic peak that represents the on-heating liquidus at 2554 °F. During the cooling cycle, there is a distinct solidification peak at 2511 °F (on-cooling solidus) and a very shallow peak that represents terminal liquid solidification at 2358 °F. The solidification temperature range for as-built LP-DEN JBK-75 is determined to be 196 °F, which is the difference between the on-heating liquidus temperature (2554 °F) and the on-cooling terminal liquid solidification temperature (2358 °F).

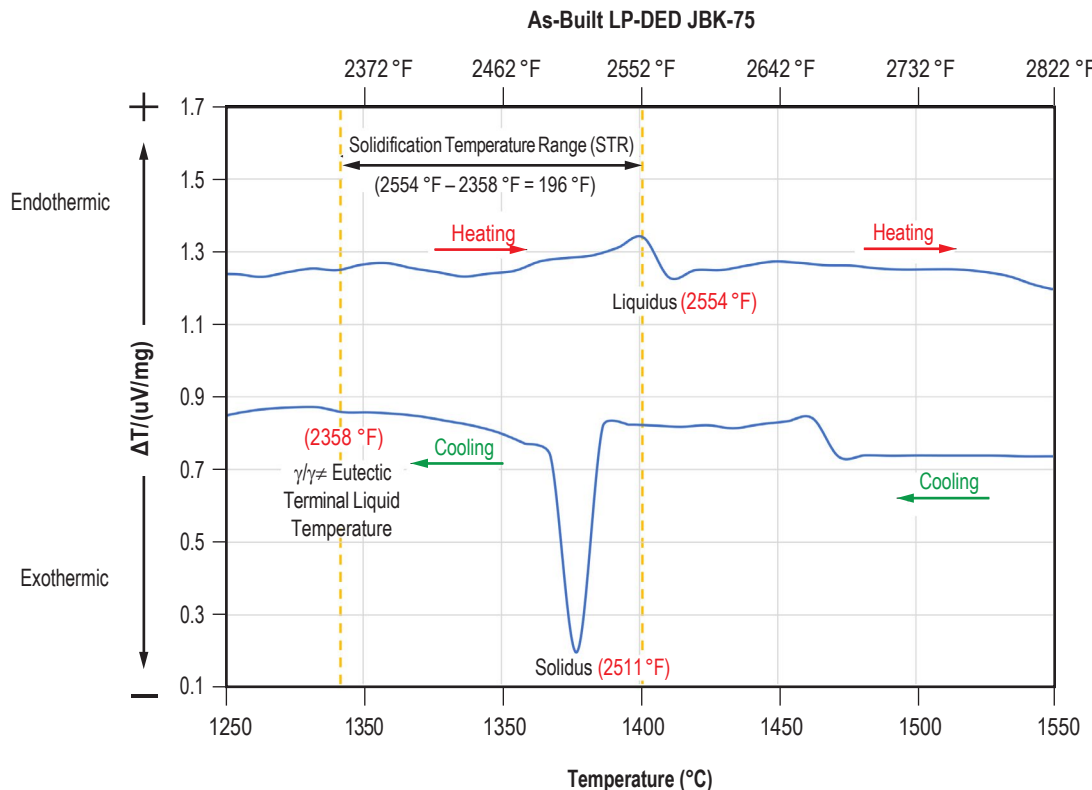


Figure 8. DTA heating and cooling curves for as-built LP-DEN JBK-75. The solidification temperature range for as-built LP-DEN JBK-75 is determined to be 196 °F.

Table 3 summarizes melting-solidification behavior comparison for NASA HR-1 powder and as built LP-DEN NASA HR-1 and JBK-75. Overall, these two alloys exhibit similar melting and solidification behavior. One notable difference between these two alloys is the solidification temperature range (STR), which is 151 °F for LP-DEN NASA HR-1 and 196 °F for LP-DEN JBK-75. Figure 9 compares the terminal liquid solidification peaks for LP-DEN NASA HR-1 and LP-DEN JBK-75. These two materials exhibit a eutectic-terminal liquid solidification peak that occurs at 2358 – 2370 °F. It is evident that LP-DEN NASA HR-1 has a more distinct terminal liquid solidification peak at around 2370 °F. LP-DEN JBK-75 also has a terminal liquid solidification peak at around 2358 °F, but it is very small suggesting the terminal liquid vol.-% is much smaller than that in LP-DEN NASA HR-1. Susceptibility to weld solidification cracking is affected by both metallurgical factors and the level of local strain at the end of solidification. In terms of metallurgical factors, the STR as well as the amount and distribution of the terminal liquid are the primary factors that affect the susceptibility of solidification cracking in Ni-base alloys. The solidification temperature range controls the size of semi-solid crack susceptible region that surrounds the liquid weld pool. A narrow STR is preferred as a relatively wider STR will produce a larger semi-solid crack susceptible region, thus increasing the weld cracking susceptibility.<sup>13</sup>

Table 3. Melting-solidification behavior comparison for LP-DED NASA HR-1 and JBK-75.

Alloy	Heating/Cooling Rate	On Heating-Liquidus	Eutectic Solidification	STR °F = (Solidification Temperature Range)
NASA HR-1 powder	10 °C/min	2516 °F	2320 °F	196 °F (2516 – 2320 °F)
LP-DED NASA HR-1, as-built	10 °C/min	2521 °F	2370 °F	151 °F (2521 – 2370 °F)
LP-DED JBK-75, as-built	10 °C/min	2554 °F	2358 °F	196 °F (2554 – 2358 °F)

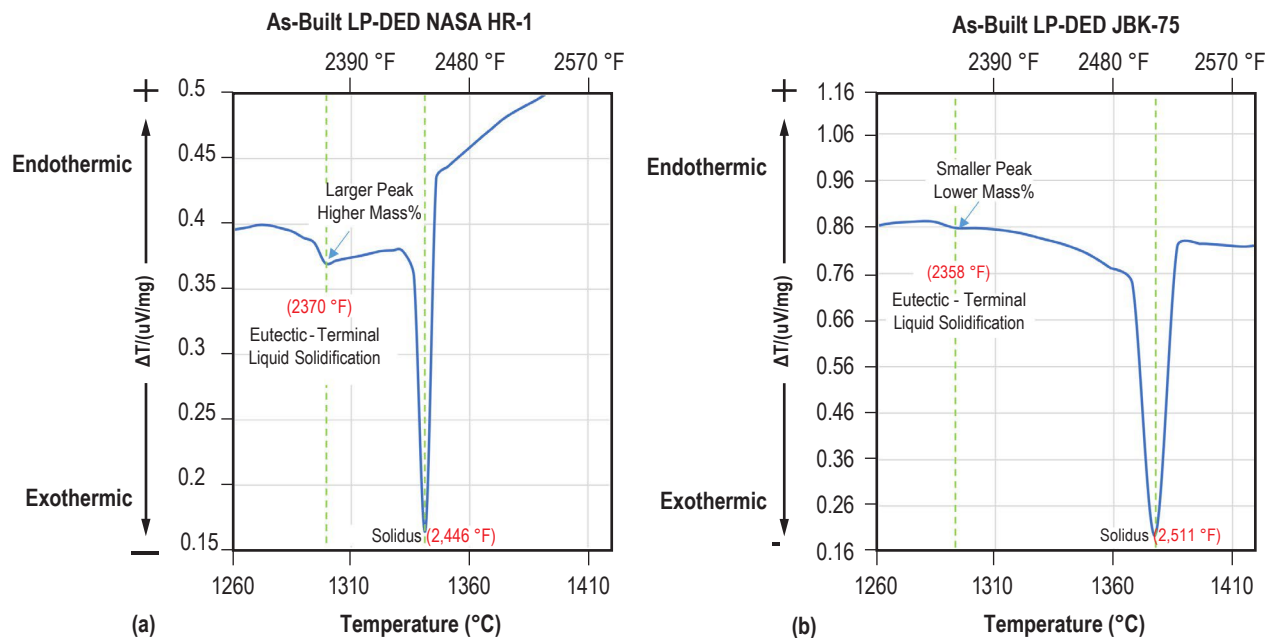


Figure 9. Solidification behavior analysis for (a) as-built LP-DED NASA HR-1; and (b) as-built LP-DED JBK-75. LP-DED NASA HR-1 has a more distinct terminal liquid solidification peak at around 2370° F.

In many alloys, cracks can form during the terminal stages of solidification when liquid films are distributed along the grain boundaries and, in some cases, interdendritic sites. At this stage, shrinkage strains across the partially solidified boundaries can become appreciable. For a given alloy system, the solidification temperature range and amount of terminal liquid are controlled primarily by chemical composition. The amount of terminal liquid is the product of a eutectic reaction that occurs at the end of solidification. This eutectic reaction occurs at a lower temperature than the alloy solidus and expands the solidification temperature range, making the alloy more susceptible to solidification cracking. However, when the amount of terminal liquid is high, it can often flow back into the cracks and provide a ‘crack healing’ effect. It is generally recognized that the backfilling of solidification cracks by the terminal eutectic liquid can reduce

or eliminate solidification cracking, particularly at low restraint level.<sup>14</sup> When the effects of microstructure are not taken into consideration, the DTA results suggest LP-DED NASA HR-1 is expected to have superior weldability to that of LP-DED JBK-75.

NASA HR-1 has shown very good printability when fabricating components using LP-DED and laser powder bed fusion (L-PBF) techniques. Metal additive manufacturing (such as LP-DED and L-PBF) is fundamentally a repeated welding process, where the layer-by-layer growth of the component is achieved through local melting of metal powder by a laser energy source. Although the metallic AM process results in solidification cooling rates that are far higher than those seen in more traditional welding processes, the existing weldability and weld cracking susceptibility theories can still be applied for AM materials. Candidate materials for AM should be weldable alloys that are less susceptible to cracking that originates in the liquid phase, such as solidification cracking and liquation cracking. AM alloys should also have good resistance to solid-state cracking phenomenon that occurs due to stresses build-up at temperatures slightly below the solidus temperature, such as strain-age cracking and ductility-dip cracking. NASA HR-1 in wrought form has excellent resistance to solidification cracking.<sup>5</sup> Based on its Al, Ti, Cr, and Co contents, NASA HR-1 is expected to have good resistance to strain-age cracking and ductility dip cracking.<sup>15</sup> Therefore, it is postulated the excellent printability that NASA HR-1 possesses when building components using LP-DED and L-PBF processes can be attributed to its decent resistance to liquid and solid state cracking.

## 3.2 Microstructure Evolution

### 3.2.1 Microstructure of As-Built LP-DED NASA HR-1

Figure 10 shows the typical cross section microstructure of an as-built 3.175 mm thick LP-DED panel. This panel was deposited at a laser power of 1070 watts with a single pass per layer that are parallel to the previous layer. The melt pool boundary is readily apparent in the as built material. The columnar dendrites, which are common in as-built LP-DED materials, are shown in greater detail in Figure 10(b). In the high energy LP-DED process, the melt pools are cooled rapidly and the growing grains (and dendrites) align themselves with the temperature gradients and result in columnar structure morphology.<sup>16</sup> The dendrites exhibit a pattern of formation from the outer perimeter of the melt pool toward a central point in single-pass LP-DED NASA HR-1. The large temperature gradient provides favorable conditions for epitaxial dendrite (grain) growth. As a result, the dendrites in the new layers are formed with the same orientation as the previous layers through several melt pools. The dendrites are somewhat randomly oriented near the melt pool periphery (toward the panel outer surface) likely due to the complex temperature gradient from the melt pool to the surrounding material. A close-up view of the dendritic structure in an as-built single-pass LP-DED NASA HR-1 panel is shown in Figure 11. The size of dendrite cell is very small and the dendritic arm spacing is in most cases smaller than 25  $\mu\text{m}$ . Solute rejection of titanium to the interdendritic regions on solidification leads to the preferential attack upon etching. As a result, the existence of titanium segregation is revealed as the dark spots in the interdendritic regions.<sup>3</sup>

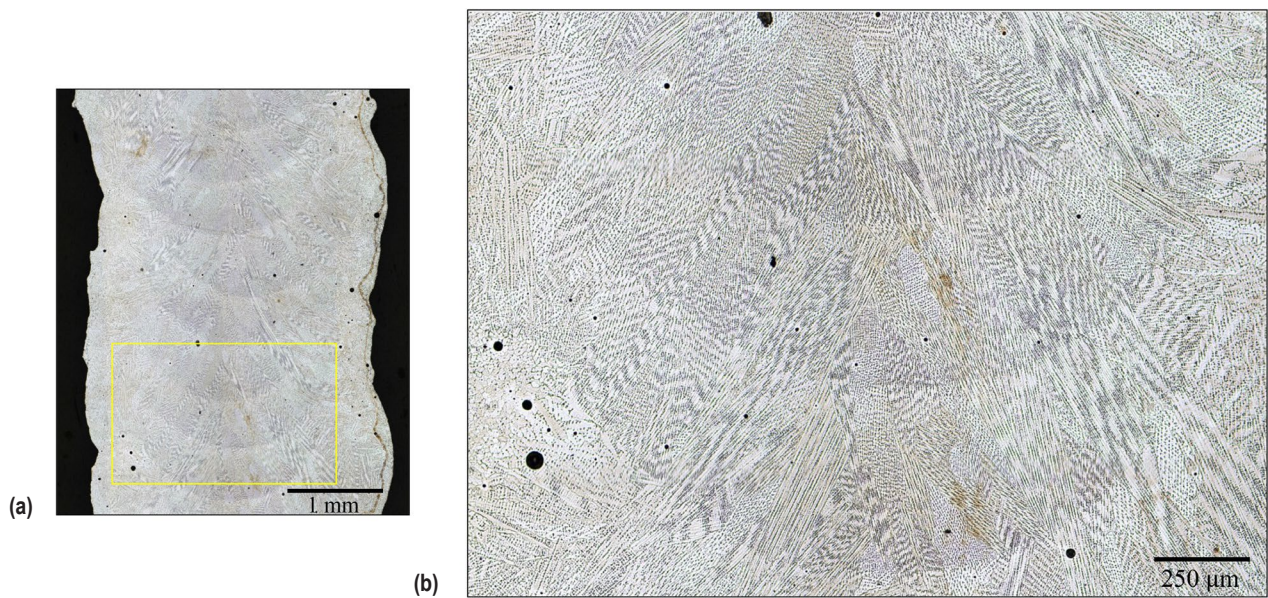


Figure 10. Optical micrographs showing the cross section microstructure of as-built LP-DED NASA HR-1. This single-pass LP-DED panel was deposited with a thickness of approximately 3.175 mm (laser power 1070 watts), the build direction is vertically upward.

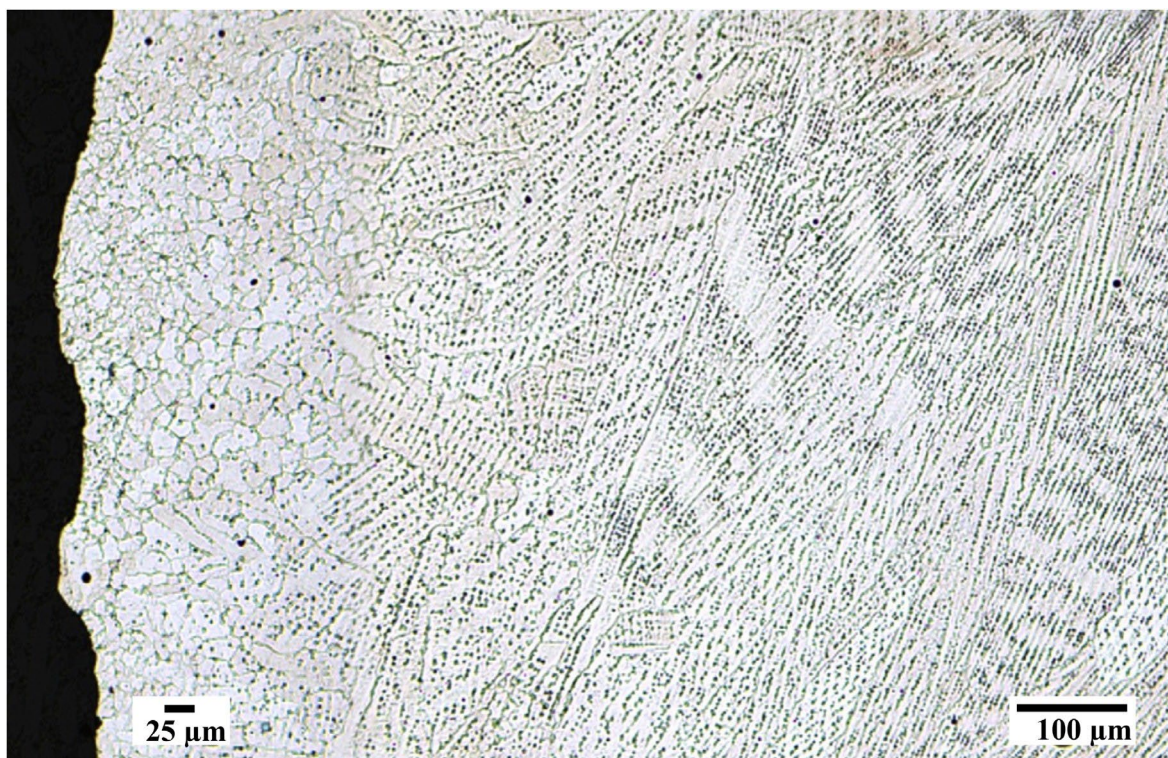


Figure 11. Close-up view of the dendritic structure in an as-built single-pass LP-DED NASA HR-1 panel. Fine grains are observed on the outer wall due to the rapid solidification.

### 3.2.2 Microstructure Evolution after Stress Relief and Homogenization

Figure 12 illustrates the microstructures of single-pass LP-DED NASA HR-1 panels after three different stress relief treatments. These panels were deposited at a laser power of 1070 watts with a single pass per layer that are parallel to the previous layer. The sample that received stress relief treatment at 1700 °F exhibits dominant dendritic structure similar to that of the as-built material. The dendritic morphologies were significantly weakened with increasing the stress relief temperature. Significant microstructure changes occurred when the stress relief temperature rose to 1800 °F. The dendritic structure has almost vanished, and the early stage of recrystallization has occurred after being heat treated at 1800 °F/1.5h. Stress relief at 1900 °F/1.5h led to a slightly higher degree of recrystallization but the grain structure remains very heterogeneous (see Figure 12(d)). During the LP-DED process, the rapid heating and cooling of the melt pools along with the molten metal volume change upon solidification result in buildup of residual stress in the parts. The driving force for recrystallization is the residual stress from the additive manufacturing process.<sup>17–19</sup> It is apparent that the residual stress for single-pass LP-DED NASA HR-1 is quite high that partial recrystallization occurs when the stress relief temperature is higher than 1800 °F.

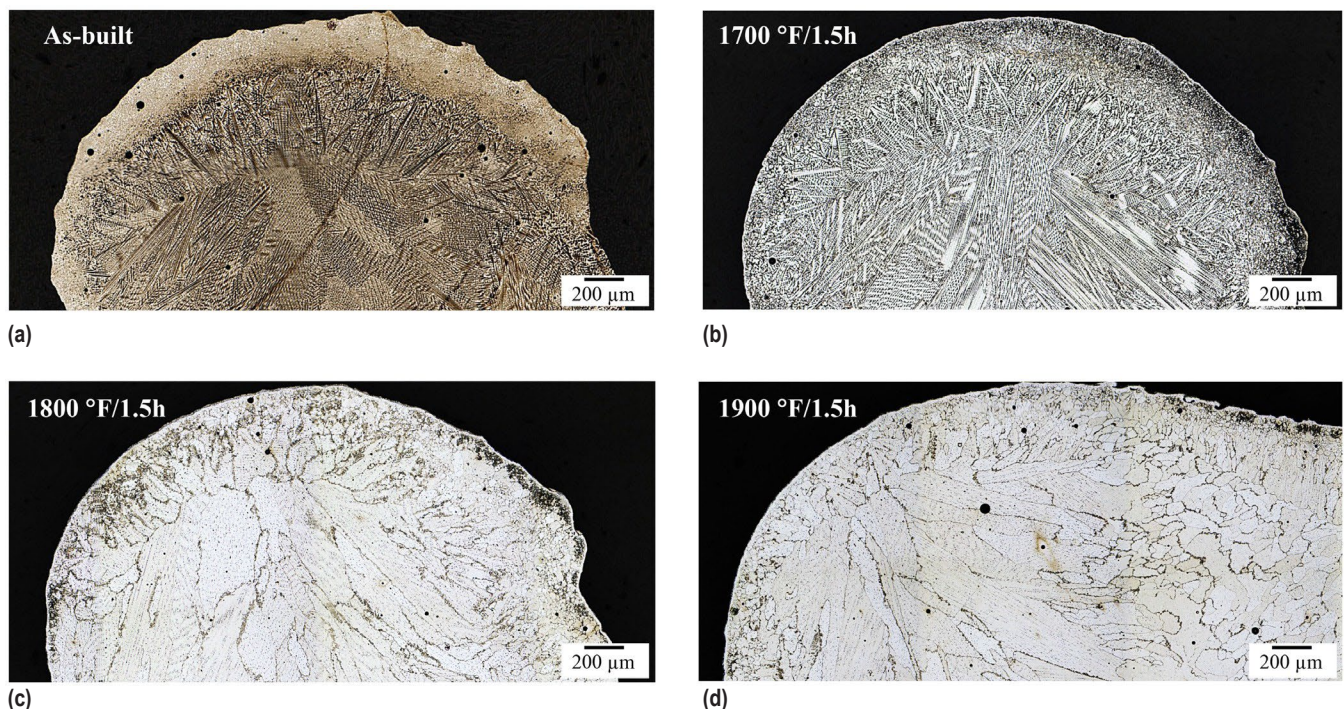


Figure 12. Effects of stress relief temperature on microstructure evolution for single-pass LP-DED NASA HR-1. The stress relief conditions are (a) as-built, (b) 1700 °F/1.5h, (c) 1800 °F/1.5h, and (d) 1900 °F/1.5h. These single-pass LP-DED panel was deposited at a laser power of 1070 watts with a thickness of approximately 3.175 mm.

After stress relief at 1800 °F/1.5h, the panel samples were subjected to a homogenization cycle of 2125 °F/3h. It is obvious that a high degree of recrystallization and grain growth had taken place after the homogenization treatment as shown in Figure 13. The grain size is quite large and many grains in the material are larger than 250 µm in diameter. The large grain structure can be attributed to the large melt pool dimensions in these single-pass LP-DED panels. It is worth noting that the homogenized sample displays smaller grains near the surface and larger grains toward the center regions. The uneven grain size distribution is caused by faster melt pool cooling rate at the part periphery than in the part center during the LP-DED process. Precipitation of the undesirable brittle  $\eta$ -phase ( $Ni_3Ti$ ) is very sensitive to the cooling rates after homogenization treatment. Upon the completion of the homogenization treatment, the samples were cooled rapidly through Ar quench method to mitigate precipitation of  $\eta$ -phase (Fig. 13). The as-homogenized sample appears free of  $\eta$ -phase.



Figure 13. Macrostructure of a 3.175 mm thick single-pass LP-DED NASA HR-1 panel after homogenization at 2175 °F/3h. The as-homogenized sample appears free of  $\eta$ -phase.

### 3.2.3 Precipitation of Grain Boundary $\eta$ -phase after Aging

NASA HR-1 is a  $\gamma'$  ( $Ni_3(Ti,Al)$ ) precipitation strengthened superalloy. The matrix phase,  $\gamma$ , is a solid solution of Fe, Ni, Co, Cr, Mo, and W, whereas the precipitate phase  $\gamma'$  is associated with the hardening elements, Ti and Al. In addition,  $\eta$  phase has been observed in the microstructure.  $\eta$  phase is a Ti rich acicular precipitate that generally forms at grain boundaries but does form within the grains with prolonged exposure at elevated temperatures. After homogenization treatment, the samples were solution annealed at 1800 °F/1h, followed by argon quenching. These samples were then aged at 1325 °F/16h to complete the heat treatment process for LP-DED NASA HR-1. As shown in Figure 14(a), the microstructure appears  $\eta$ -phase free after solution anneal. The parts were cooled rapidly from 1800 °F to ambient temperature by quenching in water to maintain  $\eta$ -phase free solid solution. However, precipitation of  $\eta$ -phase at grain boundaries occurred after the standard aging treatment at 1325 °F/16h as shown in Figure 14(b). It is postulated that dissolution of  $\eta$  phase had taken place at 1800 °F but Ti concentration at grain boundaries remained quite high. As a result, copious  $\eta$  phase precipitated along some grain boundaries after aging at 1325 °F/16h.

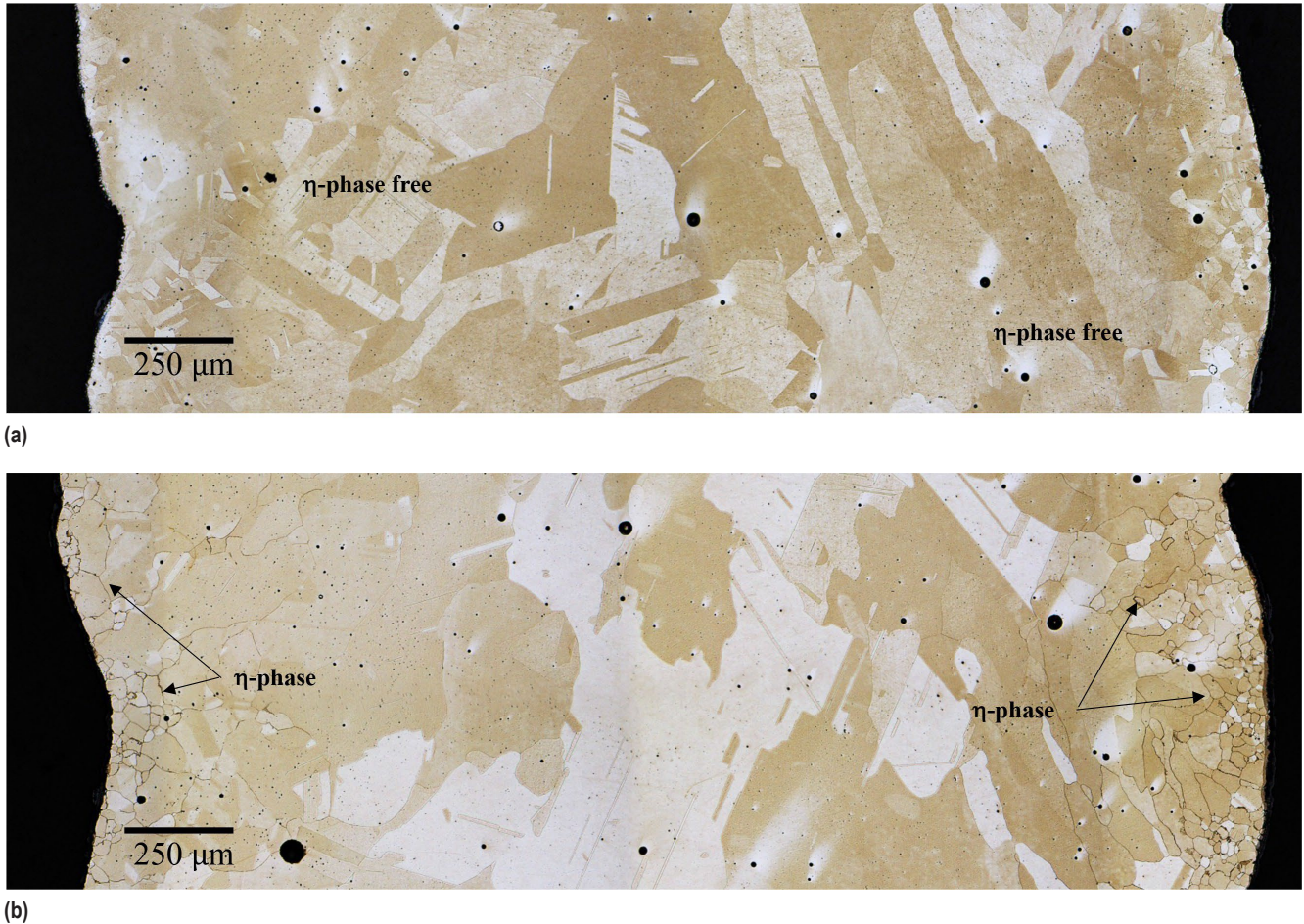


Figure 14. Macrostructure of 3.175 mm thick LP-DED NASA HR-1 after (a) solution anneal at 1800 °F/1h, and (b) aging treatment at 1325 °F/16h. Copious  $\eta$  phase precipitated along some grain boundaries after aging at 1325 °F/16h.

Close-up views of  $\eta$ -phase at grain boundaries in single-pass LP-DED NASA HR-1 (3.175 mm) panel is given in Figure 15. The  $\eta$ -phase in the 3.175 mm thick LP-DED panel has preferentially formed near the edges where the difference in grain size was observed, but it was seen to a lesser degree in the middle of panel sample after aging. However, grain-boundary  $\eta$ -phase is more evenly distributed through thickness in a thin single-pass (1 mm thick) LP-DED NASA HR-1 panel after the same aging treatment at 1325 °F/16h (see Fig. 16). The 1 mm thick single-pass LP-DED panel was deposited at a laser power of 350 watts. It is not clear as to what causes the uneven grain boundary  $\eta$  phase distribution in the 3.15 mm single-pass LP-DED panel.

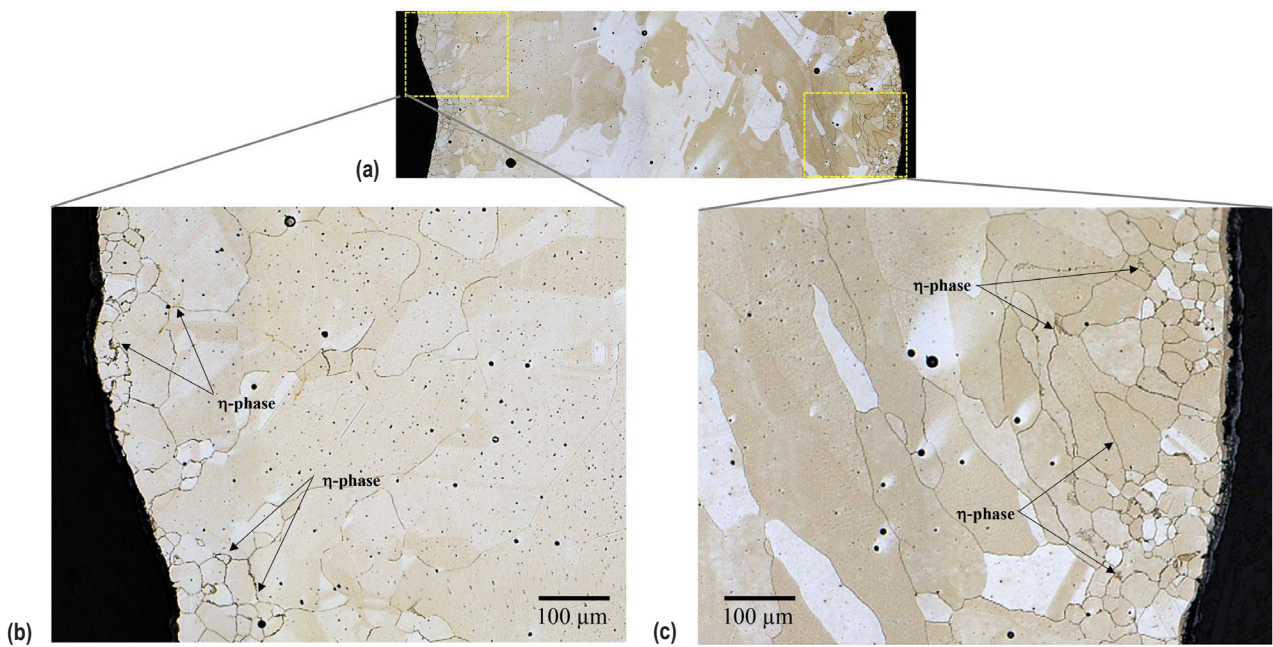


Figure 15. Closeup views of a LP-DED NASA HR-1 single-pass (3.175 mm thick) panel showing uneven distribution of grain-boundary  $\eta$ -phase after being aged at 1325 °F/16h.



Figure 16. Grain-boundary  $\eta$ -phase is more evenly distributed in a thin single-pass LP-DED NASA HR-1 panel (1 mm thick) after being aged at 1325 °F/16h. This 1 mm thick single-pass LP-DED panel was deposited at a laser power of 350 watts.

Following a solution anneal at 1800 °F/1h, wrought NASA HR-1 displays a very clean microstructure with no grain boundary  $\eta$ -phase precipitation after standard aging at 1325 °F/16h.<sup>5</sup> However, in LP-DED NASA HR-1, copious  $\eta$ -precipitation occurs at grain boundaries after aging at 1325 °F/16h. LP-DED NASA HR-1 has much higher Ti segregation that is not seen in wrought NASA HR-1.<sup>4</sup> The difference in Ti segregation can be attributed to the difference in the solidification rates between LP-DED and casting processes. For Fe-Ni-based superalloys, the prevalent nucleation sites for  $\eta$ -phase during aging treatment are the grain boundaries because  $\eta$ -phase has a hexagonal close-packed (HCP) structure that is non-coherent with the matrix.<sup>20</sup> The presence of grain-boundary  $\eta$  phase ( $Ni_3Ti$ ) in fully heat-treated LP-DED NASA HR-1 samples is a serious concern as  $\eta$ -phase is brittle and has a negative impact on tensile ductility, LCF life, and HEE resistance.

For LP-DED NASA HR-1, precipitation of undesirable grain-boundary  $\eta$ -phase can be mitigated by optimization of (1) chemical composition and (2) heat treatment. In general, the formation of  $\eta$ -phase is strongly related to (1) Ti/Al ratio, (2) Ti content, and (3) alloy composition.<sup>21</sup> When Ti/Al ratio is high, the Ti-rich  $\gamma'$  can transform to the  $\eta$ -phase during aging. Moreover, the volume fraction of  $\eta$ -phase generally increases with a greater Ti/Al ratio. In contrast, in an alloy with higher Ti content, the  $\eta$ -phase can easily form with a lower Ti/Al ratio. This indicates that both Ti/Al ratio and Ti content must be tailored to mitigate the formation of  $\eta$ -phase. Furthermore, mitigation of  $\eta$ -phase precipitation can be accomplished through heat treatment modification to reduce Ti segregation and retard  $\gamma'$  to  $\eta$ -phase transformation.<sup>4</sup> In addition to mitigating  $\eta$  precipitation to improve HEE resistance, the chemistry and heat treatment optimization efforts were also directed toward obtaining an optimal balance of the primary material properties (such as tensile strength, low cycle fatigue, and ductility) for LRE applications.

### 3.3 Obtaining an Optimal Balance of Five Important Material Properties

Liquid rocket engines operate in extreme and challenging environments in which the temperature can range from that of liquid hydrogen (-423 °F) to 6000 °F hot gas.<sup>22</sup> Component structures used in LREs require very thin walls in regeneratively-cooled nozzles that place great demands on materials selection as the structures must be able to endure enormous thermal shock during transients and large temperature differentials across walls during engine operation. Additionally, combining the environment with liquid and gaseous hydrogen propellant to the thermal and structural loads provides an even more complex challenge. For these applications, materials must be designed to resist Hydrogen Environment Embrittlement (HEE). In addition, there are also other key requirements to consider for LRE structural material selection, including tensile strength, ductility, low cycle fatigue (LCF) resistance, and thermal conductivity.<sup>3</sup> The importance of the key properties is shown below:

(I) Mechanical Strength – During the operation of LRE, the nozzle or chamber wall is subjected to high thermal load induced by huge temperature difference across the wall and the mechanical load caused by the pressure difference between the coolant-side wall and the hot-gas-side wall.<sup>23-25</sup> Yielding is expected as localized stress would be beyond the elastic limit and inelastic strain will accumulate in the plastically deformed regions. High strength is required so that the

materials have sufficient mechanical strength margin to support the thermal and mechanical loads in the components.

(2) Ductility – Due to the high thermal and mechanical loads on the components, the stress of LRE nozzles would be beyond the elastic limit, and severe plastic strains accumulate in the inner wall.<sup>23</sup> Cyclic plastic strain accumulates in the inner wall during multiple operations, which is known as thermal ratcheting.<sup>25</sup> Therefore, having high ductility is essential to prevent component failure caused by cyclic accumulation of plastic strain in the inner wall.<sup>24</sup>

(3) Low Cycle Fatigue (LCF) – Good resistance to low cycle fatigue (LCF) is essential for LRE nozzles as LCF is one of the most predominant failure modes.<sup>24–25</sup> During the cyclic operation of ambient temperatures (or sometimes chilling), transient startup, steady state, shut down transient, post-cooling and relaxation, the elastic-plastic deformation of channel wall nozzle induced by the synergy of high-speed hot gas and high-pressure cryogenic coolant results in residual strain. After many work cycles, the residual strain can accumulate to an extent that cracks begin to initiate in the cooling channels (typically in the hotwall, which has the highest strains). Hence, LCF is the primary service life limiting factor of regenerative cooling channel wall nozzles.<sup>25</sup>

(4) Hydrogen Environment Embrittlement (HEE) – Due to the use of high-pressure liquid hydrogen as propellant for some LREs, the selected LRE nozzle materials must resist Hydrogen Environment Embrittlement (HEE). The high-pressure liquid hydrogen coolant that enters the cooling channels absorbs heat and maintains wall temperatures low enough to prevent melting. The liquid hydrogen coolant warms up and gasifies, creating high pressure gaseous hydrogen environment in the cooling channels. HEE effects will become more pronounced when the channel inner hotwall temperature is between  $-100^{\circ}\text{C}$  to  $100^{\circ}\text{C}$ .<sup>26</sup> Therefore, having excellent resistance to HEE is one of the most important material selection criteria for LRE nozzle materials that operate in high pressure gaseous hydrogen environment.

(5) Thermal Conductivity – The nozzle wall is subjected to high heat flux from the combustion gases. To protect the nozzle wall, regenerative cooling must be applied by flowing a cryogenic liquid (or sometimes gaseous) propellant into the nozzle cooling channels to prevent the nozzle from melting. Therefore, nozzle materials must have high thermal conductivity to improve the cooling efficiency of cryogenic propellant and lower the nozzle temperature and thermal strain.<sup>23</sup>

These five key properties are all interrelated and must be taken into consideration when optimizing the formulation and heat treatment for LP-DED NASA HR-1. High strength materials tend to have issues with ductility, low cycle fatigue, and fracture toughness. After conducting a thorough assessment, it was determined that the most appropriate way to obtain an optimal compromise of the five important material properties is through a moderate strength reduction as shown in Figure 17. A moderate 10 – 15% strength reduction is expected to increase ductility, LCF life, and maintain good HEE resistance and thermal conductivity. To date, an optimal comprise of these five important material properties has been accomplished through optimization of alloy chemistry and heat treatment.

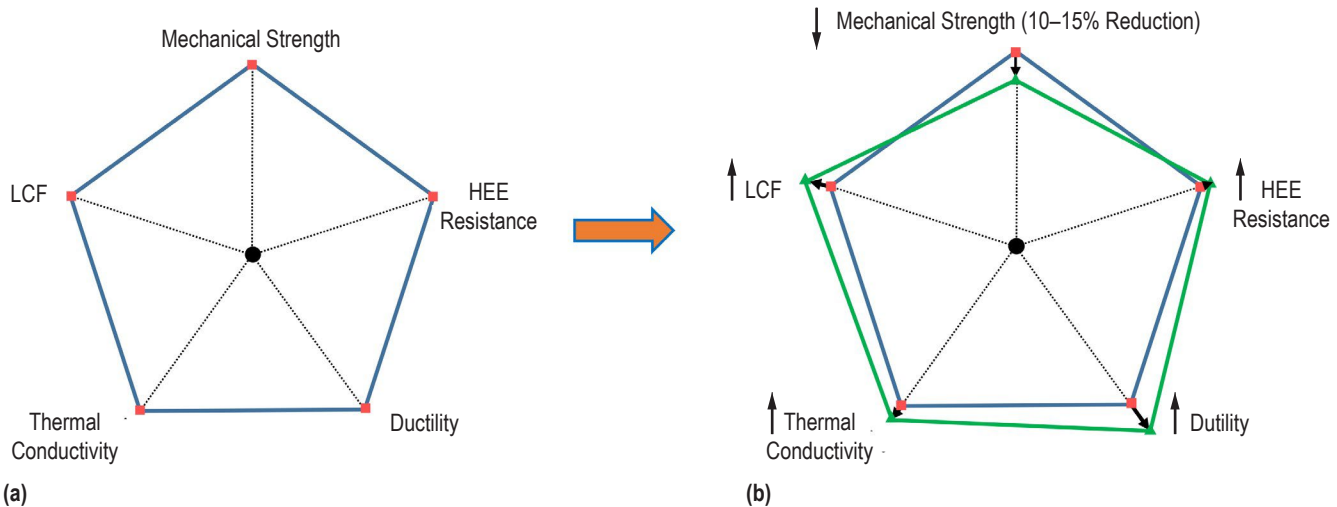


Figure 17. (a) The five (5) important material properties and (b) key trades to optimizing for a LRE nozzle application. The original formulation and heat treatment for LP-DED NASA HR-1 has been optimized to obtain an optimal comprise of these five materials properties.

### 3.3.1 Alloy Chemistry Optimization

The development of many historical superalloys was accomplished primarily by tedious trial-and-error approach.<sup>27</sup> Phase prediction using simple binary or ternary phase diagrams was not a viable option due to the complex nature of the highly alloyed superalloys and lack of computational tools at the time. A modern analytical tool that can be used to predict microstructure stability and formation of deleterious phases in superalloys is PHACOMP, which stands for PHAse COMPUTation. PHACOMP was developed by Morinaga et al. to predict austenite phase ( $\gamma$ ) stability vs TCP or GCP phase formation in Ni-base, Co-base and Fe-base alloys.<sup>28–33</sup> The PHACOMP concept was devised based on molecular orbital calculation (the discrete variational (DX)-X $\alpha$  cluster method) for transition-metal-based alloys. TCP stands for topologically-closed-pack intermetallic phases (e.g.  $\sigma$ ,  $\chi$ , and Laves phases), and GCP stands for geometrically closed-pack intermetallic phases (e.g.  $\eta$ ,  $\delta$  phases).<sup>34</sup> PHACOMP was successfully applied to control the formation of GCP phases, such as  $\eta$  phase, for the development of high-entropy alloys.<sup>35</sup> In brief, the PHACOMP method offers new approaches to advance the alloy design by estimating the solid solubility in superalloys to control the formation of undesirable TCP/GCP phases. PHACOMP uses a parameter, Md, which is an average d-electron energy above the Fermi energy level of alloying transition metals, to estimate the solid solubility of FCC (Face Centered Cubic)  $\gamma$  matrix. Overall, the alloy chemistry optimization for LP-DED NASA HR-1 follows the following criteria:

- Md level was kept close to that of JBK-75 to increase stability of the  $\gamma$  (austenitic) matrix that is essential to mitigate  $\eta$ -phase formation.
- Ni and Fe form the matrix of FCC  $\gamma$  phase, which acts as base or solvent for other elements in the alloy. A slight increase in Fe helps to depress Md. The Fe:Ni ratio was increased slightly to maintain high resistance to HEE.<sup>36</sup>

- Co was increased slightly to reduce Md. Co offers solid solution strengthening and can also increase the solid solubility for the  $\gamma'$  forming elements (Ti, Al) and retard  $\eta$ -phase formation.
- Cr was reduced slightly to reduce Md. Cr is mainly present in  $\gamma$  matrix and is a potent solid-solution strengthener. Cr promotes formation of the protective  $\text{Cr}_2\text{O}_3$  oxide layer that gives the alloy its hot corrosion resistance.
- W is an important refractory element that provides persistent solid-solution strengthening at elevated temperatures. W was reduced slightly to bring Md to a lower level. In NASA HR-1, a minimum of 1 wt% of W is required to provide adequate resistance to hydrogen embrittlement. Addition of W drastically reduces the stacking fault energy (SFE) of superalloys, which has been shown to decrease the susceptibility to hydrogen embrittlement for several binary transition metal alloys.<sup>37</sup>
- Mo was reduced slightly to bring Md to a lower level. Similar to W, Mo is also a refractory element that provides persistent solid-solution strengthening at elevated temperatures. A slight reduction in both Mo and W contents would reduce strength and improve ductility and LCF resistance.
- Ti and Al serve as the basis for the strengthening mechanism in Fe-Ni-base Superalloys as they combine with Ni to form the strengthening  $\gamma'$  precipitate ( $\text{Ni}_3(\text{Ti},\text{Al})$ ). Ti content and Ti/Al ratio were slightly reduced to mitigate  $\eta$ -phase formation and to obtain an optimal compromise of the five material properties through a moderate strength reduction.

In PHACOMP analysis, Md, which is an average d-electron energy above the Fermi energy level is calculated from the alloy composition. The Md values for various commonly used transition alloying elements in fcc Ni are listed in Table 4. Al and Si are non-transition metals and their Md values are empirically determined from interpolation of the curve of Md versus the metallic radius.<sup>38</sup>

Table 4. List of Md values for various elements in FCC Ni.<sup>38</sup>

Element		Md (eV)	Element		Md (eV)	Element		Md (eV)
3d	Ti	2.271	4d	Y	3.817	5d	Hf	3.020
	V	1.543		Zr	2.944		Ta	2.224
	Cr	1.142		Nb	2.117		W	1.655
	Mn	0.957		Mo	1.550		Re	1.267
	Fe	0.858		Tc	1.191		Os	1.063
	Co	0.777		Ru	1.006		Ir	0.907
	Ni	0.717		Rh	0.898		Others	Al
	Cu	0.615						Si
								1.900

For an alloy, the average value of  $M_d$  is defined by taking the compositional average and can be calculated using the Equation below.

$$M_d = \frac{\sum_{i=1}^n X_i (M_d)_i}{\sum_{i=1}^n X_i} \quad (1)$$

where

$M_d$  = average  $M_d$  parameter

$X_i$  = the atomic fraction of the element  $i$  in the  $\gamma$  matrix

$n$  = the number of elements in the alloy

$(M_d)_i$  = the  $M_d$  value for element  $i$

The summation is taken over all the alloying elements,  $i=1,2,\dots,n$ . For simplicity, the unit of  $M_d$  parameter, eV, is omitted in this paper. When  $M_d$  increases beyond a critical value, the  $M_d$  method assumes that the phase instability will occur and a secondary phase will appear in a terminal solid solution. In other words, the critical  $M_d$  determines the solubility limit of  $\gamma$  matrix. This  $M_d$  Equation can be expressed empirically based on the atomic concentration of the alloying elements in the overall alloy composition. For example, the  $M_d$  value for the final formulation (previously named Revision 3) LP-DED NASA HR-1 is calculated as follows:

$$\begin{aligned} M_d &= (M_d)_{Fe} \times X_{Fe} (\text{Fe atomic fraction}) + (M_d)_{Ni} \times X_{Ni} (\text{Ni atomic fraction}) + (M_d)_{Cr} \times X_{Cr} (\text{Cr atomic fraction}) \\ &\quad + (M_d)_{Mo} \times X_{Mo} (\text{Mo atomic fraction}) + (M_d)_V \times X_V (\text{V atomic fraction}) + (M_d)_W \times X_W (\text{W atomic fraction}) + (M_d)_{Co} \times X_{Co} (\text{Co atomic fraction}) + (M_d)_{Ti} \times X_{Ti} (\text{Ti atomic fraction}) + (M_d)_{Al} \times X_{Al} (\text{Al atomic fraction}) \\ &= 0.858 \times 0.4204 (\text{Fe at\%}) + 0.717 \times 0.3300 (\text{Ni at\%}) + 1.142 \times 0.1600 (\text{Cr at\%}) + 1.55 \times 0.0107 (\text{Mo at\%}) + 1.543 \times 0.0034 (\text{V at\%}) + 1.655 \times 0.0050 (\text{W at\%}) + 0.777 \times 0.0367 (\text{Co at\%}) + 2.271 \times 0.0268 (\text{Ti at\%}) + 1.900 \times 0.0053 (\text{Al at\%}) = 0.9134 \end{aligned}$$

Similar calculations were performed for other alloys to yield the  $M_d$  values. PHACOMP can determine a critical  $M_d$  value, above which microstructure instability occurs. Currently, the critical  $M_d$  value that must be kept below to avoid  $\eta$ -phase formation for NASA HR-1 is not known. Since  $\eta$ -phase in A-286 and JBK-75 can be kept to a very low level after heat treatment, the  $M_d$  levels of A-286 and JBK-75 were used as the estimated critical threshold value for LP-DED NASA HR-1. Therefore, the  $M_d$  values for LP-DED NASA HR-1 was kept very close to that of A-286 and JBK-75 to improve the  $\gamma$  matrix stability. Another important consideration for the LP-DED NASA HR-1 composition modification is its excellent HEE resistance should not be altered.

Based on the above approaches, the chemical composition for LP-DED NASA HR-1 has been optimized as shown in Table 5. The initial and final formulation of LP-DED NASA HR-1 was previously named “revision 2” and “revision 3”, respectively for internal use. Due to the reduction in  $M_d$  value, LP-DED NASA HR-1 final formulation is expected to have better microstructure stability than the initial formulation. Figure 18 compares the  $M_d$  values for the alloys listed in Table 5. LP-DED NASA HR-1 final formulation (revision 3) is the composition that has been optimized to obtain an optimal balance of primary material properties for LRE nozzles. The reduction of Ti content and the overall  $M_d$  value is expected to retard precipitation of undesirable grain boundary  $\eta$ -phase and achieve an optimal balance of the primary material properties for LRE applications.

Table 5. Nominal chemical composition (wt%) for wrought and LP-DED NASA HR-1. The Md levels of A-286 and JBK-75 were used as the estimated the critical threshold value for LP-DED NASA HR-1.

Alloy	Fe	Ni	Cr	Mo	V	W	Co	Ti	Al	Mn	Md
Wrought NASA HR-1	38.90	34.10	15.50	2.40	0.30	2.20	3.50	2.80	0.30	—	0.928
LP-DED NASA HR-1 *Initial Formulation	39.80	34.00	15.50	2.20	0.32	2.10	3.30	2.50	0.25	—	0.922
LP-DED NASA HR-1 *Final Formulation	41.20	34.00	14.60	1.80	0.30	1.60	3.80	2.40	0.25	—	0.913
Wrought A-286	55.20	25.00	15.00	1.30	0.30	—	—	2.00	—	1.50	0.912
Wrought JBK-75	51.13	30.20	14.75	1.25	0.30	—	—	2.10	0.25	—	0.910

\*The initial and final formulations are also known as “revision 2” and “revision 3” compositions for internal use and comparison to some previous documentation.

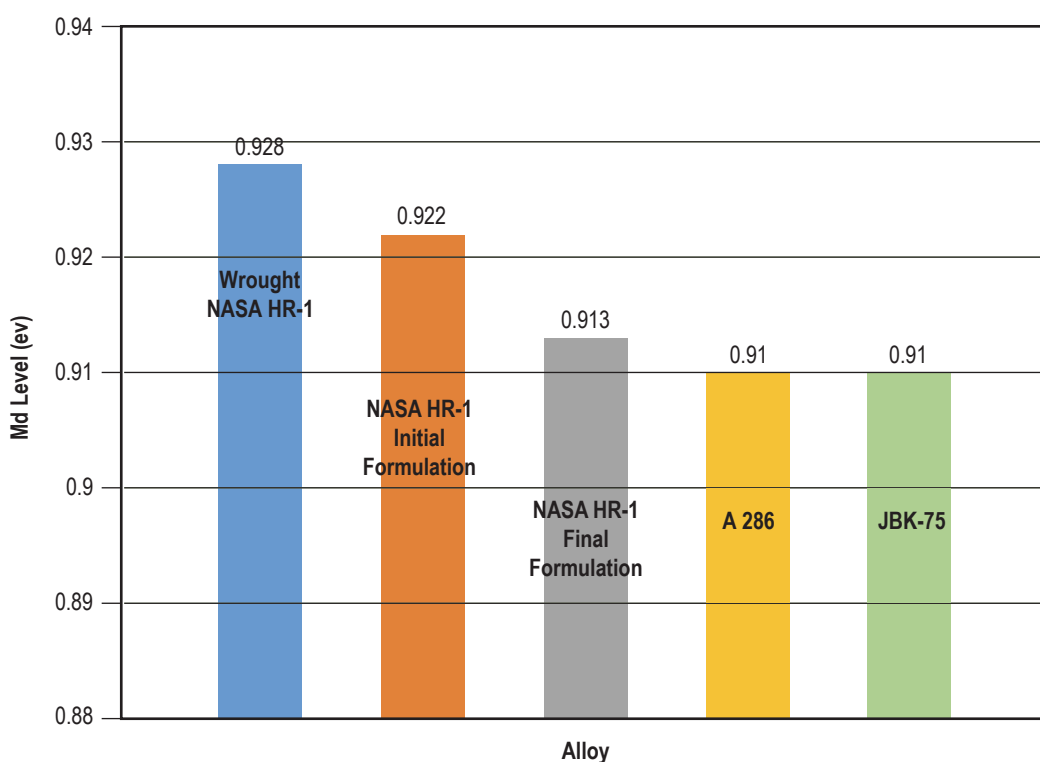


Figure 18. Md comparison for wrought NASA-HR-1, LP-DED NASA HR-1 initial formulation, final formulation, wrought A-286, and wrought JBK-75.

### 3.3.2 Heat Treatment Optimization

During metal additive manufacturing (AM) process, the material is deposited layer by layer by a high-power laser beam and is subjected to a complex thermal cycle that includes rapid heating above the melting temperature and rapid cooling and solidification of the molten material. Thus, the AM material often has heterogeneous microstructures, and non-uniform chemical composition and phase distribution.<sup>2-3</sup> These characteristics make it difficult to produce AM parts with materials properties and microstructures that are as reproducible as same alloys produced by conventional wrought process. Once the composition of wrought NASA HR-1 was modified for the LP-DEN alloy using the PHACOMP method, attention was directed toward heat treatment optimization.

The as-deposited LP-DEN NASA HR-1 has a high degree of titanium segregation in the interdendritic regions. Titanium segregation promotes precipitation of  $\eta$ -phase ( $Ni_3Ti$ ) at grain boundaries that is detrimental to tensile ductility, LCF life, and resistance to hydrogen environment embrittlement. Therefore, a new heat treatment was developed to minimize titanium segregation and  $\eta$ -phase precipitation for LP-DEN NASA HR-1. A heat treatment investigation plan was put together based on the homogenization kinetic analysis as shown in Table 6. A higher temperature stress relief at 1950 °F was attempted to understand the effects of stress relief temperature on grain structure evolution. Homogenization treatment was extended for times up to 12 hours at 2125 °F. It is a great concern that the standard solution anneal temperature of 1800 °F was too close to the upper boundary of the  $\eta$ -phase TTP diagram.<sup>39</sup> Therefore, higher solution anneal temperature was also attempted at 1950 °F to ensure  $\eta$ -phase is completely dissolved and Ti concentration at grain boundary is reduced to a very low level prior to the final aging treatment.

Table 6. Heat treatment investigation plan intended to reduce Ti segregation and  $\eta$ -phase precipitation at grain boundaries for LP-DEN NASAHR-1.

	Stress Relief (°F/h)			Homogenization (°F/h)			Solution Anneal (°F/h)		
	1800/1.5	1950/1.5	1950/3	2125/3	2125/6	2125/12	1800/1	1950/1	1950/3
Standard Heat Treatment	✓			✓			✓		
Heat Treatment Investigation		✓	✓		✓	✓		✓	✓

**3.3.2.1 Effects of Stress Relief on Microstructure Evolution.** Stress relief treatment is intended to relieve internal residual stress and strain energy and must be performed at an elevated temperature that can activate the recovery process. During stress relief treatment, atomic diffusion takes place and atoms in regions of high stress move to regions of lower stress. Significant microstructure changes occur when the stress relief temperature exceeds 1800 °F. Recrystallization during stress relief is desirable for LP-DEN NASA HR-1 to transform the as-built coarse

columnar dendritic structure to finer and more equiaxed grain structure. Varying degree of recrystallization occurred when the material was heat treated at 2125 °F after stress relief. As shown in Figure 19, the grain structure evolution after HIP (2125 °F/3h + furnace cooling) is sensitive to the stress relief temperature. The grain structure is finest for the samples that received stress relief treatment at 1900 °F/1.5h. It is apparent that higher stress relief temperature prior to HIP promotes recrystallization and decreases grain size. Similar grain size reduction was accomplished when LP-DED NASA HR-1 was stress relieved at 1950 °F/1.5h and followed by a homogenization treatment at 2125 °F/3h.<sup>40</sup> One of the most important effects of post-processing heat treatment for AM materials is microstructure refinement. It is desirable to have finer and more equiaxed grain structure. Therefore, 1950 °F/1.5h was chosen as the stress relief treatment for LP-DED NASA HR-1.

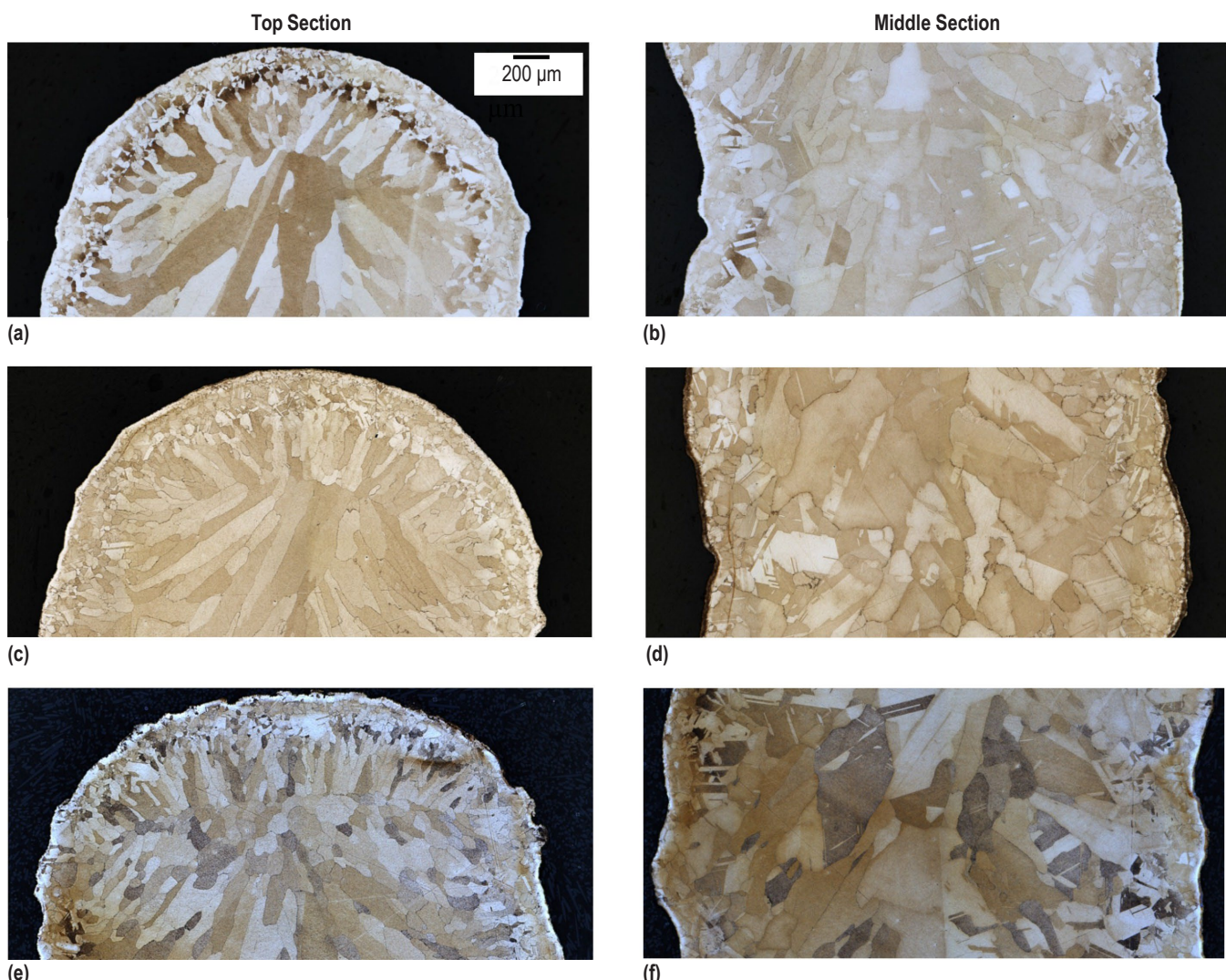


Figure 19. Varying degree of recrystallization occurred when the material was HIPed at 2125 °F after stress relief. These samples were stress relieved at 1700 °F for (a) and (b), 1800 °F for (c) and (d), 1900 °F for (e) and (f) before HIP.

**3322 Reduction of Ti Segregation through Homogenization.** One of the most important considerations for post-processing heat treatment is the control of grain structure. It is desirable to have finer and more equiaxed grain structure. Stress relief causes recovery and some degree of recrystallization. Variation in grain structure evolution after stress relief results from the competition between the recovery process and the concurrent recrystallization. The driving force for recrystallization is the thermal residual stresses that are introduced from the LP-DED process. Lower temperature stress relief extended the recovery process and reduced the driving force for recrystallization. Higher stress relief temperature promotes recrystallization and suppresses the recovery process. When the stress relief temperature is increased to 1900 °F and above, recovery process is largely suppressed, and the number of active recrystallization nuclei increases, leading to smaller and more equiaxed grain structure after homogenization treatment at 2125 °F. Finer, more equiaxed and more evenly distributed grain structure can improve overall mechanical properties, reducing the anisotropy in mechanical properties. Therefore, selecting an optimal combination of stress relief and homogenization treatments to minimize recovery process and promote recrystallization is a significant method to consider for LP-DEN NASA HR-1.

Evolution of titanium segregation evolution in LP-DEN NASA HR-1 after LP-DEN deposition and post-processing homogenization has been investigated in detail.<sup>4</sup> It was found that titanium segregation migrates from the interdendritic regions (in as-built LP-DEN material) to grain boundaries after homogenization treatment. A basic model for titanium diffusion in NASA HR-1 was developed to project concentration distribution of titanium as a function of homogenization temperature, duration, and grain size. The results of the homogenization kinetic analysis provide a valuable reference on how the homogenization treatment should be adjusted for LP-DEN NASA HR-1. The degree of homogenization of an alloy can be calculated by the value of residual segregation index,  $\delta$  as shown below:<sup>4</sup>

$$\delta = \left( \frac{C_{\text{max}} - C_{\text{min}}}{C_{0\text{max}} - C_{0\text{min}}} \right) = \exp \left( -\frac{Dt\pi^2}{L^2} \right) \quad (2)$$

$C_{0\text{max}}$  and  $C_{0\text{min}}$  represent the grain-boundary solute atom concentration (highest concentration) and the grain center solute atom concentration (lowest concentration) before the start of homogenization.  $C_{\text{max}}$  and  $C_{\text{min}}$  are the grain-boundary solute atom concentration and the grain center solute atom concentration after performing the homogenization treatment for a duration,  $t$ .  $D$  is the diffusion coefficient of Ti in the matrix, and  $L$  is half wavelength of Ti concentration (segregation). The time required to reach the desired homogenization level (or the residual segregation index,  $\delta$ ) can be expressed as the Equation below:<sup>4</sup>

$$t = -\frac{L^2 \ln \delta}{\pi^2 D_0} \exp \left( -\frac{Q}{R T} \right) \quad (3)$$

$D_0$  is the diffusion constant ( $\text{m}^2/\text{s}$ ),  $Q$  is the diffusion activation energy ( $\text{J}/\text{mole}$ ),  $R$  is the gas constant ( $8.31 \text{ J}/\text{mole}\cdot\text{K}$ ), and  $T$  is the thermodynamic temperature ( $^\circ\text{K}$ ). It is significant to note that a two-fold decrease in the segregation wavelength ( $L$ , equivalent to half of the grain diameter) would result in a four-fold decrease in the homogenization time ( $t$ ). The homogenization

process for LP-DED NASA HR-1 is mainly focused on the diffusion of Ti atoms from a higher concentration location at grain boundaries to the lower concentration location at grain center.

Figure 20 shows the predicted homogenization kinetics (Ti diffusion) for LP-DED NASA HR-1 to reach the residual segregation index ( $\delta$ ) of 0.1. It can be clearly seen that homogenization time decreases with an increase of homogenization temperature for the same grain size. Small grain size (lower L value) has a great advantage in achieving homogeneous microstructure in shorter time than that in large grain material. The standard homogenization treatment for LP-DED NASA HR-1 is 2125 °F/3h. According to the homogenization kinetics curves, to reach the target residual segregation index ( $\delta$ ) of 0.1, the combinations of temperature and time are 2125 °F/5.3h and 2125 °F/14.8h for grain size of 60  $\mu\text{m}$  ( $L=30 \mu\text{m}$ ) and 100  $\mu\text{m}$  ( $L=50 \mu\text{m}$ ), respectively. Based on the homogenization kinetic analysis, it is apparent that homogenization at 2125 °F/3h was not adequate for LP-DED NASA HR-1 parts that have many grains (larger than 100  $\mu\text{m}$  in diameter).

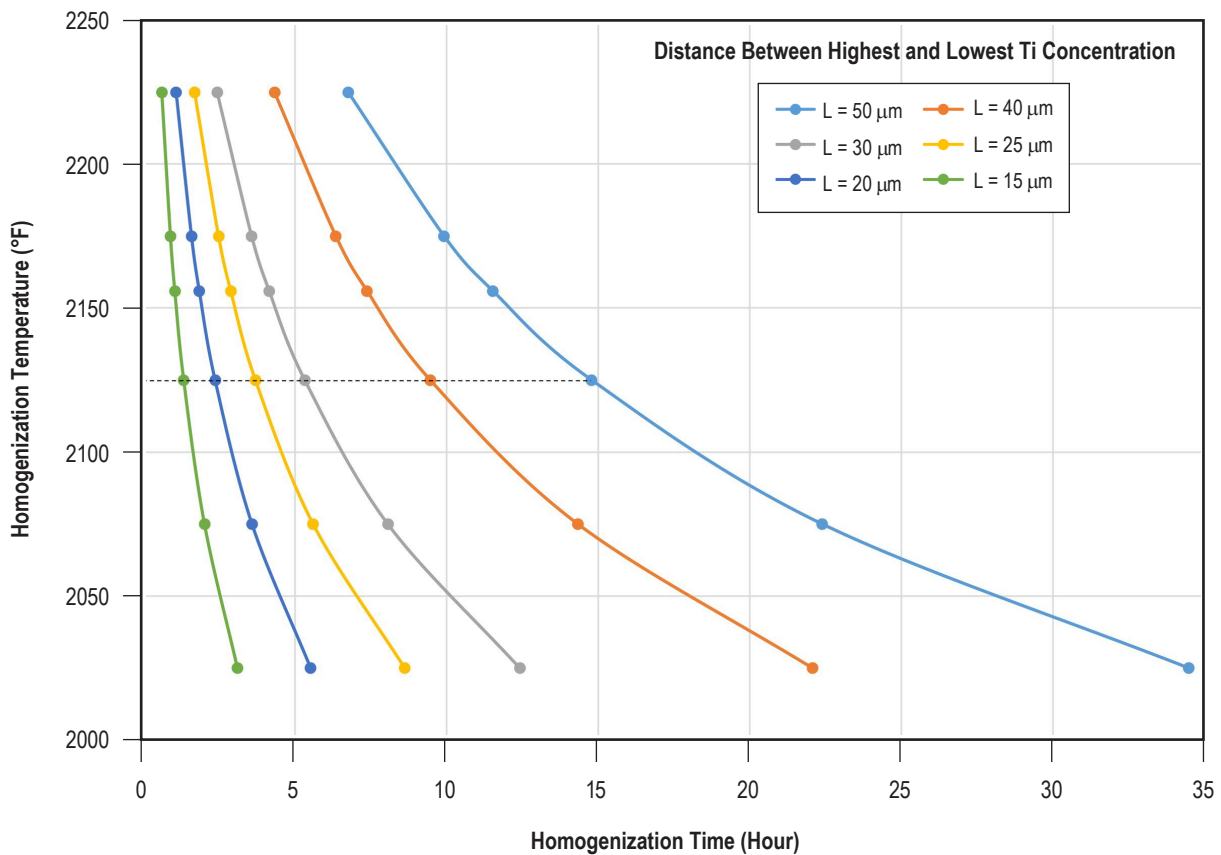


Figure 20. The predicted homogenization kinetic curves for LP-DED NASA HR-1 to reach the residual segregation index ( $\delta$ ) of 0.1. The homogenization time decreases with an increase of the homogenization temperature for the same grain size.

The main alloying elements distribution across the columnar dendrites was determined by EDS line scans. Figure 21 shows an example of Ti segregation in an as-built 1.00 mm thick single-pass LP-DED NASA HR-1 panel (built with 350 watts laser power). A large variation in Ti concentration can be clearly seen over a 1200  $\mu\text{m}$  distance. The nominal 2.5 wt% Ti varies considerably between a minimum of 0.0% to a maximum of about 10%. A close-up view for Ti concentration up 8% (Fig. 21(b)) reveals that Ti concentration fluctuates intensely between 0.3 to 6% in many locations.

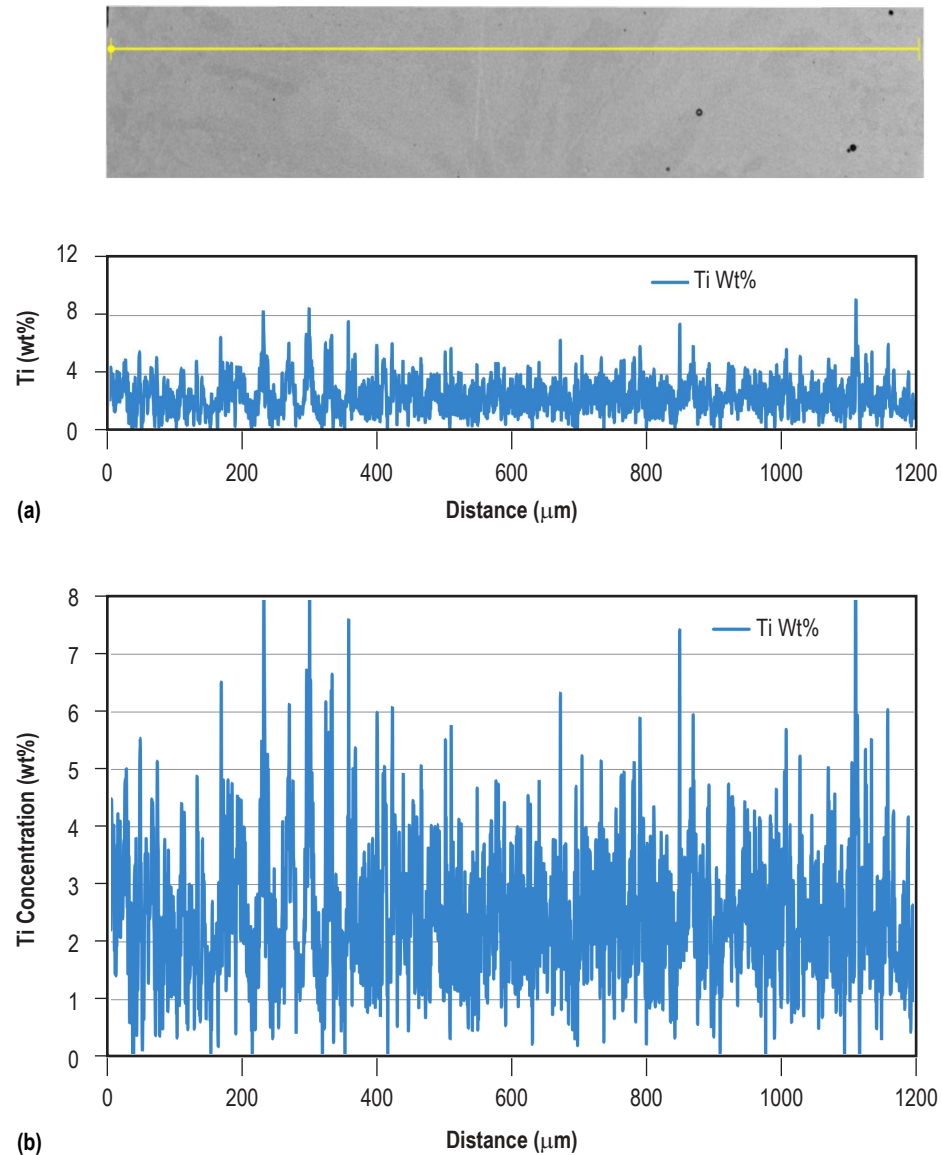


Figure 21. (a) An EDS line scan on an as-built 1.0 mm thick single-pass LP-DED NASA HR-1 panel (built with 350 watts laser power) showing titanium concentration fluctuates intensely between 0 to 10% in some locations. (b) A close-up view of EDS line scan data revealing titanium concentration fluctuates intensely between 0.3 to 8% in many locations.

Ti segregation amplitude can be greatly reduced by increasing the homogenization time at 2125 °F. Figure 22 shows Ti concentration profile in 1mm thick single-pass LP-DED NASA HR-1 panels that were homogenized at 2125 °F for 3, 6, and 12 hours. As shown in Figure 22(a), the fluctuation of Ti concentration amplitude was reduced from 0.3 – 8% (in the as-built condition) to approximately 1.0 – 4.5% after homogenization at 2125 °F/3h. Ti concentration is still significantly higher than the nominal 2.5 wt% in many locations. An increase of the homogenization time to 6 hours leads to noticeable improvement in Ti segregation as shown in Figure 22(b). After homogenization at 2125 °F/6h, titanium segregation amplitude decreased further and most Ti peaks fluctuated in the range of 1.0 – 3.5%. However, further increase of the homogenization time to 12 hours leads to only marginal improvement in Ti segregation amplitude as shown in Figure 22(c).

The EDS line scan results clearly indicate the standard homogenization treatment at 2125 °F/3h is not adequate to reduce titanium segregation to an acceptable level for LP-DED NASA HR-1. Due to the coarse grain structure in LP-DED NASA HR-1, higher homogenization temperature or longer duration should be performed in order to reduce Ti segregation to a very low level.<sup>4</sup> However, the use of a temperature higher than 2125 °F is not be recommended due to the increased risks of surface oxidation, grain growth and potential growth of internal pores. Performing a homogenization treatment at 2125 °F for durations longer than 12 hours cannot be justified either as reduction of Ti segregation becomes very sluggish after the initial 6 hours at 2125 °F. Therefore, 2125 °F/6h was selected as the new homogenization treatment for LP-DED NASA HR-1.

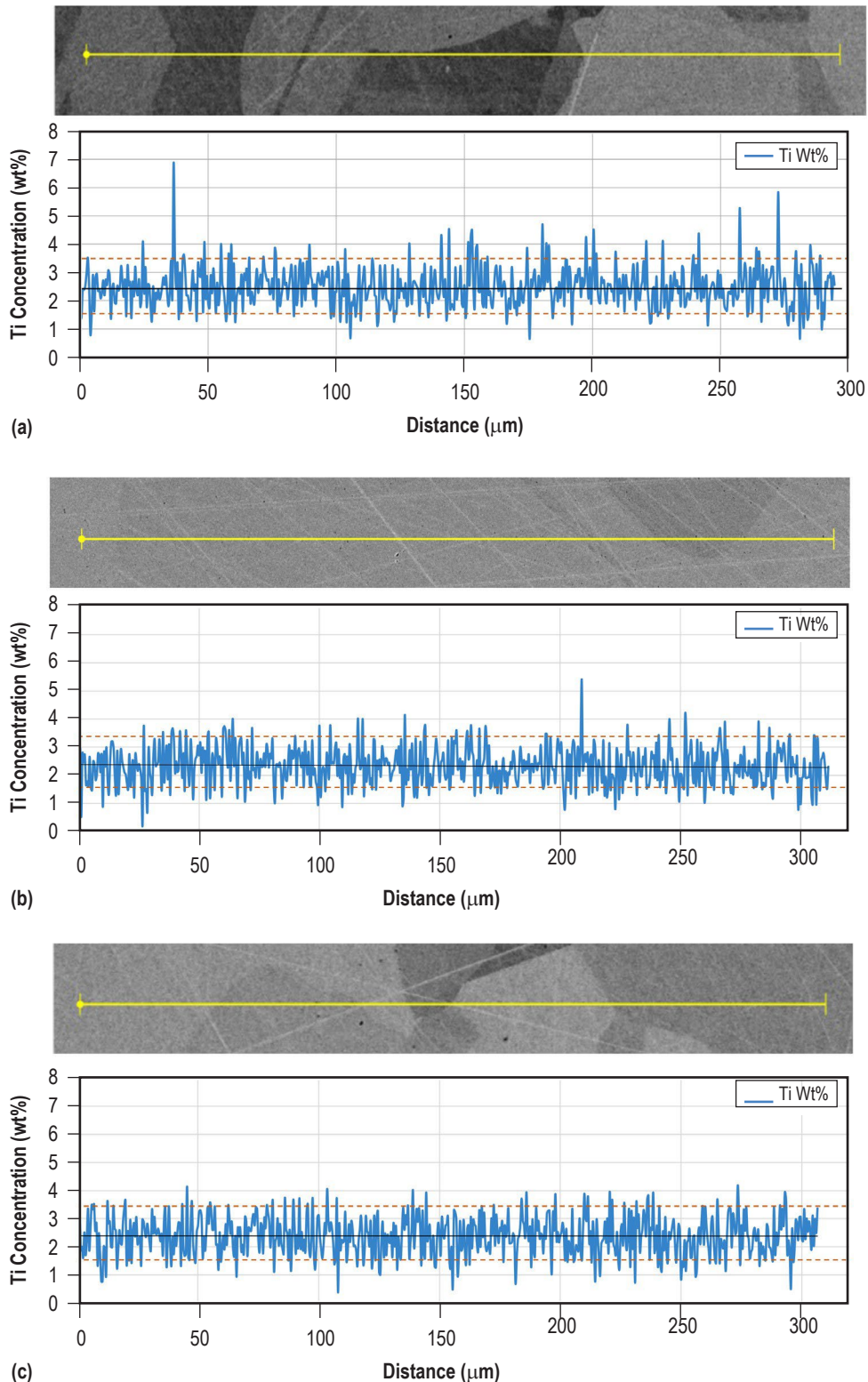


Figure 22. The evolution of titanium concentration profile for a 1.0 mm thick single-pass LP-DED NASA HR-1 panel (built with 350 watts laser power) after homogenization at (a) 2125 °F/3 h, (b) 2125 °F/6 h, and (c) 2125 °F/12 h.

High Ti segregation at grain boundaries is not normally seen in wrought NASA HR1 [5]. The difference in grain-boundary Ti segregation between LP-DED NASA HR-1 and the wrought alloy can be attributed to the difference in the solidification rates between LP-DED and casting processes. Comparing to the LP-DED process, the casting process has much slower cooling (solidification) rate that allows for prolonged cooling time, permitting the slow-to-diffuse elements (such as Ti) to disperse more homogeneously. NASA HR-1 castings usually receive homogenization treatment at elevated temperatures for 24 hours, which is significantly longer than the recommended 2125 °F/6h for LP-DED NASA HR-1. Additionally, the chemical inhomogeneity in wrought NASA HR-1 can be further reduced to a very low level by thermo-mechanical processes such as hot rolling and forging. Thus, extended homogenization treatment coupled with thermo-mechanical process drastically reduced Ti segregation and the propensity to form the detrimental  $\eta$ -phase at grain boundary in LP-DED NASA HR-1.

**3323 Mitigation of  $\eta$ -phase Precipitation through Solution Anneal and Aging.** After homogenization, solution anneal and aging processes are performed sequentially to precipitate and grow the strengthening  $\gamma'$  precipitate ( $Ni_3(Ti,Al)$ ). NASA HR-1 is a precipitate hardened material and solution anneal should be performed above the  $\eta$ -phase solvus temperature to dissolve the undesirable  $\eta$ -phase that forms during cooling from homogenization treatment. The standard solution anneal for LP-DED NASA HR-1 is 1800 °F/1h, which is only approximately 50 °F above the  $\eta$ -phase solvus temperature.<sup>39</sup> Therefore, solution anneal temperature was increased to 1950 °F to ensure complete dissolution of  $\eta$ -phase, followed by a quench. Another advantage of conducting SA at 1950 °F is that Ti segregation amplitude can be slightly reduced according to the homogenization kinetic analysis.<sup>4</sup>

The standard aging treatment for wrought NASA HR-1 is 1325 °F/16h. It was discovered that the standard single-step aging treatment at 1325 °F/16h was unable to reduce the precipitation of brittle  $\eta$ -phase ( $Ni_3Ti$ ) to an acceptable level for LP-DED NASA HR-1, primarily due to high magnitude of localized Ti segregation. Figure 23 shows precipitation of  $\eta$ -phase at grain boundaries when aging treatment was performed at 1325 °F, 1300 °F, and 1275 °F. Grain boundaries are  $\eta$ -phase free after solution anneal at 1800 °F/1h as shown in Figure 23 (a). Abundant  $\eta$ -phase precipitated at grain boundaries after aging at 1325 °F/24h. The volume fraction of grain-boundary  $\eta$ -phase decreases significantly when the aging temperature was lowered to 1300 °F (Fig. 23 (c)). Only a few isolated  $\eta$ -phase was present at grain boundaries after aging at 1275 °F/16h (Fig. 23 (d)). It is apparent that the amount of grain-boundary  $\eta$ -phase decreases with a reduction in aging temperature. Therefore, 1275 °F was selected as the 1<sup>st</sup> step aging temperature.

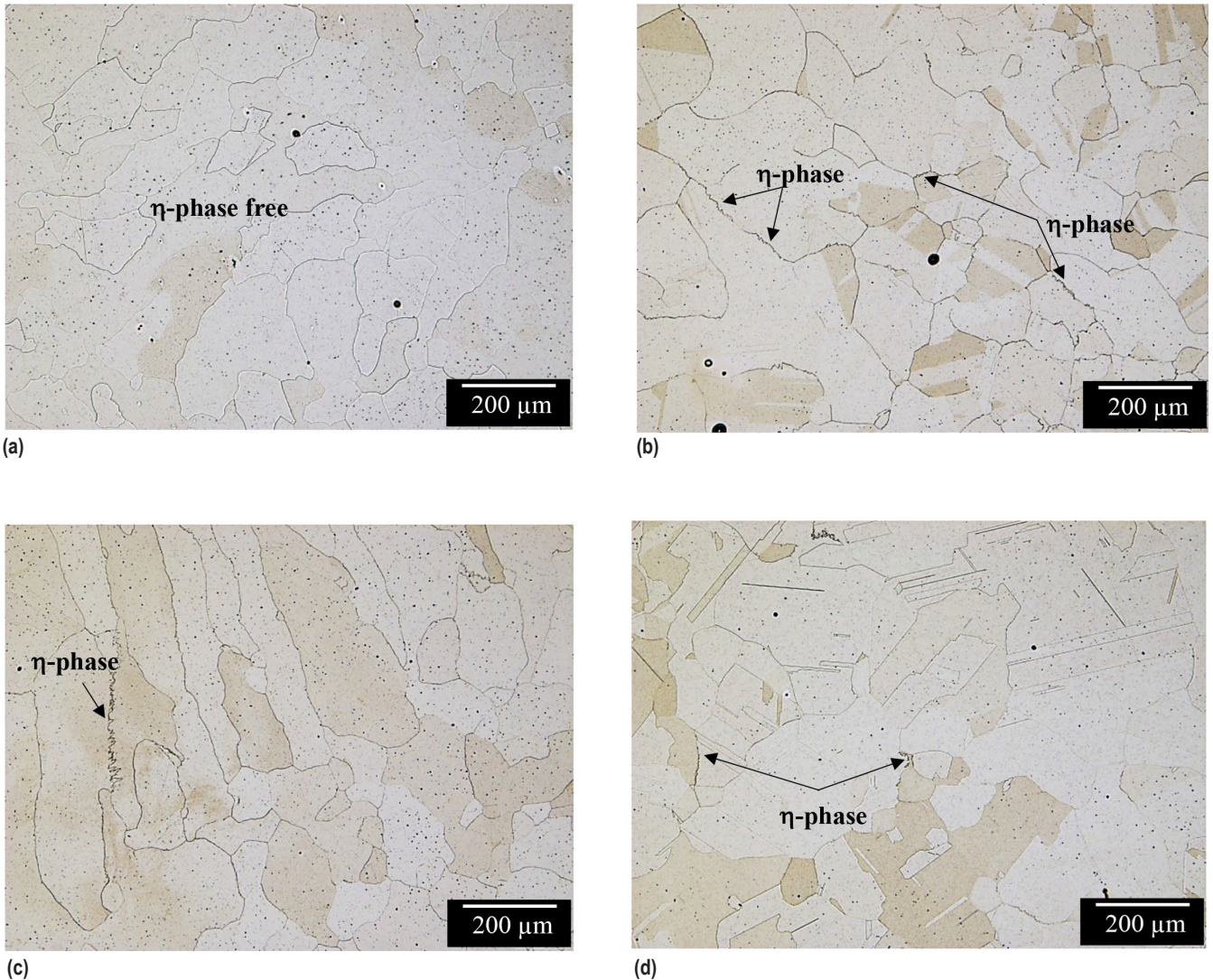


Figure 23. Precipitation of grain-boundary  $\eta$ -phase after (a) solution anneal, (b) aging at 1325 °F/24h, (c) aging at 1300 °F/24h, and (d) aging at 1275 °F/16h.

Lowering the aging temperature to 1275 °F is expected to slow down the kinetics of  $\gamma'$  precipitation and result in a significant reduction in tensile strength. In order to keep the strength reduction within a moderate 10 – 15% range, the standard single-step aging treatment must be modified into a 2-step aging process. Two-step aging treatment is commonly used for age-hardenable superalloys to maximize strength and to develop the best combination of short-term tensile and long-term creep properties.<sup>41</sup> In  $\gamma'$ -strengthened superalloys, the 1<sup>st</sup> aging treatment (higher temperature) precipitates secondary  $\gamma'$  precipitates and finer secondary or tertiary  $\gamma'$  precipitates during the 2<sup>nd</sup> step aging (lower temperature).<sup>42,43</sup> The most important mechanism of  $\eta$ -phase precipitation during aging treatment is  $\gamma' \rightarrow \eta$  transformation. The 2-step aging treatment is specifically designed to improve the microstructure stability to retard  $\gamma' \rightarrow \eta$  transformation during aging

treatment. Two promising 2-step aging treatments, 1275 °F/16h + 1200 °F/16h and 1275 °F/16h + 1150 °F/16h, were selected for further evaluation through tensile testing.<sup>44</sup> The most promising 2-step aging treatment would be chosen after performing an in-depth analysis on tensile data, which includes yield strength, ultimate tensile strength, ductility, and strain hardening exponent.

### 3.3.3 Effects of Heat Treatment on Tensile Properties

To examine the impacts of heat treatments on mechanical properties, tensile tests were performed using LP-DED NASA HR-1 samples build with different deposition parameters that could be used to produce parts. All samples were subjected to stress relief at 1800 °F/1.5h, homogenization treatment at 2125 °F/3h, and solution anneal at 1800 °F/1h, prior to aging treatment. Four aging treatments were selected for tensile property evaluation as shown in Table 7. The standard aging treatment for wrought NASA HR-1, 1325 °F/16h, was included as the baseline for comparison with the other three aging treatments. All tests were performed in air at room temperature with the as-deposited wall thickness and diameter shown in Table 7. The most promising 2-step aging treatment was chosen after performing an in-depth analysis on tensile data, which includes yield strength, ultimate tensile strength, ductility, and strain hardening exponent  $n$  ( $\sigma = K\varepsilon^n$ ). The strain hardening exponent can be determined by using the true stress-true strain curve obtained from a tensile test. The Equation below describes the true stress-true strain correlation during the tensile testing:

$$\sigma = K\varepsilon^n \quad (4)$$

Where  $\sigma$  is true stress,  $K$  is the strength coefficient,  $\varepsilon$  is true strain, and  $n$  is strain hardening exponent. A simple power-curve relation can express the flow curve of many metals in the region of uniform plastic deformation, which is from yielding up to the maximum load. The strain-hardening exponent is the slope of the true stress-true strain curve, when plotted on logarithmic coordinates ( $n = \partial \ln \sigma / \partial \ln \varepsilon$ ). A high strain hardening exponent enhances a materials ability to uniformly distribute the imposed plastic strain.

Table 7 summarizes the effects of aging treatment on room temperature tensile properties for LP-DED NASA HR-1. The 1070W – 0.6” diameter round bar samples have an average yield strength, ultimate tensile strength, and fracture elongation of 87.02 – 109.60 ksi, 162.40 – 171.61 ksi, and 32.23 – 38.97%. The 350W – 0.047” thick samples have an average yield strength, ultimate tensile strength, and fracture elongation in the range of 73.57 – 89.58 ksi, 142.37 – 147.61 ksi, and 25.32 – 30.97%. The 0.047” thick single-pass samples, which have very large grain size, display excellent strain hardening exponent that are critical for LRE nozzle application. It is encouraging to note that NASA HR-1 is suitable for fabricating very thin panels using the LP-DED method. One 1070W – 0.6” diameter round bar sample that has the highest tensile strength was selected from each aging treatment to compare the strain hardening behavior. Signs of high strain hardening capability are delayed necking, high elongation, and lower yield strength. As shown in Figure 24, it is apparent that A4 2-step aging treatment, 1275 °F/16h + 1150 °F/16h (total time of 32 hours), yields higher strain hardening capability than the others.

Table 7. Effects of aging treatment on tensile properties for LP-DED NASA HR-1.

Laser Power & Sample Configuration	Aging Treatment	Aging Treatment	Yield Stress (ksi)	Tensile Stress (ksi)	Fracture Elongation (%)	Strain Hardening Exponent (n)
350 W – 0.248" W × 0.047" T	1325 °F/16h	A 1	89.98	147.52	25.32	0.210
	1300 °F/16h	A 2	78.48	143.62	26.91	0.250
	1275 °F/16h + 1200 °F/16h	A 3	83.54	147.61	27.89	0.237
	1275 °F/16h + 1150 °F/16h	A 4	73.57	142.37	30.97	0.274
<hr/>						
1070 W – Round Bar (0.6" Diameter)	1325 °F/16h	A 1	109.60	171.61	32.23	0.198
	1300 °F/16h	A 2	88.44	162.74	37.87	0.263
	1275 °F/16h + 1200 °F/16h	A 3	92.95	166.19	36.74	0.251
	1275 °F/16h + 1150 °F/16h	A 4	87.02	162.40	38.97	0.271
<hr/>						
1070 W – 0.248" W × 0.140" T	1325 °F/16h	A 1	104.54	155.29	21.78	0.175
	1300 °F/16h	A 2	96.48	156.21	26.67	0.216
	1275 °F/16h + 1200 °F/16h	A 3	100.14	157.09	27.50	0.197
	1275 °F/16h + 1150 °F/16h	A 4	92.42	158.33	29.66	0.223
<hr/>						
2600 W – 0.247" W × 0.25" T	1325 °F/16h	A 1	106.56	166.37	31.93	0.182
	1300 °F/16h	A 2	106.82	164.11	31.52	0.192
	1275 °F/16h + 1200 °F/16	A 3	107.42	170.17	31.61	0.189
	1275 °F/16h + 1150 °F/16	A 4	102.23	168.56	31.89	0.190

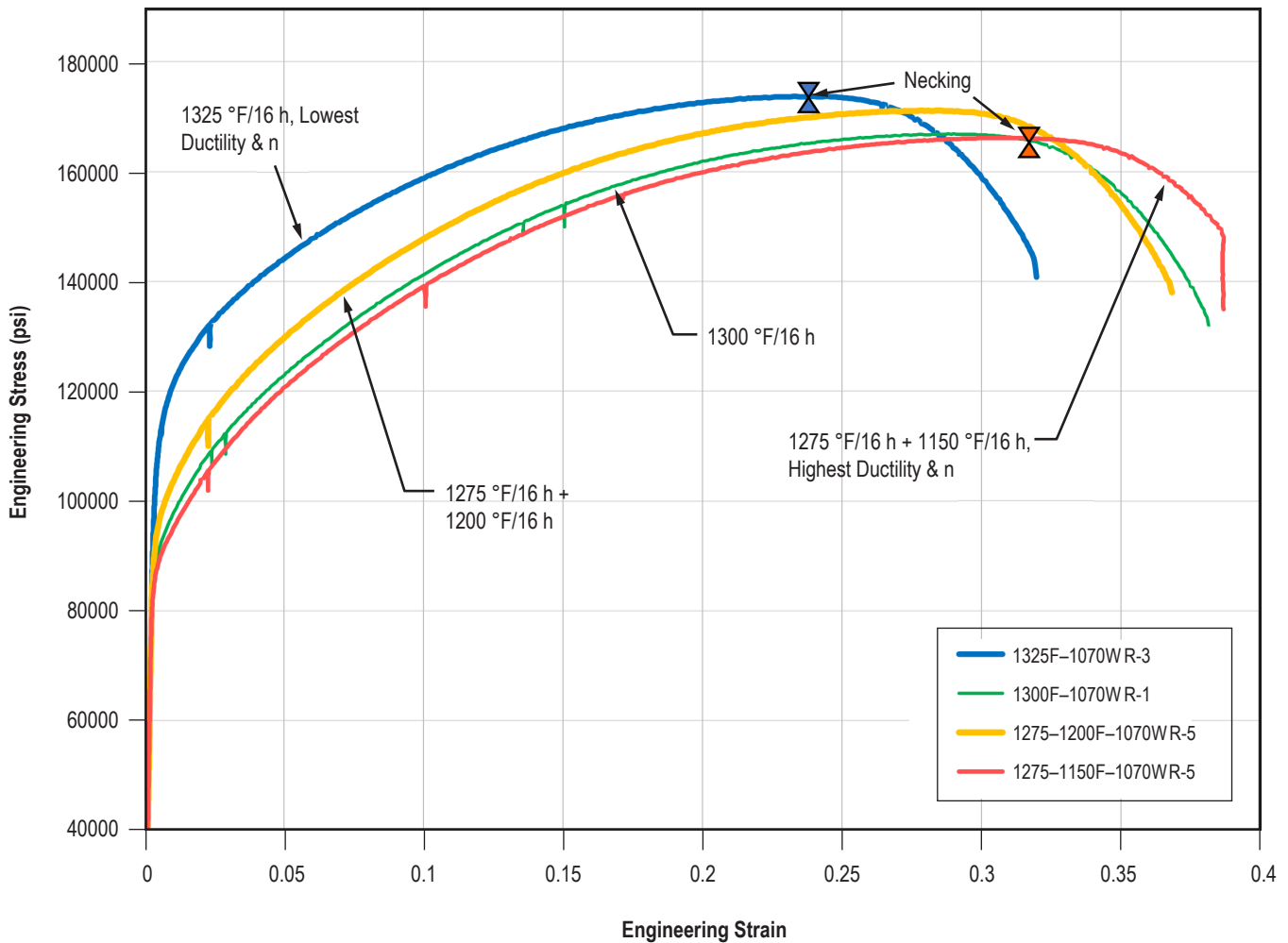


Figure 24. Overlaid stress-strain curves for the round bar samples (1070 W-0.6" diameter) that have the highest tensile strength from each aging treatment group.

One key takeaway from the tensile data analysis is A4 2-step aging treatment yields significantly higher tensile ductility and strain hardening exponent than the standard single-step aging treatment (1325 °F/16h). The strain hardening exponent ranking is A4 > A2 > A3 > A1. The material that has high strain hardening exponent can store more strain energy, diffuse deformation, and improve LCF performance. Strain hardening behavior is microstructure dependent and the improved strain hardening capability with A4 2-step aging can be attributed to high solute contents and the presence of finer and underaged  $\gamma'$  precipitate. The solute contents in the alloy can enhance the efficiency of dislocation storage during plastic deformation and increase the level of strain hardening. As nucleation and growth of  $\gamma'$  precipitate consumes more free solutes, an opposite evolution trend of strain hardening ( $n$ ) is observed. Therefore, A4 (1275 °F/16h + 1150 °F/16h) is the most promising and has been selected as the new aging treatment for LP-DED NASA HR-1. The evolution of post-processing heat treatment for LP-DED NASA HR-1 from the early stage heat treatment to the new heat treatment is given in Figure 25.

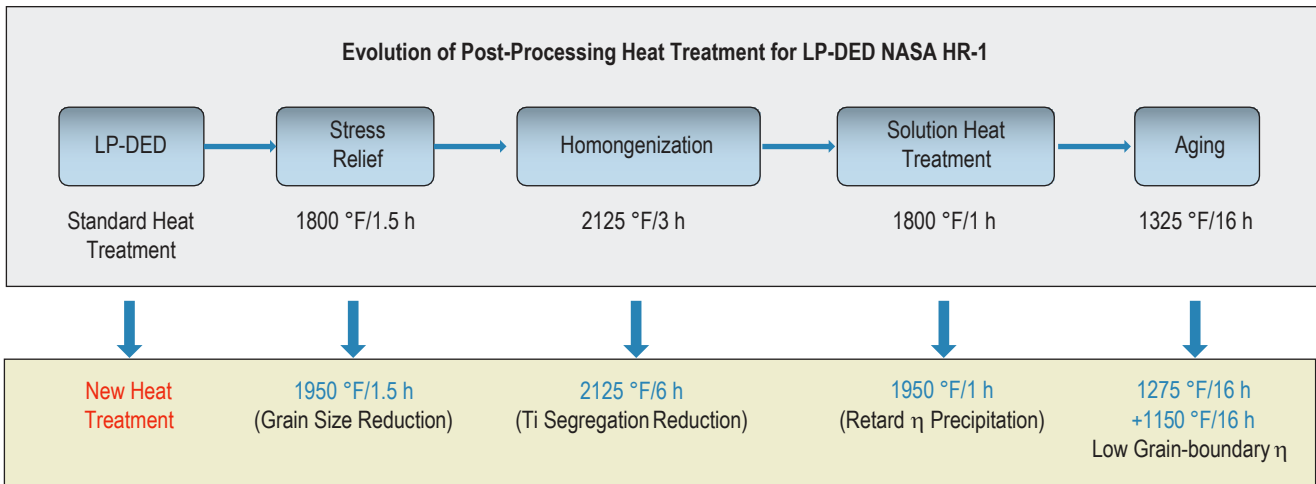


Figure 25. The evolution of post-processing heat treatment for LP-DED NASA HR-1.

In summary, LP-DED NASA HR-1 exhibits expected trends in tensile strength and ductility as temperatures of aging cycles are reduced. Changes from the standard single step aging cycle to a lower temperature two step aging cycle resulted in improved fracture elongation and strain hardening behavior, which is important for components that need excellent low cycle fatigue resistance. LP-DED NASA HR-1 exhibits lower yield and ultimate tensile strengths than the wrought alloy. This strength reduction is part of the trade to optimizing the alloy for LRE applications. However, ductility of LP-DED NASA HR-1 is significantly higher than that of the wrought alloy due to optimization of chemical composition and heat treatment. LCF performance, which is the primary service life limit factor for LRE nozzles, is expected to increase to the same level of the wrought alloy.

### 3.4 Key Materials Properties

#### 3.4.1 Temperature-Dependent Tensile Properties in Ambient Air.

Figure 26 shows the typical microstructure evolution of LP-DED NASA HR-1 multi-pass samples before and after heat treatment. Layer melt pool boundaries with different columnar dendritic morphologies can be clearly seen in the as-built state. The microstructure consists of recrystallized grains and annealed twins after heat treatment as shown in Figure 26(d). The typical grain size varies from approximately 50 – 250 µm. Grain boundaries look very clean as the undesirable grain-boundary  $\eta$  phase is reduced to a very low level with the new heat treatment.

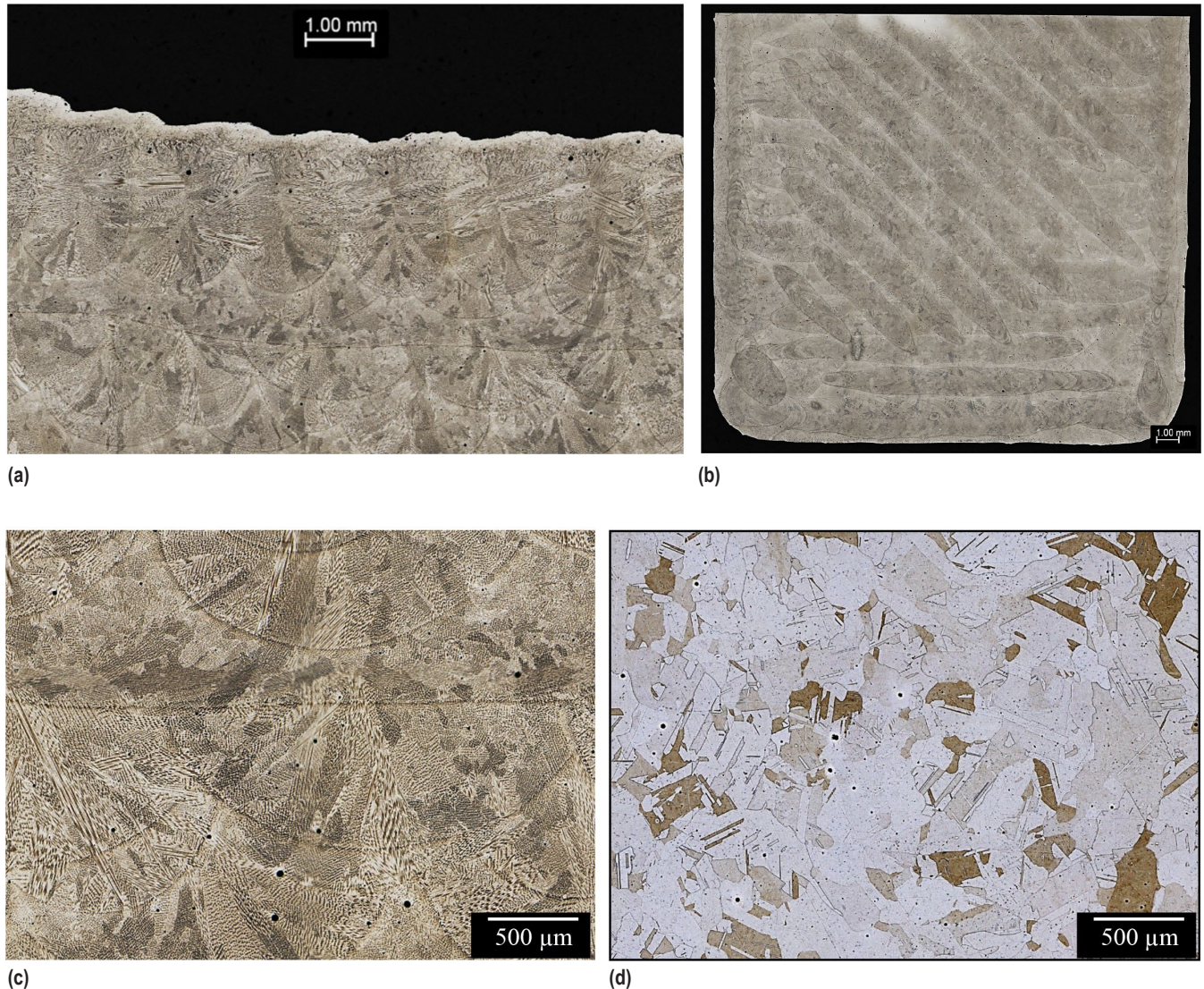


Figure 26. Cross-section of as-built LP-DED NASA HR-1 in (a) x-z plane showing melt pool morphologies, (b) x-y plane showing scanning strategy. Close-up view showing microstructure features in x-z plane in (c) as-built condition and (d) fully heat treated condition.

Temperature-dependent tensile properties of LP-DED NASA HR-1 were investigated using samples in two different aged conditions, 1325 °F/16h (1-step aging treatment) and 1275 °F/16h + 1150 °F/16h (2-step aging treatment). LP-DED NASA HR-1 round bar was machined into a cylindrical shaped tensile specimen along the build direction with a gauge length of 1 inch and 0.25 inch in diameter. Table 8 summarizes the tensile properties of LP-DED NASA HR-1 as a function of testing temperature from -320 °F to 1400 °F. It can be seen from Table 8 that both YS and UTS decrease gradually with an increase in the test temperature from room temperature to 1200 °F. UTS/YS ratio, and strain hardening exponent also decrease gradually as the test temperature increases up to 1200 °F. Tensile fracture elongation is very high around 45 – 49% at

$-320^{\circ}\text{F}$  and decreases slightly to 35 – 41% at room temperature. Tensile ductility remains quite high up to  $1100^{\circ}\text{F}$ . A significant reduction in ductility was noted when the testing temperature increased to  $1200^{\circ}\text{F}$  and above. LP-DED NASA HR-1 is normally recommended for component applications up to  $1200^{\circ}\text{F}$ .

Table 8. Summary of tensile properties for LP-DED NASA HR-1 1 as a function of testing temperature.

Laser Power & Sample Configuration	Aging Treatment	Tensile Test Temperature ( $^{\circ}\text{F}$ )	Yield Stress (ksi)	Tensile Stress (ksi)	Fracture Elongation (%)	UTS/YS Ratio	Strain Hardening Exponent (n)
1070 W – Round Bar (0.6" Diameter)	1-step	-320	106.70	205.37	44.67	1.92	0.291
	2-step		92.97	202.57	48.62	2.18	0.334
	1-step	RT	89.09	162.15	34.78	1.82	0.224
	2-step		77.28	153.91	41.36	1.99	0.283
	1-step	400	85.58	148.02	31.20	1.73	0.232
	2-step		77.84	143.32	35.60	1.84	0.254
	1-step	800	83.70	135.54	33.00	1.62	0.218
	2-step		76.10	130.36	36.60	1.71	0.234
	1-step	1000	82.58	131.12	31.40	1.59	0.210
	2-step		75.12	123.68	36.20	1.65	0.220
	1-step	1100	82.90	130.64	28.00	1.59	0.211
	2-step		73.22	120.22	33.20	1.65	0.226
	1-step	1200	85.95	123.65	22.83	1.44	0.168
	2-step		72.30	109.51	27.42	1.51	0.187
	1-step	1300	80.02	89.72	7.60	1.12	0.096
	2-step		69.84	80.50	10.20	1.15	0.111
	1-step	1400	69.38	73.96	7.40	1.07	0.080
	2-step		63.24	71.52	9.80	1.13	0.111

1-step aging treatment:  $1325^{\circ}\text{F}/16\text{h}$

2-step aging treatment:  $1275^{\circ}\text{F}/16\text{h} + 1150^{\circ}\text{F}/16\text{h}$  (32h total)

Strain hardening exponent (calculated from the true stress-strain curve) and UTS/YS ratio can be used to estimate both static and cyclic hardening capability.<sup>45</sup> LP-DED NASA HR-1 has the highest ductility at  $-320^{\circ}\text{F}$  because its strain hardening capability is higher at cryogenic temperatures than at room temperature and elevated temperatures. The materials with FCC crystal lattice, such as NASA HR-1, are very suitable for cryogenic applications as they have more dislocation slip systems (12 systems) that can assist in plastic deformation and enhance ductility in extremely cold condition. Many FCC alloys exhibit higher strain hardening capability at

cryogenic temperature because the internal energy of atoms is greatly reduced, which hampers the movement of dislocations. Tensile fracture elongation is typically proportional to the value of strain hardening exponent ( $n$ ) as high strain hardening capability can homogenize plastic deformation and retard tensile fracture initiation. Therefore, the improved ductility in cryogenic temperatures can be attributed to the enhanced strain hardening capability that makes deformation more homogeneous and stable prior to fracture.

The specimens aged with single-step aging cycle have higher strength but lower fracture elongation and strain hardening exponent. On the other hand, the specimens that were subjected to two-step aging treatment exhibits lower strength but higher fracture elongation and strain hardening exponent. Strain hardening exponent for LP-DED NASA HR-1 can vary due to the change in the solid solution concentration of  $\gamma$ -matrix and the size and distribution of  $\gamma'$  strengthening precipitate. The concentration of Ti and Al in the  $\gamma$ -matrix solid solution in 2-step aged condition is higher than that in the 1-step aged condition because the material is significantly underaged after 2-step aging cycle. The increase in strain hardening exponent can be attributed to higher solute concentration (Ti and Al) in  $\gamma$  matrix and the presence of finer tertiary  $\gamma'$  and more uniformly distributed secondary  $\gamma'$  precipitate structure. Higher Ti and Al concentration in  $\gamma$ -matrix enables the material to store more dislocations during tensile deformation and lead to enhanced strain hardening capability.

The engineering stress vs. strain curves of LP-DED NASA HR-1 tested at  $-320^{\circ}\text{F}$ , room temperature and  $1200^{\circ}\text{F}$  were selected to compare strain hardening behavior as a function of temperature. As shown in Figure 27, it is apparent that the flow stress and strain hardening behavior are strongly influenced by test temperature and aging cycles. Serrated stress-strain flow behavior was observed for the 2-step aged samples tested at  $1200^{\circ}\text{F}$ , which is indicative of dynamic strain aging (DSA). The repeated locking and unlocking of dislocations create serrations in stress-strain curves, which is known as DSA.<sup>46</sup> DSA is commonly seen in many Ni-based superalloys during tensile deformation at elevated temperatures.<sup>47</sup> DSA generally occurs at a certain combination of temperature and strain rate, where the diffusivity of the solute atom is sufficient to obstruct the dislocation motion. Serrations appear as a result of interaction of moving dislocations with the interstitial or substitutional alloying elements. It is interesting to note that the 1-step aged sample does not appear to have serrated stress-strain flow behavior as shown in Figure 27(c). The 2-step aged sample has more pronounced serrated stress-strain flow behavior that likely results from the presence of higher concentration of Ti and Al atoms in the  $\gamma$ -matrix solid solution (due to a high degree of under-aging) that enhances dislocation pinning.

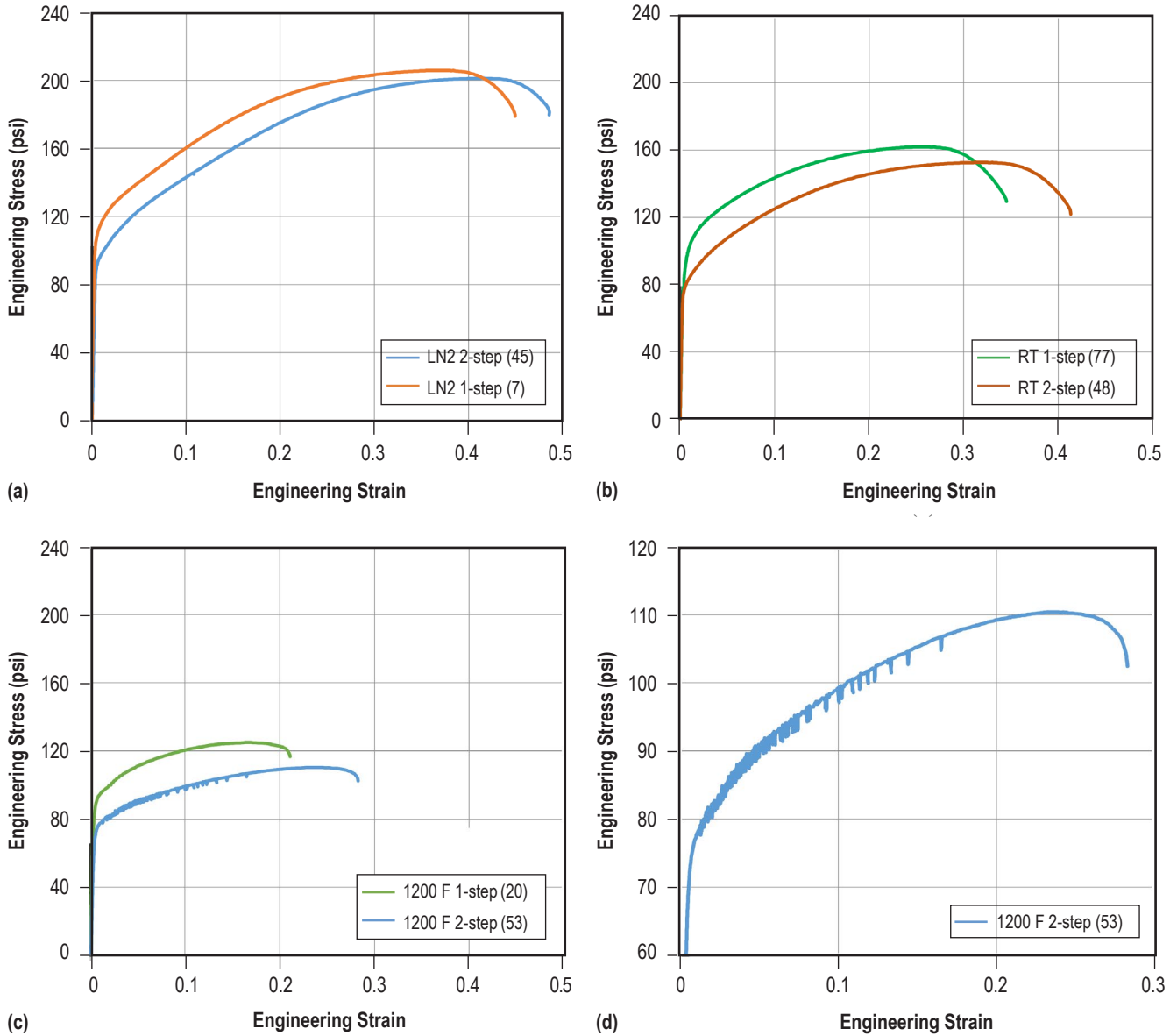


Figure 27. Engineering stress-strain curves of LP-DED NASA HR-1 tensile tested at (a)  $-320^{\circ}\text{F}$ , (b) ambient air, and (c)  $1200^{\circ}\text{F}$ . (d) Serrated stress-strain flow behavior is observed in the 2-step aged sample during tensile testing at  $1200^{\circ}\text{F}$ . Scales are kept in identical ranges from (a) through (c) to illustrate the variation in engineering stress and strain curves as a function of temperature.

Optical microscopy was performed to observe deformation-induced microstructure evolution near the fracture surface. Metallographic samples were prepared by sectioning through the gage section along the tensile loading direction. The typical cross-sectional images of the fractured tensile samples tested at three different temperatures are shown in Figure 28. The samples were heat treated using 2-step aging cycle. All samples exhibit deformed microstructure with numerous slip lines. The degree of plastic deformation is significantly higher at  $-320^{\circ}\text{F}$  and

RT than at 1200 °F as evidenced by more pronounced grain elongation and finer slip lines at lower temperatures. As shown in Figure 28, grains that are more elongated and have higher slip line density can be observed in –320 °F samples. Ductility improvement at cryogenic temperature results from more homogeneous plastic deformation as slip lines are finer and denser at –320 °F than at room temperature (see Fig. 28).

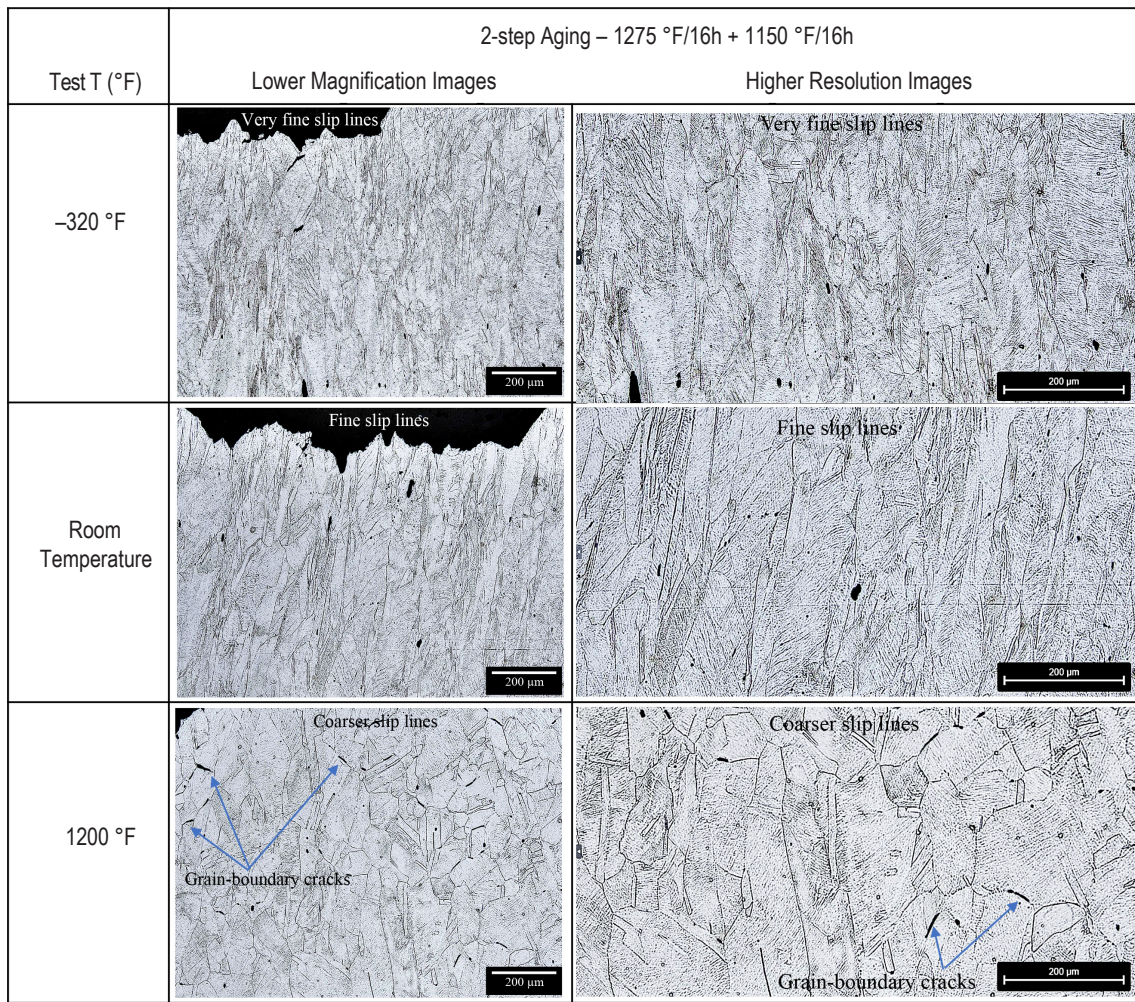


Figure 28. Cross-sectional views of the fractured tensile samples after testing at three different temperatures, –320 °F, ambient air, and 1200 °F. The samples were heat treated using 2-step aging cycle.

**34.1.1 Deformation and Fracture Behavior at Elevated Temperatures.** Crystal lattice expands at elevated temperatures, and the movement of dislocations becomes easier. The degree of grain elongation is considerably lower and slip lines become more widely spaced after tensile testing at elevated temperatures. Figure 29 presents the fracture surface morphologies of LP-DED NASA HR-1 specimens tensile tested at 1200 °F. The fracture surface displays predominantly ductile transgranular fracture mode. However, small partial intergranular fracture zones are

present near the gauge surface. The presence of isolated partial intergranular fracture zones contributes to the reduction in ductility from 35–45% at room temperature to 25–30% at 1200 °F. Grain boundaries provide additional strengthening effects to metallic materials at lower temperature but can become the weakest link when the temperature exceeds 0.5 T<sub>m</sub> (melting temperature), which is approximately 1250 °F for LP-DED NASA HR-1.<sup>46</sup> Plastic deformation often occurs by mixed dislocation slip and grain sliding when grain boundaries become weaker than grain interior at elevated temperatures. The presence of intergranular fracture indicates grain boundary sliding became more prominent when tensile testing at 1200 °F, causing some cracks to develop along grain boundaries as shown in Figure 29.

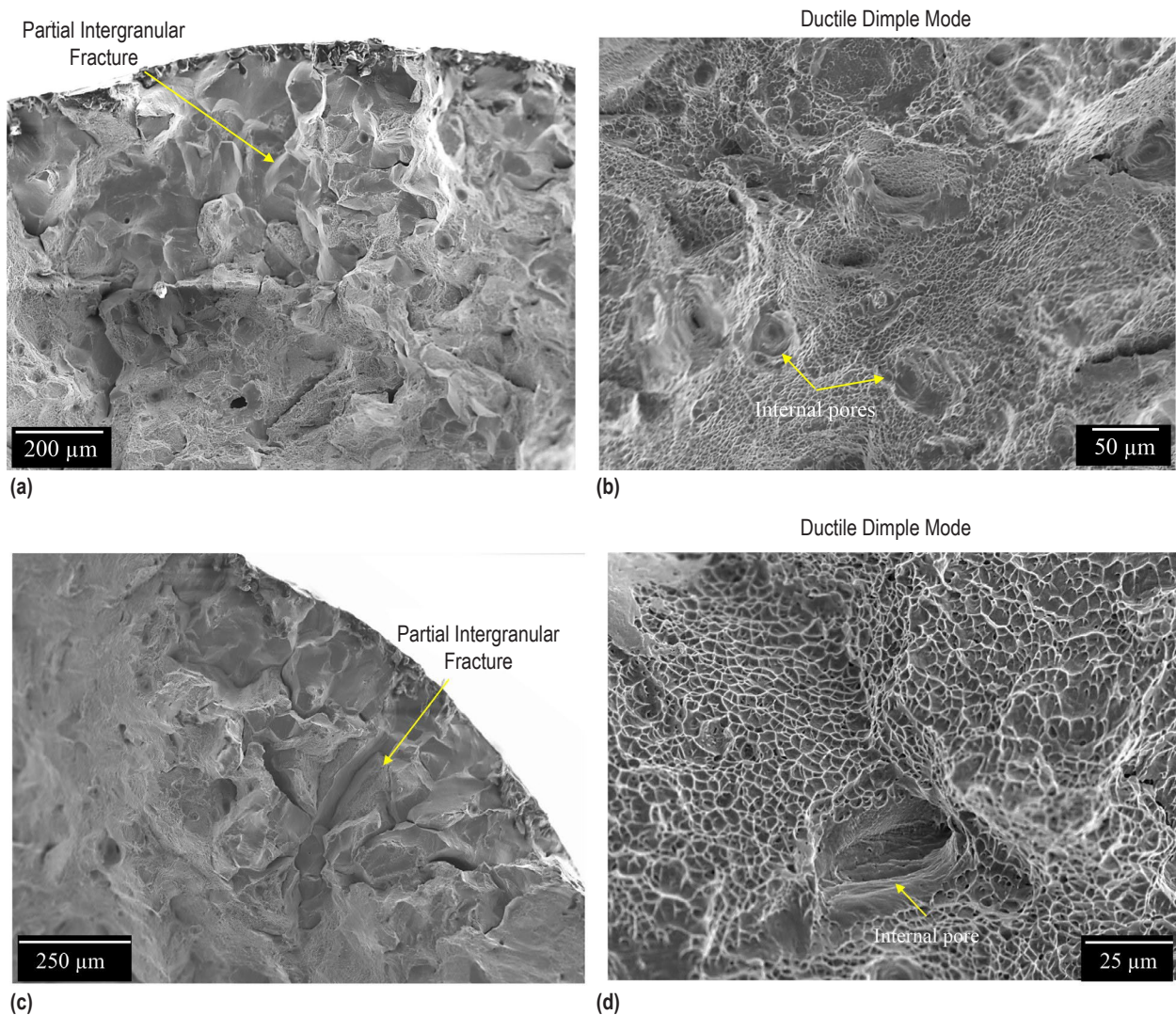


Figure 29. Fracture surfaces of LP-DED NASA HR-1 tensile tested at 1200 °F. The samples were in (a) and (b) 1-step aged condition and (c) and (d) 2-step aged condition. The near gauge surface areas have some isolated intergranular fracture zones, while ductile dimple fracture predominates away from the specimen gauge surface.

**3412 LP-DED and Wrought NASA HR-1 Comparison.** A comparison of tensile properties between LP-DED NASA HR-1 and the wrought alloy is given in Figure 30. Wrought NASA HR-1 clearly has higher strength than LP-DED alloy under the same test temperatures. Although strength decreases with increasing temperature, both yield and tensile strengths remain quite high up to 1200 °F for wrought NASA HR-1. Ti is the primary strengthening element as it combines with Ni to form the primary strengthening  $\gamma'$  precipitate in NASA HR-1. The volume fraction of  $\gamma'$  precipitate is expected to be significantly reduced in LP-DED NASA HR-1 as the Ti content is reduced from 2.8% (in the wrought alloy) to 2.5% (in the LP-DED alloy). The strength reduction is part of the trade when using LP-DED process to manufacture NASA HR-1 and is thus expected based on the chemistry reformulation. However, LP-DED NASA HR-1 has significantly higher ductility than the wrought alloy. The change from the standard single step aging cycle to a lower temperature two step aging cycle resulted in further improvement in ductility. Compared with the wrought alloy, the ductility increases from 29% to 48.6% at -320 °F, from 23% to 41.36% at room temperature, and from 18% to 27.4% at 1200 °F when the LP-DED alloy is processed with 2-step aging cycle. The exceptional ductility that LP-DED NASA HR-1 displays can be attributed to the optimal balance of primary material properties through alloy chemistry and heat treatment optimization.

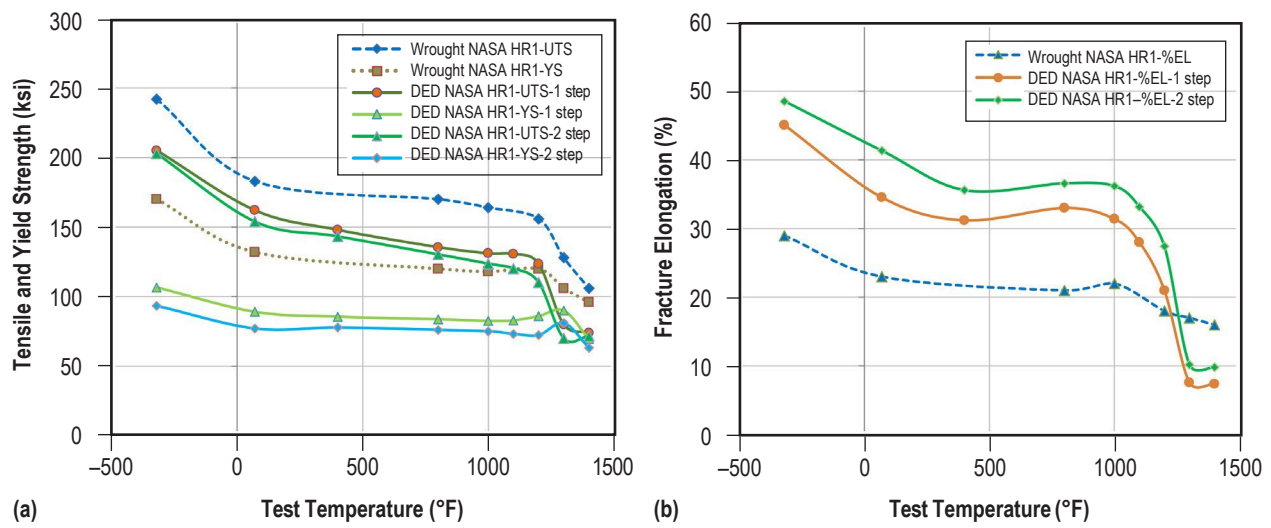


Figure 30. Comparison of (a) tensile and yield strengths and (b) fracture elongation for LP-DED and wrought NASA HR-1 as a function of testing temperature.

### 342 LCF Properties in Ambient Air.

Tension-compression type of low cycle fatigue (LCF) tests were performed in air at room temperature at strain ratio ( $R$ ) of -1 and total strain of 1% and 2%. The LCF samples were heat treated with two different aging cycles. Table 9 presents the LCF test results that include inelastic strain range at the mid-life cycle ( $N_h$ ), the cycle to crack initiation ( $N_i$ ), and cycle to failure ( $N_f$ ). The change in the aging treatment from 1-step to 2-step has little effects on inelastic strain range. At 1% total strain, the inelastic strain range varies from 0.34 – 0.35% in the 1-step aged condition

and from 0.32 – 0.36% in the 2-step aged condition. When the total strain is increased to 2%, the inelastic strain varies from 1.17 – 1.21% in the 1-step aged condition and from 1.19 – 1.23% in the 2-step aged condition. However, the change in aging treatment from 1-step to 2-step has significant effects on LCF life. At 1% total strain, the LCF life is approximately 30 – 50% longer when the specimens were in 2-step aged condition. The 2-step aged samples also exhibit longer fatigue crack initiation life than those heat treated with 1-step aging cycle. This is consistent with the tensile test results that 2-step aging results in higher ductility and strain hardening exponent than 1-step aging, which is essential for LCF critical components such as LRE nozzles. However, the effect of aging treatment on LCF life appears to be less significant when the total strain is increased to 2%. At 2% total strain, the average LCF life increases moderately by 15–20% when the specimens were in 2-step aged condition. The tendency to delay crack initiation also increases slightly by 10 – 15% for the 2-step aged material at 2% total strain.

Table 9. Room temperature LCF tests results for LP-DED NASA HR-1. LCF was conducted at ambient air at total strain range of 1% and 2%, and  $R = -1$ .

Material	Environment	Strain Range	Aging Treatment	Specimen ID	Inelastic Strain Range at $N_h$ (%)	Cycles to Crack Initiation ( $N_i$ )	Cycles to Failure ( $N_f$ )
LP-DED NASA HR-1	Ambient Air	-0.5% to 0.5%	1325 °F	34	0.35	7545	8318
				104	0.34	4794	6600
				105	0.35	4601	5054
		1275 °F + 1150 °F	1275 °F + 1150 °F	4	0.32	9279	11765
				5	0.36	6957	7581
				68	0.36	8551	10492
		-1% to 1%	1325 °F	121	1.21	813	899
				122	1.19	764	828
				123	1.17	860	898
		1275 °F + 1150 °F	1275 °F + 1150 °F	21	1.19	897	981
				22	1.22	827	880
				23	1.23	1121	1298

**3421 Hysteresis Loops.** To better understand the LCF behavior of LP-DED NASA HR-1, cyclic stress-strain curves were analyzed using hysteresis loops. The specimens were heat treated to two different aging conditions. The typical hysteresis loops of the first cycle, the peak stress cycle, and the cycle that is near half-life for total strain of 1.0% and 2.0% are illustrated in Figure 31 and 32. The hysteresis loops of most materials typically vary more significantly in the initial cycles and stabilize around the half-life cycle. The area within a hysteresis loop is energy dissipated during a cycle, which is usually in the form of heating from the plastic deformation. Nearly symmetrical hysteresis loops can be observed under both aging conditions and strain

amplitudes. The shape of hysteresis loops varied slightly with the level of total strain. Higher total strain resulted in larger plastic strain range and wider hysteresis loops. For each aging condition, there is significant cyclic strain hardening in the first 10 – 30 cycles. The peak tensile/compression stresses decreased slightly near the half cycle due to cyclic stabilization after the initial cyclic hardening.

One noticeable difference on the hysteresis loops is the degree of cyclic hardening between the samples processed with different aging cycles. As shown in Figure 31, the samples that were heat treated with 2-step aging cycle show more pronounced cyclic hardening response than those heat treated with 1-step aging cycle. At 1% total strain, the peak tensile stress increased slightly (by 2.6 ksi) from 90.5 ksi at the 1<sup>st</sup> cycle to 93.1 ksi at the half life cycle for the 1-step aged sample. In comparison, the peak tensile stress increased (by 7.2 ksi) from 77.7 ksi at the 1<sup>st</sup> cycle to 84.9 ksi at the half life cycle for the 2-step aged sample. At 2% total strain, the peak tensile stress increased modestly (by 9.7 ksi) from 100.3 ksi in the 1<sup>st</sup> cycle to 110.0 ksi at the half life cycle for the 1-step aged sample are shown in Figure 32. In comparison, the peak tensile stress increased more significantly (by 16.6 ksi) from 84.9 ksi in the 1<sup>st</sup> cycle to 101.5ksi at the half life cycle for the 2-step aged sample. The hysteresis loops clearly show that the 2-step aged sample has higher cyclic strain hardening capability than the 1-step aged sample. This is consistent with the strain hardening behavior of tensile tested samples that strain hardening capability for LP-DEN NASA HR-1 can be enhanced with 2-step aging treatment.

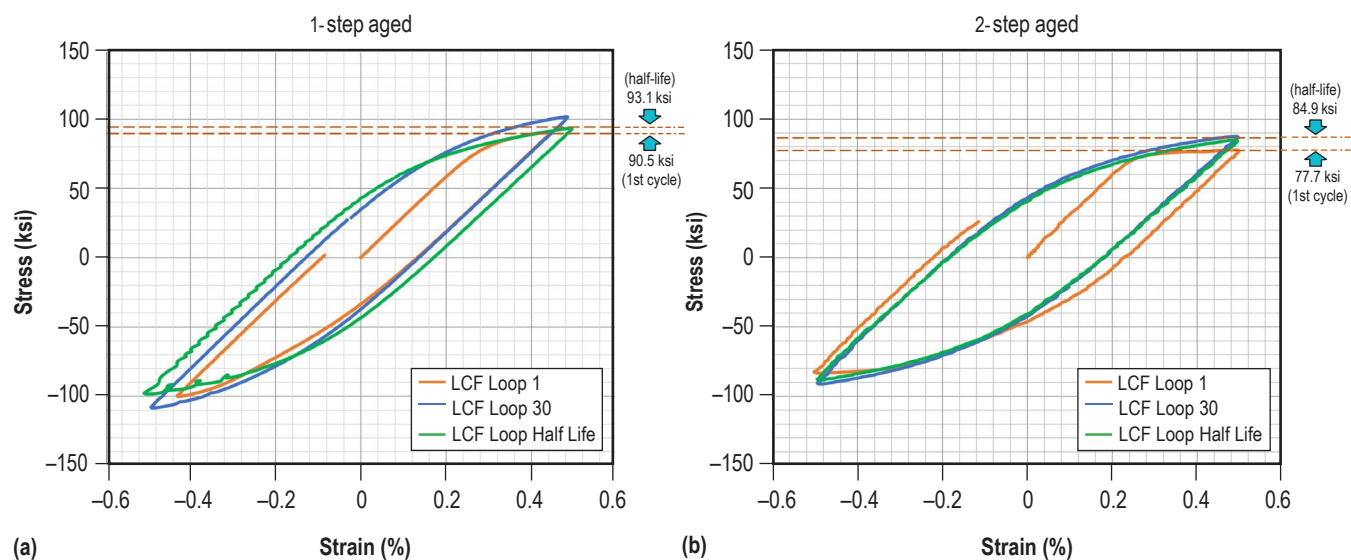


Figure 31. The typical hysteresis loops of the first cycle, the near peak stress cycle (cycle 30), and the cycle that is near half-life at 1.0% total strain in (a) 1-step aged condition and (b) 2-step aged condition.

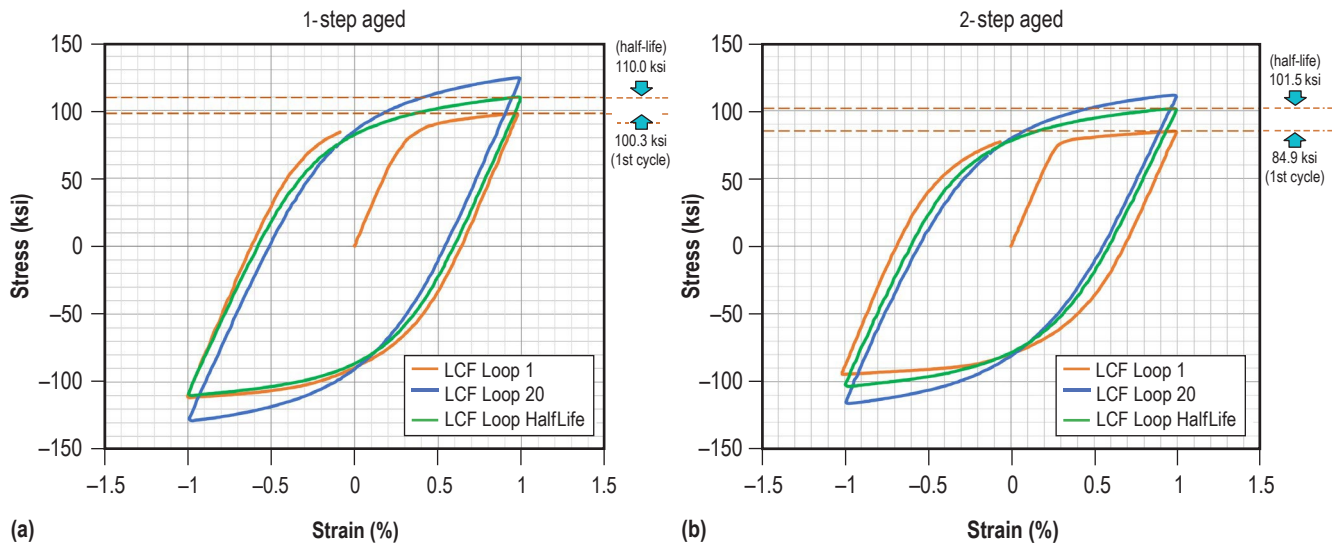


Figure 32. The typical hysteresis loops of the first cycle, the near peak stress cycle (cycle 20), and the cycle that is near half-life at 2.0% total strain in (a) 1-step aged condition and (b) 2-step aged condition.

**3422 Cyclic Stress Response.** The evolution of peak tensile stress ( $\sigma_{\max}$ ) and compressive stress ( $\sigma_{\min}$ ) with respect to the number of cycles ( $N$ ) at two different total strains is shown in Figure 33. The variation of tensile and compressive stress magnitude with number of cycle ( $N$ ) is dependent on the applied total strain and the condition of aging. Both 1-step and 2-step aged samples display significant cyclic strain hardening in the first 10 – 30 cycles. The initial cyclic hardening was brief and the peak stress curve became noticeably flattened as cyclic hardening response leveled off. The peak stresses of 1-step aged samples were always higher than that of 2-step aged samples before crack initiation. However, the 2-step aged samples exhibit more pronounced cyclic hardening than 1-step aged samples.

Both crack initiation life and fatigue life can be determined from the peak tensile stress vs. cycle ( $N$ ) plot. The LCF specimens maintain a cyclically stable condition for approximately 70 – 80% of the fatigue life until the onset of crack initiation ( $N_i$ ), after which accelerated cyclic softening occurred. Onset of LCF crack initiation can be determined when a rapid drop in the peak tensile stress occurred. It is evident that most of the LCF life is spent in crack initiation. The regime of rapid cyclic softening occurs at final stage of LCF testing, approximately within the final 10 – 15% of the fatigue life. The growth of fatigue crack accelerated at late stage of LCF testing and cyclic stress amplitude drops rapidly until final fracture. Final fracture of the LCF samples was gradual as there is no sign of a sudden drop in the peak tensile stress amplitude after crack initiation.

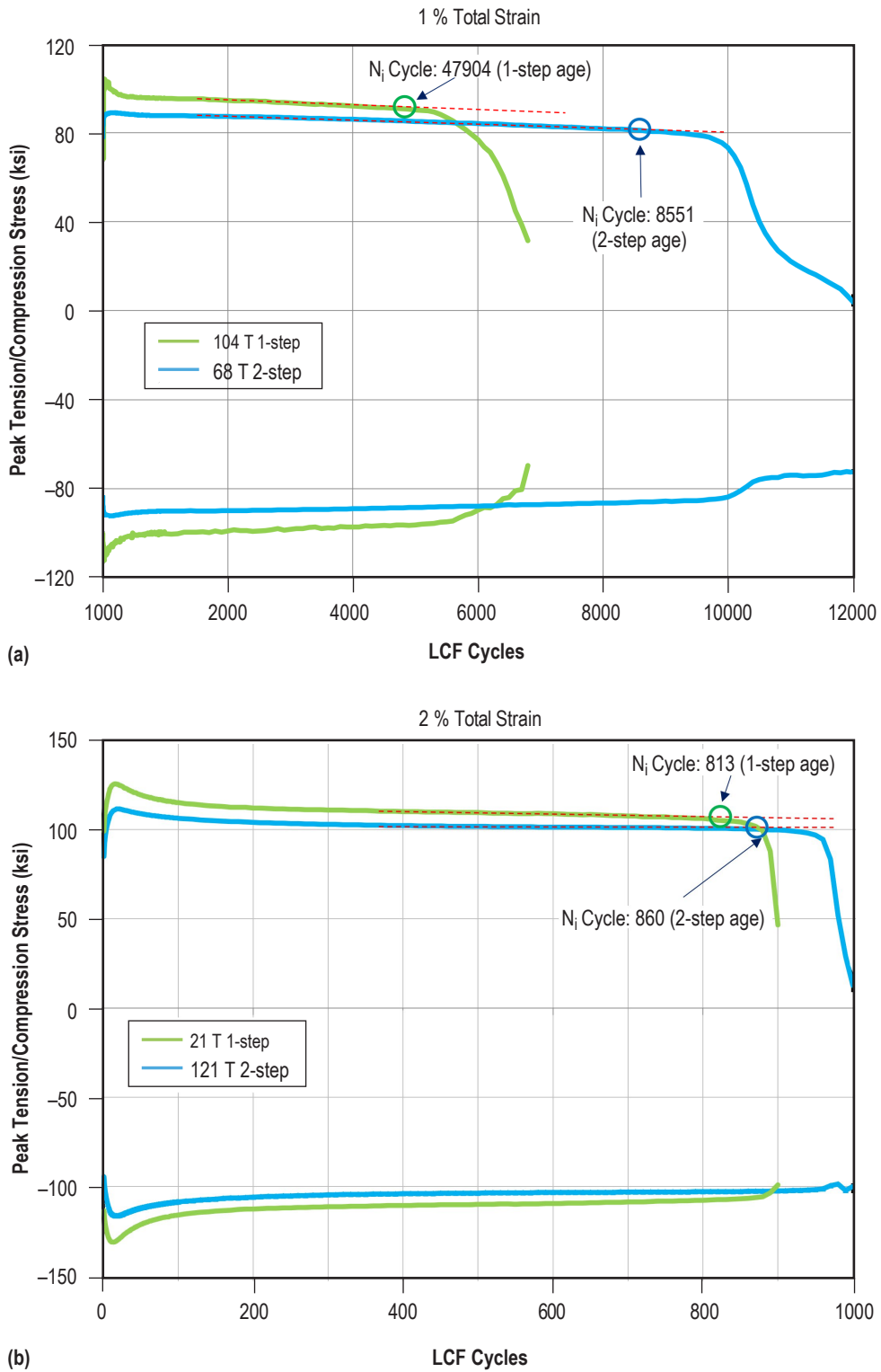


Figure 33. Variations of peak tensile stress ( $\sigma_{\max}$ ) and compressive stress ( $\sigma_{\min}$ ) with number of cycles ( $N$ ) at (a) 1% total strain (0.5% strain amplitude) and (b) 2% total strain (1.0% strain amplitude). The LCF samples were heat treated with two different aging cycles.

The division of the total fatigue life into different stages (crack initiation, crack propagation, and final fracture) is an important consideration in regard to fatigue assessment.<sup>48</sup> Many fatigue assessments focus on the stages when a fatigue crack grows to a detectable size. The LCF data indicates that two-step aging seems to be able to delay fatigue crack initiation, which is significant as engineering materials often contain inherent defects and the use of total life approaches can lead to overestimation of useful fatigue life. Some mechanical components are designed based on crack initiation life as the problem in its initial stage (after the sign of initial crack initiation) can be efficiently controlled by NDE inspection to determine the extent of crack advance.<sup>48</sup> In other words, it is safer to take preventive rather than corrective maintenance action to prevent unexpected catastrophic failure. Overall, 2-step aging is better suited for LCF critical applications than one-step aging as it leads to longer LCF life by making the material more ductile, enhancing strain hardening capability and delaying crack initiation.

**3423 Cyclic Hardening Analysis.** In order to quantitatively compare the effects of strain amplitude and aging treatment on the cyclic stress response, the ratios of cyclic hardening and cyclic softening were calculated. Cyclic hardening ratio (HR) and cyclic softening ratio (SR) can be expressed as follows:

$$HR = (\otimes\sigma_{max} - \otimes\sigma_{first}) / \otimes\sigma_{first} \quad (5)$$

$$SR = (\otimes\sigma_{max} - \otimes\sigma_{half}) / \otimes\sigma_{max} \quad (6)$$

Where  $\Delta\sigma_{max}$ ,  $\Delta\sigma_{first}$ , and  $\Delta\sigma_{half}$  represent the stress amplitudes at the maximum, first cycle and half cycle, respectively.<sup>45,50</sup> Table 10 shows the comparison of the stress amplitudes at the maximum ( $\Delta\sigma_{max}$ ), first cycle ( $\Delta\sigma_{first}$ ) and half-life ( $\Delta\sigma_{half}$ ) cycles for LP-DED NASA HR-1 in both 1-step and 2-step aged conditions. As can be seen in Table 10, the 2-step aged specimens exhibited higher HR and lower SR than the 1-step aged specimens at both 1% and 2% total strain. The hardening ratio (HR) and softening ratio (SR) as a function of the total strain are shown in Figure 34. Both HR and SR values increase with increasing strain amplitude. The samples in 2-step aged condition exhibit higher HR but lower SR than those in 1-step aged condition. As a result, the 2-step aged samples exhibit larger differences between the values of HR and SR than the 1-step aged samples at both total stain amplitudes. HR and SR are two important parameters in characterizing cyclic deformation behavior. Higher HR and lower SR indicate enhanced cyclic hardening that enables the cyclic plastic deformation to become more homogeneous. These observations further confirm that 2-step aging is better suited for LCF critical applications than 1-step aging.

Table 10. Comparison of the stress amplitudes at the maximum ( $\Delta\sigma_{\max}$ ), first cycle ( $\Delta\sigma_{\text{first}}$ ) and half-life ( $\Delta\sigma_{\text{half}}$ ) cycles for LP-DED NASA HR-1 tested at 1% and 2% total strain in both 1-step and 2-step aged conditions. HR and SR values are also given in this Table 10.

Material	Environment	Strain Range	Aging Treatment	Specimen ID	$\Delta\sigma_{\max}$ (ksi)	$\Delta\sigma_{\text{half}}$ (ksi)	$\Delta\sigma_{\text{first}}$ (ksi)	HR	SR
LP-DED NASA HR-1	Ambient	-0.5% to 0.5%	1325 °F	34	100.0	91.0	91.2	0.096	0.090
				104	101.6	93.4	90.5	0.123	0.081
				105	97.8	90.3	91.8	0.065	0.077
		-1% to 1%	1275 °F + 1150 °F	4	88.6	84.7	78.8	0.124	0.044
				5	89.8	86.5	77.0	0.166	0.037
				68	88.8	84.9	77.7	0.143	0.044
		-1% to 1%	1325 °F	121	125.2	109.4	99.1	0.263	0.126
				122	126.5	110.3	98.5	0.284	0.128
				123	124.1	110.0	97.9	0.268	0.114
		-1% to 1%	1275 °F + 1150 °F	21	111.5	101.6	84.7	0.316	0.088
				22	114.5	103.2	85.7	0.336	0.098
				23	109.9	99.9	84.1	0.306	0.091

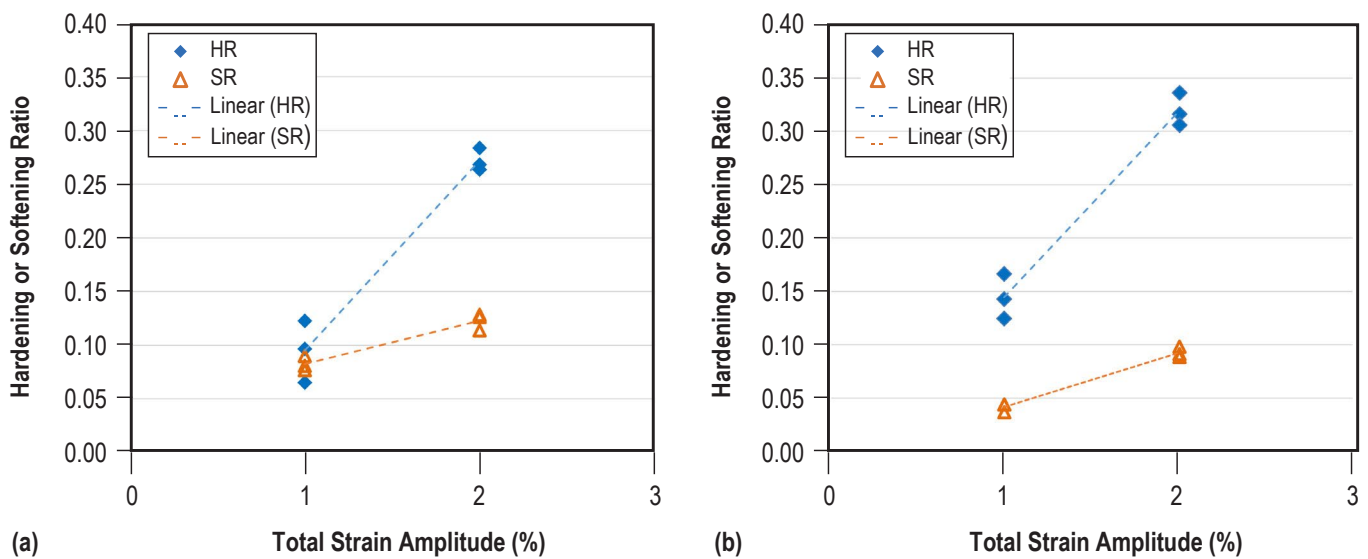


Figure 34. Variations of the cyclic hardening ratio (HR) and softening ratio (SR) as a function of total strain for LP-DED NASA HR-1 in (a) 1-step aged and (b) 2-step aged conditions.

**3424 Fracture Features.** Fatigue life of a component can be divided to five stages: dislocation movement, crack nucleation, micro-crack propagation, macro-crack propagation, and the final fracture.<sup>48</sup> The first three stages are treated as the crack initiation phase followed by a macro-crack propagation phase and final fracture. Figure 35 and 36 provides details regarding LCF fracture behavior of LP-DEN NASA HR-1, such as crack initiation and crack propagation, under 1% and 2% total strain amplitudes. The LCF specimens were heat treated with two different aging cycles. There are three distinct zones on the fracture surface consisting of fatigue crack initiation, crack propagation, and final fast-fracture regions (as indicated by dashed white and yellow lines). There are multiple crack initiation sites in each specimen. It can be seen from Figure 35 that the fatigue crack initiated from the specimen surface at 1% total strain in both 1-step and 2-step aged specimens. As shown in Figure 35(c), the crack initiation site has distinct slip bands along certain crystallographic planes and directions. Slip bands are a result of the systematic buildup of fine dislocation slip movements.

There are multiple crack initiation sites in the crack initiation region at 2% total strain and the small cracks grew along several different directions in the early stage of crack propagation. The cracks grew, coalesced, and propagated further until the final fracture. Striation marks are very distinct in the fatigue propagation zone as shown in Figure 35(d). The striation spacing during the early stage of crack propagation ranges from 0.5 – 1  $\mu\text{m}$  at 1% total strain. At 2% total strain (see Fig. 36), the fatigue crack also initiated along certain crystallographic planes near the specimen surface. Some fatigue propagation striations can be clearly seen, although a significant portion of the fracture surface was smeared due to repeated tensile-compression loadings. At 2% total strain, the striation spacing is approximately 2 – 10  $\mu\text{m}$  during the early stage of crack propagation. The width of a striation increases significantly when the total strain increases from 1% to 2% as the increase in stress intensity leads to higher fatigue crack growth rate.

Fatigue striation mark is the typical characteristic of crack propagation in a very ductile material.<sup>45</sup> Striations on the fatigue fracture surface show the incremental growth of a fatigue crack. Each striation represents fatigue crack growth per cycle and the width of a striation is indicative of the overall crack growth rate. There is no sign that the fatigue cracks initiated from the near surface defects, such as internal pores. The small fatigue cracks grew and coalesced and advanced further in a direction normal to the applied stress, forming a large propagation zone. The final fracture area is significantly larger when the total strain was increased from 1% to 2%. The most noticeable differences between the two aging cycles (1-step vs., 2-step aging) were in the crack propagation zone. The crack propagation zone appears to be larger in 2-step aged specimen, which correlates well with its higher cyclic hardening capability and longer LCF life.

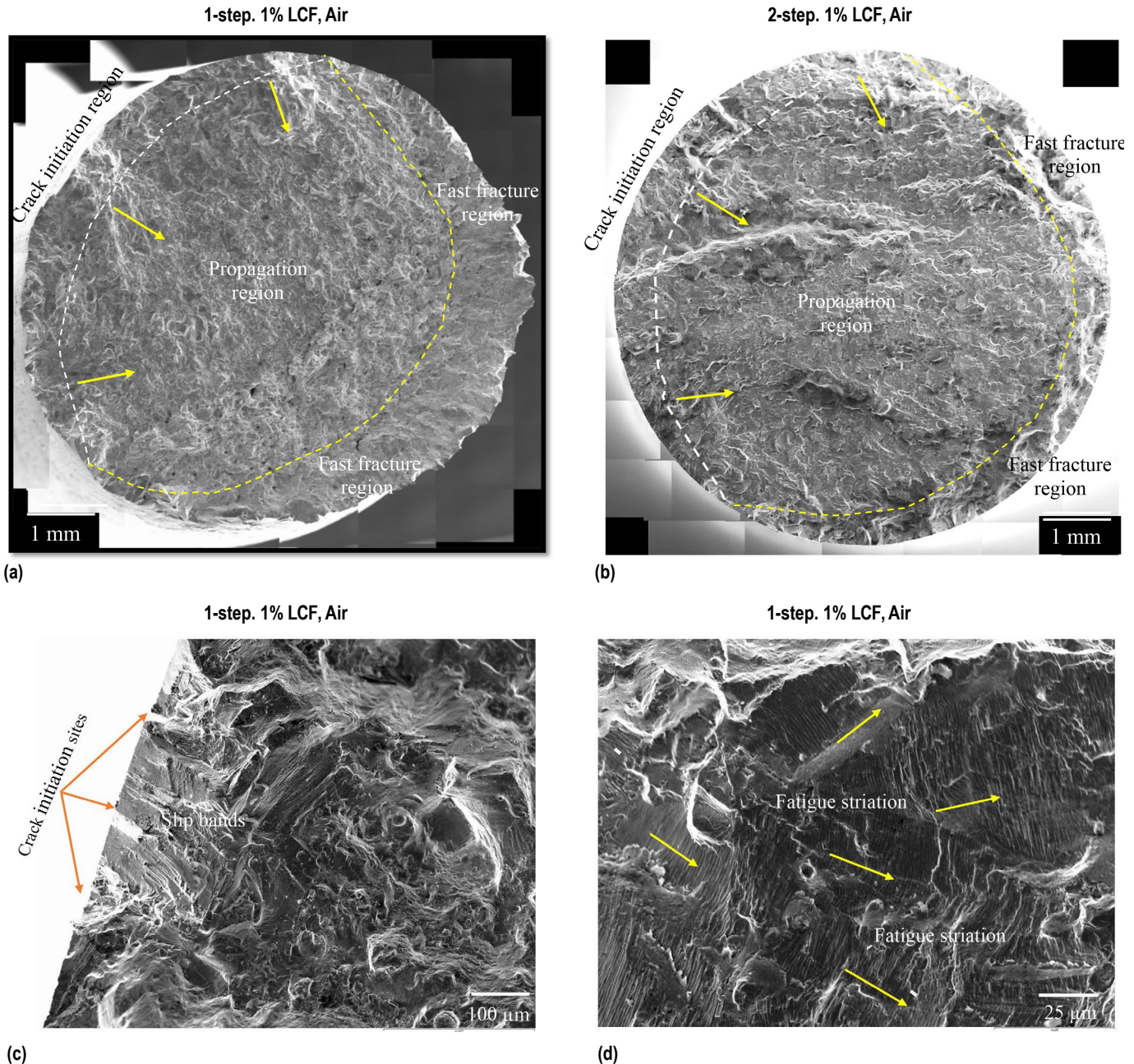
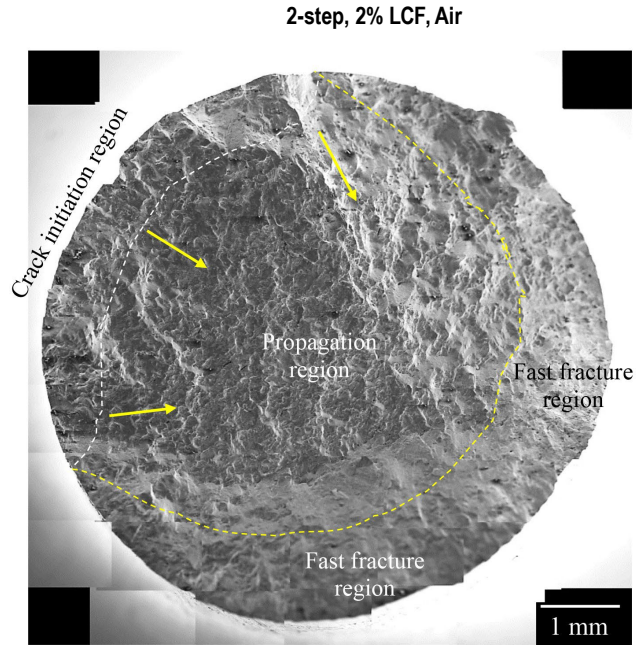
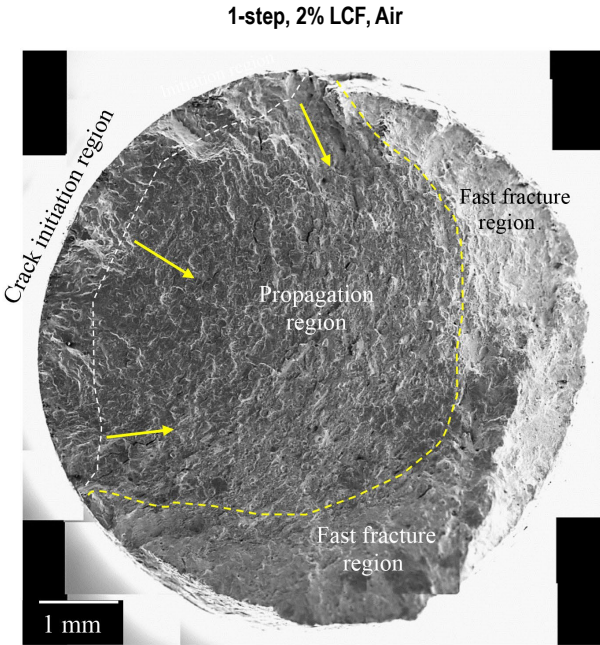
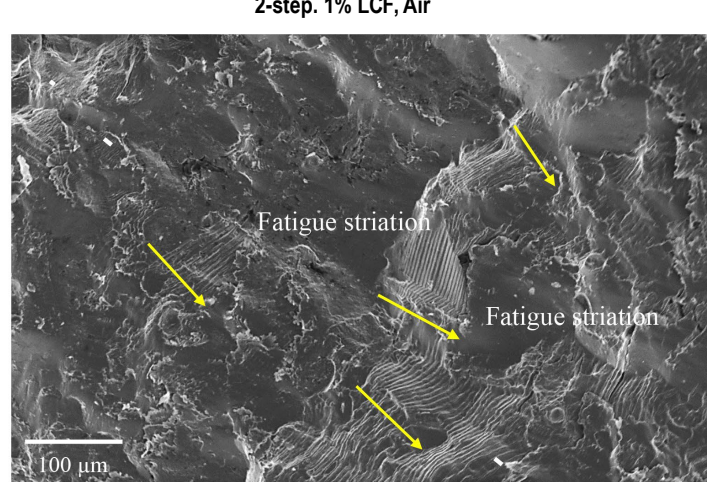
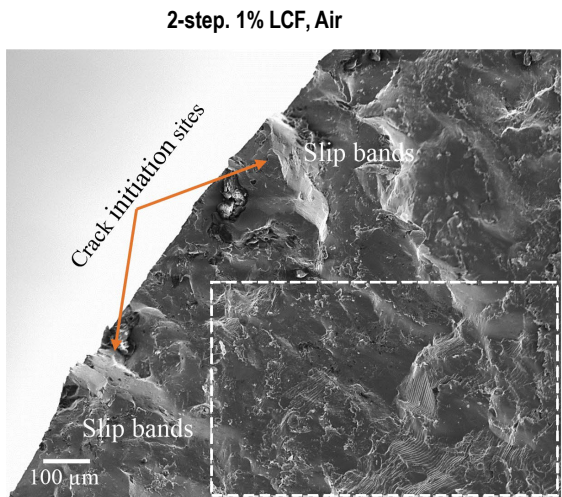


Figure 35. LCF fracture surface of LP-DED NASA HR-1 tested at 1% total strain in (a) 1-step and (b) 2-step aged conditions. (c) Crack initiation from the surface and (d) distinct fatigue striation marks showing early stage of crack propagation in the 1-step aged specimen.



(a)

(b)



(c)

(d)

Figure 36. LCF fracture surface of LP-DED NASA HR-1 tested at 2% total strain in (a) 1-step and (b) 2-step aged conditions. (c) Crack initiation from the surface and (d) distinct fatigue striation marks showing early stage of crack propagation in the 2-step aged specimen (close up view of the white dotted box in (c)).

**3425 LP-DED and Wrought NASA HR-1 Comparison.** Comparison of LCF life between LP-DED and wrought NASA HR-1 was made to evaluate the effects of the LP-DED process on LCF behavior. The LP-DED LCF specimens were heat treated with two different aging cycles (1-step and 2-step aging), while the wrought specimens were heat treated with the standard 1-step aging at 1325 °F/16h. As shown in Figure 37, the LCF strain-life curves look similar between wrought and LP-DED NASA HR-1. At 1% total strain, the LCF life of 1-step and 2-step aged LP-DED samples varies from 5054–8318 cycles and 7581–11765 cycles, respectively. LCF life of LP-DED NASA HR-1 in 2-step aged condition is slightly shorter than that of wrought NASA HR-1, which lasted for approximately 12500 cycles at 1% total strain. At 2% total strain, the LCF life of 1-step and 2-step aged LP-DED samples varies from 828–898 cycles and 880–1298 cycles, respectively. LCF life of LP-DED NASA HR-1 in 2-step aged conditions is comparable to that of wrought NASA HR-1, which lasted for 1020 cycles at 2% total strain. With optimized chemical composition and heat treatment, the LCF life of LP-DED NASA HR-1 was increased to a level that is comparable to the wrought alloy. LP-DED is a viable process method to manufacture NASA HR-1 for LRE nozzles that operate under a severe reverse strain cycling condition at high strain amplitudes. The exceptional LCF performance of LP-DED NASA HR-1 can be attributed to its excellent ductility and strain hardening capability, which help homogenize plastic deformation and delay crack initiation.

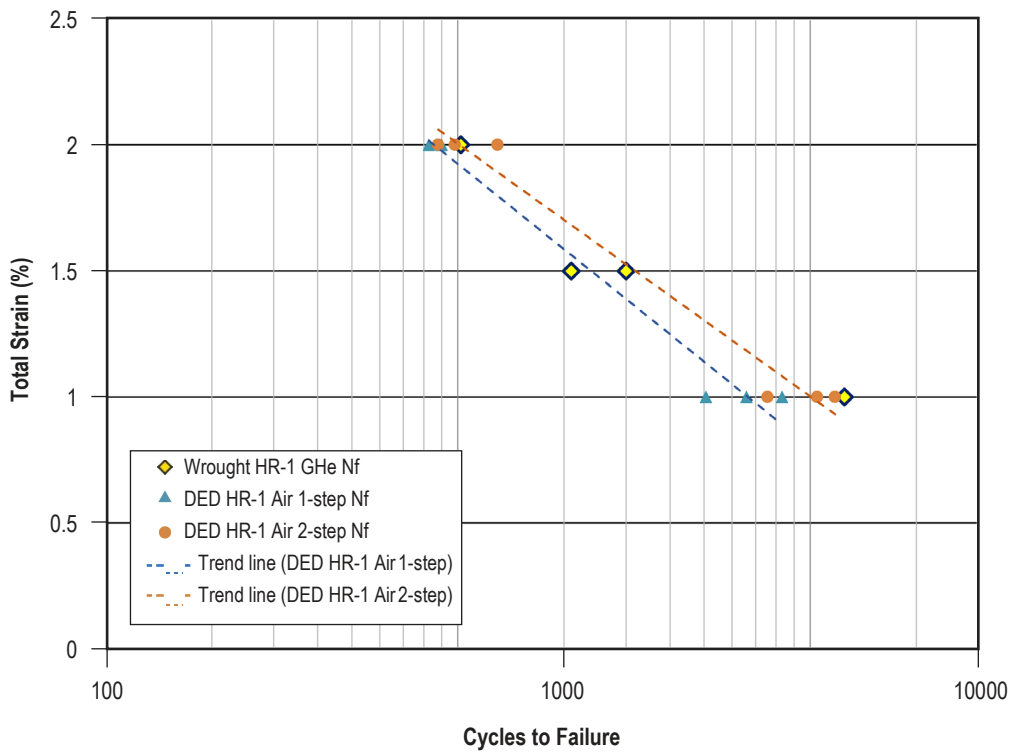


Figure 37. LCF life comparison by superimposing strain-life curves for LP-DED and wrought NASA HR-1. The LP-DED LCF specimens were heat treated with two different aging cycles (1-step and 2-step aging), while the wrought specimens were heat treated with the standard 1-step aging at 1325 °F/16h.

### 343 Tensile Properties in High Pressure Hydrogen Environment

As the initial material screening to evaluate the susceptibility of hydrogen environment embrittlement (HEE) for LP-DEN NASA HR-1, tensile testing was conducted in a 5 ksi high pressure gaseous hydrogen environment at ambient temperature. HEE is commonly known as the degradation of certain mechanical properties that occur while the material is exposed to a high pressure gaseous hydrogen environment under the influence of an applied stress.<sup>26</sup> HEE effects are a function of temperature and maximum HEE susceptibility usually occurs near room temperature. The tensile ductility degradation of smooth tensile specimens, tested in hydrogen as compared to that in helium, is commonly used to gauge HEE susceptibility.<sup>26</sup> Figure 38 shows the microstructure (in x-z plane) of the LP-DEN NASA HR-1 tensile samples prior to tensile testing in hydrogen. A high degree of recrystallization had taken place after heat treatment and the average grain size is ~75  $\mu\text{m}$ . Grain boundary looks very clean as the undesirable grain-boundary  $\eta$  phase is reduced to a very low level with the new heat treatment.



Figure 38. The typical microstructure (in x-z plane) of the LP-DEN NASA HR-1 samples used for tensile testing in 5 ksi gaseous hydrogen environment. The average grain size is approximately 75  $\mu\text{m}$ .

Tensile samples were heat treated using two different aging treatments, 1325 °F/16h (1-step aging) and 1275 °F/16h + 1150 °F/16h (2-step aging). Initial tensile testing was performed in 5 ksi gaseous helium environment at a strain rate of 0.05 in/in/min to provide a baseline comparison to the 5 ksi gaseous hydrogen. Strain rate was reduced to 0.0001 in/in/min when tensile testing in

5 ksi gaseous hydrogen environment to maximize the effects of HEE. Table 11 presents the tensile properties for LP-DED NASA HR-1 tested at room temperature in 5 ksi gaseous helium and hydrogen environments. The average tensile properties for wrought NASA HR-1 tested in high pressure helium and hydrogen environments are also given in Table 11. As expected, the 2-step aged material exhibits lower strength but higher tensile ductility than the 1-step aged material in both helium and hydrogen environments. Hydrogen does not seem to affect the strain hardening behavior for LP-DED NASA HR-1 as the strain hardening exponent in hydrogen is comparable to that in helium. Ductility, as represented by total fracture elongation, was reduced from 34.50% to 28.75% in 1-step aged condition, and from 41.73% – 33.1% in 2-step aged condition. Although there are some ductility reductions in hydrogen, it is significant to note that the tensile ductility of LP-DED NASA HR-1 remains quite high when testing in high pressure gaseous hydrogen environment for 7–10 hours under an extremely slow strain rate of 0.0001 in/in/min.

Table 11. The average tensile properties, strain hardening exponent and testing duration for the tensile tests performed in high pressure helium and hydrogen environments.

Material	Aging Treatment	Strain Rate (in/in/min)	Test Environment	Yield Stress (ksi)	Ultimate Tensile Stress (ksi)	Ductility (%EL)	Strain Hardening Exponent (n)	Testing Duration (minute)
LP-DED NASA HR-1	1-step	0.05	5 ksi GHe	102.08	170.17	34.50	0.234	6 – 7
	1-step	0.0001	5 ksi GH <sub>2</sub>	98.82	161.81	28.75	0.237	450 – 550
LP-DED NASA HR-1	2-step	0.05	5 ksi GHe	86.99	162.26	41.73	0.279	7 – 8
	2-step	0.0001	5 ksi GH <sub>2</sub>	87.55	151.35	33.10	0.278	550 – 650
Wrought NASA HR-1	1-step	0.05	5 ksi GHe	136.93	183.07	23.57	–	4 – 5
	1-step	0.005	5 ksi GH <sub>2</sub>	128.83	175.37	23.40	–	20 – 25

1-step aging treatment: 1325 °F/16h

2-step aging treatment: 1275 °F/16h + 1150 °F/16h

The ratios of yield stress (YS), ultimate tensile stress (UTS), and ductility (fracture elongation) for LP-DED and wrought NASA HR-1 tested in high pressure hydrogen (GH<sub>2</sub>) and helium (GHe) environments are given in Table 12. The YS ratios (GH<sub>2</sub>/GHe) for LP-DED NASA HR-1 in both 1-step and 2-step aged conditions were above 97%, indicating that hydrogen had little effect on the stress required to initiate plastic deformation. Tensile elongation ratio in hydrogen vs. in helium (GH<sub>2</sub>/GHe) was used to assess HEE susceptibility. The samples in 2-step aged condition exhibited a lower ductility ratio than that in 1-step aged condition, but the fracture elongation of the 2-step aged material is higher than the 1-step material by ~ 4.35% in hydrogen. Although LP-DED NASA HR-1 exhibits lower GH<sub>2</sub>/GHe ductility ratios than the wrought alloy, the tensile ductility of LP-DED NASA HR-1 in high pressure hydrogen environment is significantly higher than that of the conventional wrought alloy by 5 – 10%.

The variation in the GH<sub>2</sub>/GHe ductility ratio between LP-DED NASA HR-1 and the wrought alloy can be attributed to the discrepancy in the tensile testing strain rate. The tensile testing strain rate for LP-DED NASA HR-1 is 0.0001 in/in/min, which is approximately 20 – 30 times slower than that for the wrought alloy (0.005 in/in/min). The reduction in strain rate increases the exposure time in high pressure gaseous hydrogen environment from approximately 20–25 minutes (0.005 in/in/min) for the wrought alloy to roughly 450–650 minutes (0.0001 in/in/min) for the LP-DED alloy. Since dislocation motion and its interaction with hydrogen is highly strain rate sensitive, the HEE effects are expected to become more pronounced when tensile testing at a slower strain rate.<sup>51</sup> The use of tensile ductility ratio (as shown in Table 12) is intended for initial screening to gauge the effects of HEE and should not be used for component design. Additional mechanical testing in high pressure hydrogen environment is needed to evaluate the effects of hydrogen on other critical mechanical properties such as low cycle fatigue, high cycle fatigue, and fatigue crack growth, etc.

Table 12. The GH<sub>2</sub>/GHe ratios of yield stress (YS), ultimate tensile stress (UTS), and ductility (fracture elongation) for LP-DED and wrought NASA HR-1.

Material	Aging Treatment	Strain Rat (in/in/min)	YS Ratio (GH <sub>2</sub> /GHe)	UTS Ratio (GH <sub>2</sub> /GHe)	Ductility Ratio (GH <sub>2</sub> /GHe)
LP-DED NASA HR-1	1-step	0.0001	1.01	0.93	0.83
	2-step	0.0001	0.97	0.95	0.79
Wrought NASA HR-1	1-step	0.005	0.94	0.96	0.99

1-step aging treatment: 1325 °F/16h

2-step aging treatment: 1275 °F/16h + 1150 °F/16h

The typical engineering stress-strain curves for LP-DED NASA HR-1 tested in high pressure helium and hydrogen environments are presented in Figure 39. All specimens display continuous strain hardening before reaching the UTS. Distinct necking can be observed from the stress-strain curves and the development of tensile fracture was gradual as there is still 4–5 % ductility (fracture elongation) between the onset of necking and final fracture. Serrated stress-strain behavior was found for both 1-step and 2-step aged samples in hydrogen, indicative of Portevin-Le Chatelier (PLC) effect.<sup>52</sup> The PLC effect manifests itself as an unstable plastic flow during tensile testing under certain conditions of strain rate and temperature. It has been reported that hydrogen can trigger PLC effect in traditional wrought and AM 718 alloy at room temperature.<sup>52</sup> The serrated stress-strain flow behavior is caused by the dragging effect of hydrogen atoms on dislocations. Occurrence of a drag force requires two conditions: (1) formation of hydrogen atmospheres at the dislocations and (2) the hydrogen atmospheres move with but lag behind the dislocations. The drag force of hydrogen atoms is strain rate dependent. Lower strain rate increases the drag force because reduced strain rate permits more competitive motion between hydrogen atoms and dislocations to form hydrogen atmospheres around the dislocations. As a result, repeated locking and unlocking of dislocations by hydrogen creates serrations in the stress-strain curves.

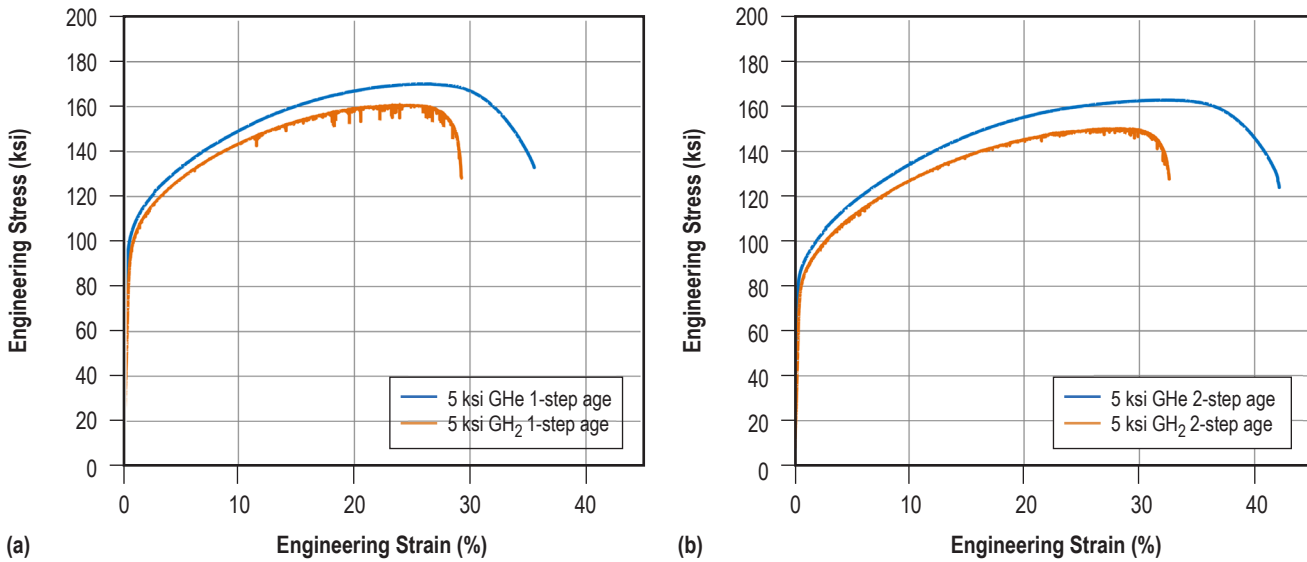


Figure 39. Engineering stress-strain curves of LP-DEN NASA HR-1 tensile tested in high pressure helium and hydrogen environment in (a) 1-step aged and (b) 2-step aged conditions. Serrated stress-strain flow behavior is observed for samples tested in high pressure hydrogen environment.

Plastic deformation occurs more uniformly in the initial stages of a tensile test as the diffusion distance of hydrogen is still very short. As tensile testing continues, the dislocation density continues to increase and more hydrogen atoms can be transported and accumulate in the regions with high plastic deformation. For LP-DEN NASA HR-1 in 1-step aged condition, the PLC effects become more pronounced when the plastic strain exceeds 12% as hydrogen is increasingly accumulated in the regions that have high dislocation density. The effects of HEE became more pronounced when the plastic instability occurs after the onset of necking. PLC results in localization of plastic deformation and the serrations become more intense in the post-necking region when local damage occurred.<sup>53</sup> The serrations on the stress-strain curves are more pronounced in the 1-step aged specimen than in the 2-step aged specimen, which may be caused by the difference in their strain hardening behavior. Compared with the 2-step aged samples, the samples in 1-step aged condition exhibit lower strain-hardening capability. As a result, deformation takes place by more heterogeneous dislocation slip that results in deformation localization and more pronounced PLC effects.<sup>54</sup>

**3.4.3.1 Hydrogen-induced surface cracking.** Surface characteristics of tensile tested specimens were analyzed using optical microscopy. As shown in Figure 40, the specimen surface exhibited unusual “orange peel” appearance after prolonged tensile testing in high pressure hydrogen environment. Many surface cracks are present and distributed along the machining marks. Per the ASTM G-142 standard, tensile specimen for evaluation of hydrogen effect should be machined to have a surface finish of 32  $\mu\text{in}$  or better to minimize the amount of cold work on the gauge surface. However, examination of specimen surface finish found the gage surface finish is approximately 75  $\mu\text{in}$ , which is significantly coarser than the 32  $\mu\text{in}$  specified by ASTM G-142.

Machining marks are stress concentration sites that are known to promote crack initiation and affect tensile ductility.<sup>55</sup> The gage section having a rougher surface finish could be one of the mechanisms that contribute to the reduced tensile fracture elongation in 5 ksi GH<sub>2</sub> environment for LP-DED NASA HR-1. Future tensile testing in high pressure gaseous hydrogen environment will use specimens that have surface roughness conforming to the ASTM G-142 standard to avoid localized grooves (such as machining marks) that promote surface cracking.

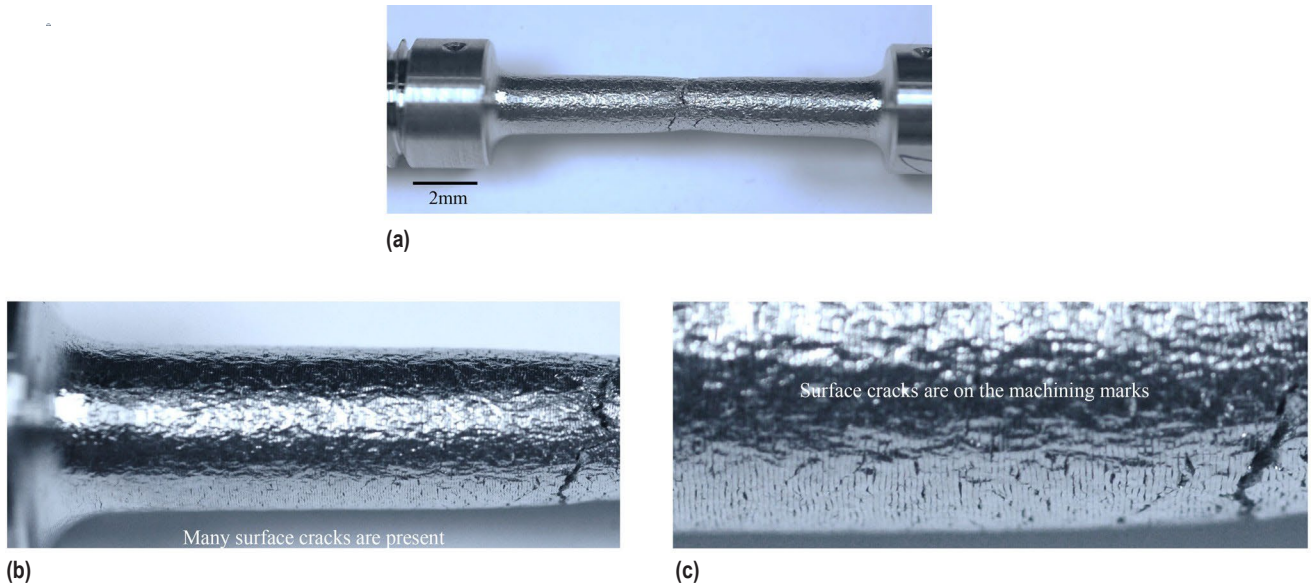
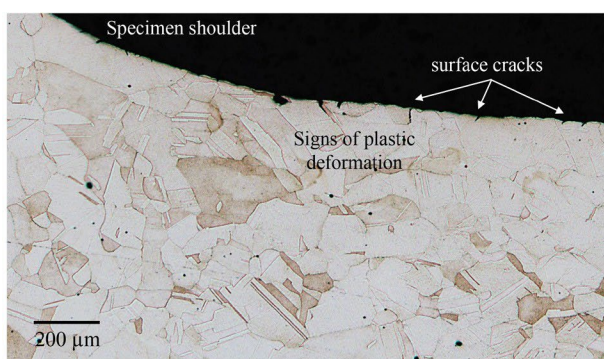


Figure 40. Macrographs of LP-DED NASA HR-1 tensile tested in hydrogen showing (a) orange peel appearance on the surface along the gauge length, (b) many surface cracks are present along the machining marks, (c) close-up view of the surface cracks. This specimen was in 2-step aged condition.

An in-depth analysis of the deformed microstructure was performed to see the effects of hydrogen. Cross-sectional views of a fractured tensile specimen, which is heat treated with 2-step aging cycle, are shown in Figure 41. The fracture surface is oriented at approximately 45° with respect to the tensile loading direction, which corresponds to the plane of near maximum shear stress. Figure 41(b) reveals signs of plastic deformation in the specimen shoulder region, which indicates the material is very ductile in hydrogen and plastic deformation extends outside the specimen gauge section. The depth of surface cracks and the surrounding microstructure is shown in Figure 41(b) and (c). Most surface cracks are 20 – 60 µm deep along the machining marks and oriented at approximately 30 – 45° with respect to the loading direction. This further demonstrates that LP-DED NASA HR-1 remains very ductile in 5 ksi gaseous hydrogen environment as the surface cracks initiated by ductile shear mode. Grain structure becomes more heavily deformed near the fracture surface. As shown in Figure 41(d) and (e), the fracture surface exhibits typical ductile transgranular type of fracture mode and there is no sign of brittle intergranular fracture.



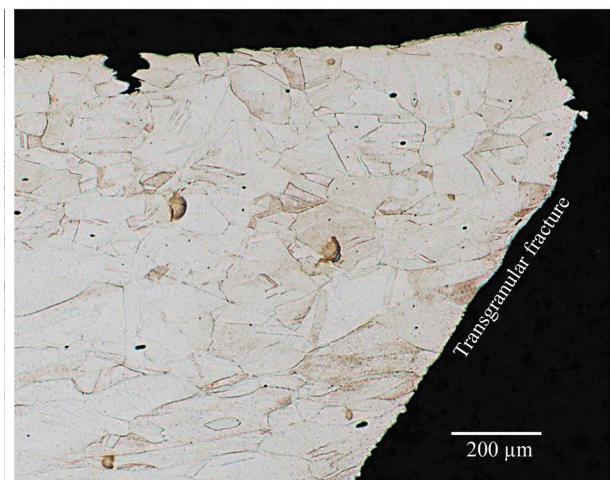
(a)



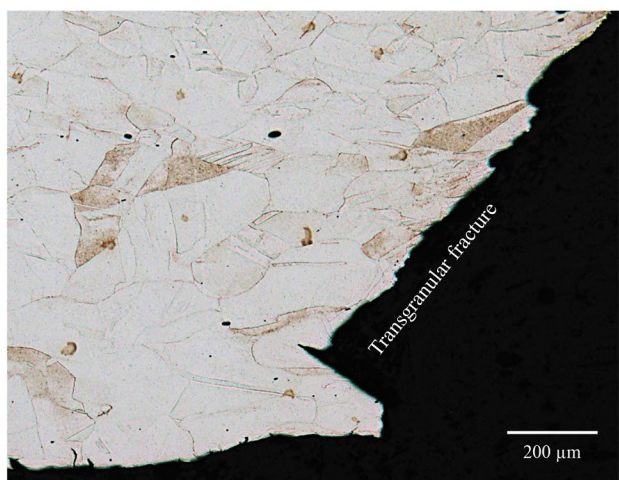
(b)



(c)



(d)



(e)

Figure 41. Optical images showing (a) cross-sectional view of a fractured tensile sample tested in 5 ksi gaseous hydrogen environment, (b) noticeable surface cracks and plastic deformation are present in the shoulder region (region A in (a)), (c) 20 – 60  $\mu\text{m}$  deep surface cracks are present along the machining marks (region B in (a)), (d) and (e) the fracture surface is oriented at approximately 45° with respect to the loading direction and the fracture mode is predominantly ductile transgranular (regions C and D in (a)). This tensile specimen was in 2-step aged condition.

Cross-sectional views of a fractured tensile specimen, which is heat treated with 1-step aging cycle, are shown in Figure 42. As is the case with the 2-step aged specimen, the 1-step aged specimen also displays similar deformation and fracture characteristics after tensile testing in hydrogen. Many surface cracks, 30–100  $\mu\text{m}$  deep, initiated from the machining marks and grew along the plane of maximum shear stress. Many fine slip lines can be clearly seen that indicates the material remained very ductile under the influence of high-pressure gaseous hydrogen. As shown in Figure 42 (b) and (c), the final fracture surface exhibits the typical characteristics of shear-dominated ductile transgranular mode, and there is no sign of a brittle intergranular type of fracture.

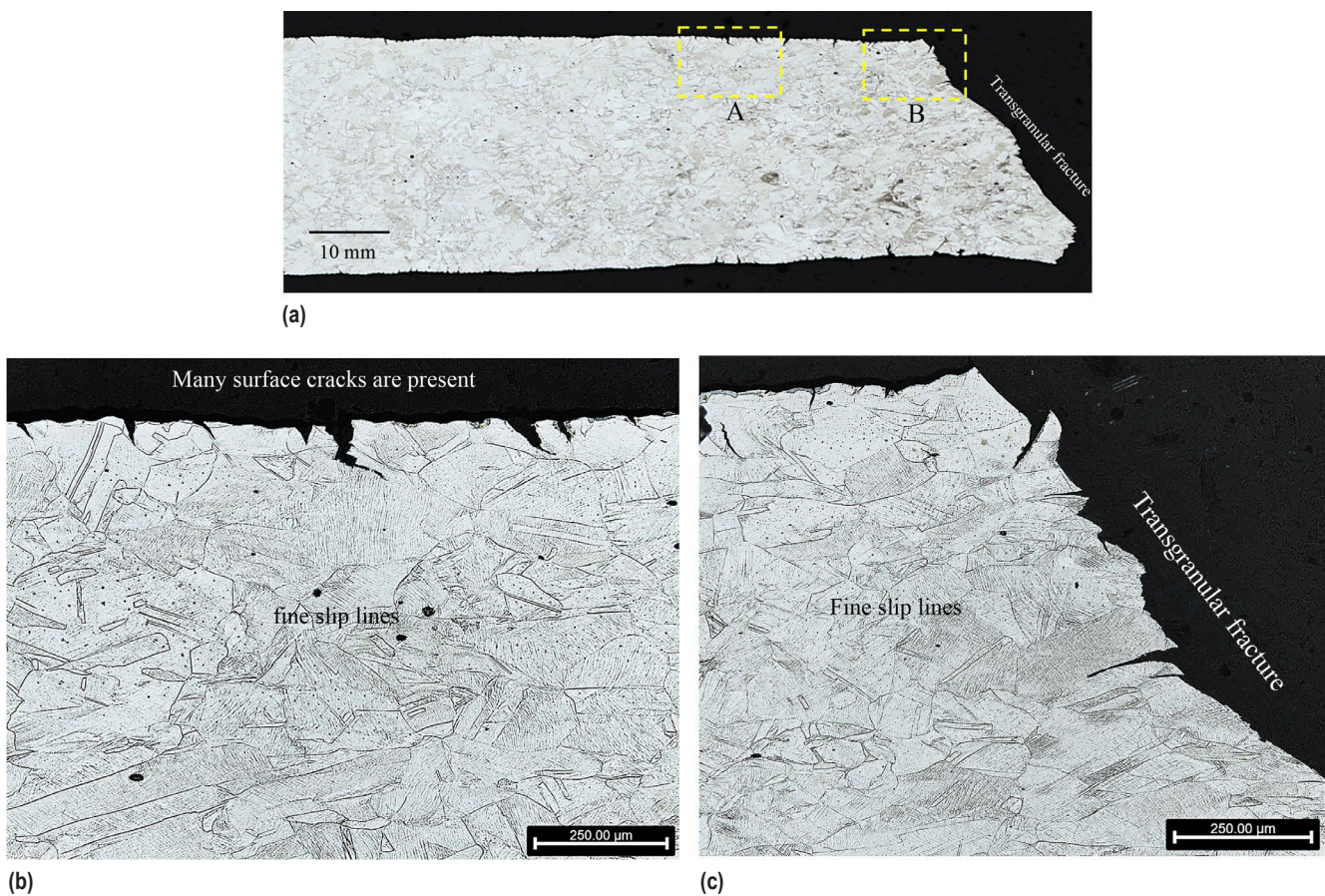


Figure 42. Optical micrographs showing (a) cross-sectional view of a fractured LP-DED NASA HR-1 tensile sample tested in 5 ksi gaseous hydrogen environment, (b) numerous slip lines are present and surface cracks are inclined approximately  $45^\circ$  with respect to the tensile loading axis that corresponds to the planes of near maximum shear stress (from region A in (a)), (c) signs of heavy deformation near the fracture surface and the fracture mode is ductile transgranular (from region B in (a)). This tensile specimen was in 1-step aged condition.

**3.4.3.2 Hydrogen Diffusion Analysis and Strain Rate Effects.** For metals stressed in a gaseous hydrogen environment, hydrogen-induced crack initiation typically starts at the gas-metal surface.<sup>56</sup> Hydrogen can dissociate on metal surfaces into H-atom and be physically absorbed and transported by diffusion through metal lattice. Upon further loading, the absorbed H-atom can be transported by dislocations to the regions of high stress and interacts with the material at the crack tip. In alloy 718 (Inconel 718), the resistance to HEE is related to hydrogen diffusion behavior and hydrogen transport by diffusion is an important consideration for interpreting susceptibility to HEE.<sup>57</sup> Diffusivity of hydrogen in superalloys varies slightly with composition of alloys. The diffusivity of lattice hydrogen at room temperature is on the order of  $10^{-16} \text{ m}^2/\text{s}$  in Fe-Cr-Ni austenitic steels and  $2 \times 10^{-15} \text{ m}^2/\text{s}$  in alloy 718.<sup>58,59</sup> The depth of hydrogen diffusion in LP-DEN NASA HR-1 was estimated using the bulk diffusivity of alloy 718 in hydrogen at room temperature ( $2 \times 10^{-15} \text{ m}^2/\text{s}$ ). The diffusion distance of hydrogen has a square root dependence on diffusivity and can be determined from the Equation below:

$$x = \sqrt{(Dt)} \quad (7)$$

where  $x$  is the diffusion distance traveled by the diffusing hydrogen atoms in one direction along one axis,  $D$  is diffusivity, and  $t$  is the elapsed time since diffusion began.<sup>58</sup> The diffusivity determines the time it takes for a hydrogen atom to diffuse a given distance in an alloy. Diffusion time increases with the square of diffusion distance and is inversely proportional to the diffusivity ( $D$ ).

The tensile testing strain rate for LP-DEN NASA HR-1 in hydrogen is 0.0001 in/in/min, which is more than an order of magnitude slower than that for the wrought alloy (0.005 in/in/min). The reduction in strain rate increases the testing time in a high pressure gaseous hydrogen environment from 20 – 25 minutes (at 0.005 in/in/min) for the wrought alloy to 450 – 650 minutes (at 0.0001 in/in/min strain rate) for the LP-DEN alloy. When a tensile test is performed at a strain rate of 0.005 in/in/min strain rate for 20 – 25 minutes, hydrogen atoms were able to diffuse over a distance of approximately 1.55 – 1.73  $\mu\text{m}$ . In comparison, when the strain rate is decreased to 0.0001 in/in/min, the exposure time in the hydrogen environment increases to 450 – 650 minutes, and the estimated depth of hydrogen diffusion at failure would increase from 2.19 to approximately 7.35 – 8.83  $\mu\text{m}$ . Therefore, the fraction of deforming material that is affected by hydrogen is considerably larger at 0.0001 in/in/min than at 0.005 in/in/min strain rate as the exposure time to high pressure hydrogen increased from 20 – 25 minutes to more than 450 minutes. This explains why HEE is more pronounced when tensile testing is performed at a lower strain rate.

The calculated hydrogen diffusion distance of 7.35 – 8.83  $\mu\text{m}$  (at 0.0001 in/in/min strain rate) is shorter than the observed depth of surface cracks, which is 20 – 100  $\mu\text{m}$  in most cases. The discrepancies could be caused by enhanced lattice diffusivity of hydrogen due to expanded crystal lattice (by elastic strain) or by dislocation assisted transportation. HEE is more pronounced at a lower strain rate because slow strain rate increases testing duration and promotes interaction of hydrogen and the moving dislocations.<sup>59,60</sup> At a higher strain rate, the diffusion of hydrogen may not be able to follow the dislocation motion. In contrast, hydrogen can diffuse deeper and follow the dislocation motion when strain rate is decreased to a certain level. Therefore, the interaction of hydrogen

with dislocation is enhanced and higher amount of hydrogen can be effectively transported by dislocations to the high stress regions when the strain rate is very slow. It is significant to note that LP-DED NASA HR-1 exhibits higher fracture elongation than the wrought alloy in high pressure hydrogen environment, despite tensile testing was conducted at a strain rate that is slower by one order of magnitude. The exceptional ductility of LP-DED NASA HR-1 in hydrogen can be attributed to (1) clean grain boundary that has very low density of detrimental  $\eta$  phase and (2) exceptional high ductility and strain hardening exponent that increase its ability to homogenize plastic deformation and retard stress concentration.

**3.4.3.3 Effects of Hydrogen on Fracture Features.** Fracture surfaces were analyzed using SEM to explore the effects of hydrogen on tensile fracture behavior. Figure 43 shows the SEM images of a 1-step aged sample after tensile testing in hydrogen. As shown, the fracture surface exhibits hydrogen-induced quasi-cleavage fracture near the specimen surface, a transition region with a mixed mode of quasi-cleavage and dimpled fracture, and ductile dimple fracture toward the central region. The quasi-cleavage fracture surface is typically flat but some traces of shallow dimples can be clearly seen in the high resolution images (Fig. 43(c), (d)). Transport of hydrogen by dislocations is enhanced when the strain rate is low as a higher amount of hydrogen can be transported to the stress concentration sites.<sup>59,60</sup> The interaction of gaseous hydrogen with the tensile sample is initially confined within its outer region. Surface cracks initiated and continued to grow. Hydrogen was transported deep into the material towards the end of the tensile test, leading to reduced fracture elongation. Outside of the transition region, the fracture surface exhibits predominant ductile failure toward the central region of the fracture surface. Intergranular fracture, which is the most severe form of HEE, is not present on the fracture surface.

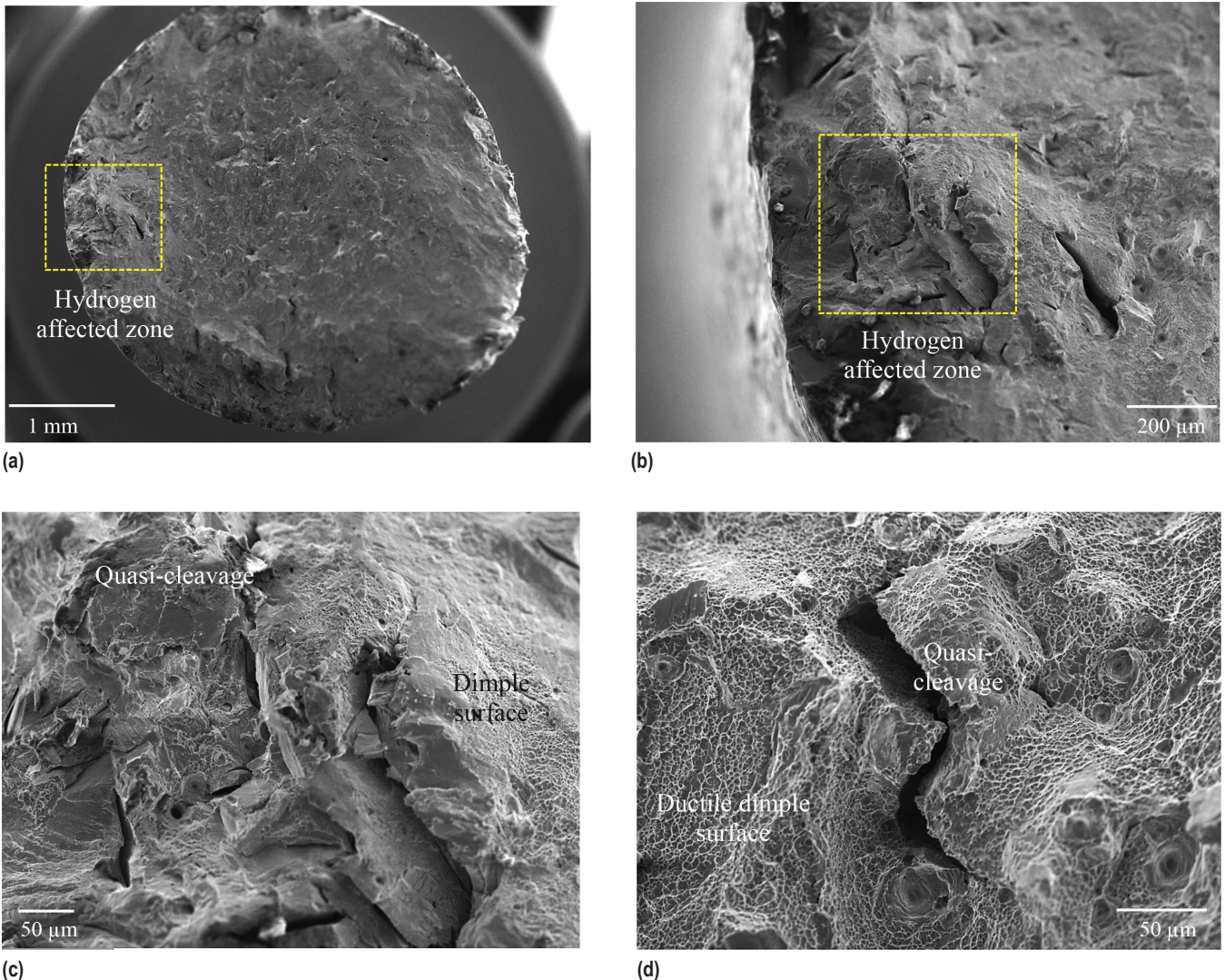


Figure 43. SEM fractography of a 1-step aged LP-DEN NASA HR-1 sample tensile tested in hydrogen showing (a) the overall fracture surface, (b) the HEE affected quasi-cleavage zone near surface (from the yellow box in (a)), (c) closeup view of the yellow box in (b), (d) the mixed quasi-cleavage and dimple fracture in the transition region

The fracture behavior of 2-step aged samples is similar to that of the 1-step aged samples as shown in Figure 44. Mixed quasi-cleavage fracture and ductile dimpled surface are the main characteristics near the specimen surface, indicative of hydrogen effects. As shown in Figure 44, the fracture surface exhibits hydrogen-induced quasi-cleavage fracture near the specimen surface, a transition region with a mixed mode of quasi-cleavage and dimpled fracture, and ductile dimple fracture toward the central region. The quasi-cleavage fracture surface is flat and mixed with secondary cracking but some traces of shallow dimples can be clearly seen in the high resolution image (Fig. 44(c), (d)). The fracture surface exhibits predominant ductile failure outside the transition region. Although there are a few hydrogen affected quasi-cleavage regions on

the fracture surface, the 2-step aged samples remains very ductile and have more than 33% fracture elongation after tensile testing in high pressure hydrogen environment for 8 – 10 hours. Overall, LP-DED NASA HR-1 remains very ductile in high pressure hydrogen and the fracture surface exhibits no signs of hydrogen-induced brittle intergranular fracture. Additional tensile testing is being completed for LP-DED NASA HR-1 in 5 ksi high pressure hydrogen environment using three different strain rates, 0.005, 0.0005, and 0.0001 in/in/min, so that the resistance to HEE for LP-DED NASA HR-1 and the wrought alloy can be compared under the same testing conditions.

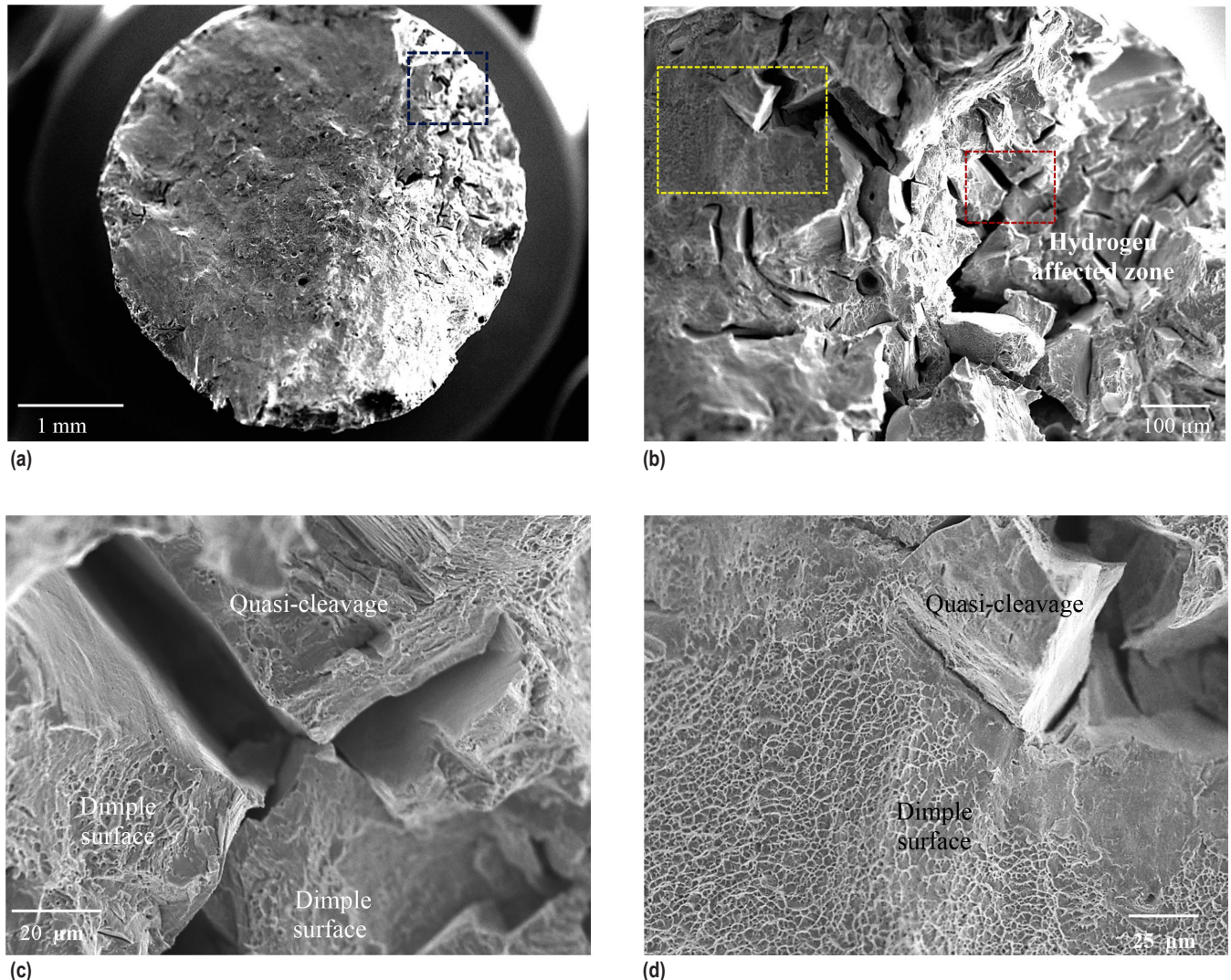


Figure 44. SEM Fractography of a 2-step aged sample tensile tested in hydrogen showing (a) the overall fracture surface, (b) the near surface hydrogen affected zone from the blue box in (a), (c) the mixed quasi-cleavage and ductile dimple fracture from the red box in (b), (d) predominant ductile dimple fracture outside of the quasi-cleavage zone from the yellow box in (b).

### 3.4.4 LCF Properties in High Pressure Gaseous Hydrogen Environment

LCF is the primary service life limit factor for LRE nozzles. High pressure gaseous hydrogen environment is known to have a considerable effect on LCF properties for HEE susceptible materials. In general, the strain-controlled LCF test is more sensitive to HEE than the load-controlled high cycle fatigue (HCF) test.<sup>26</sup> The greatest reduction in LCF life in high pressure hydrogen environment is found at near room temperature for most superalloys. Therefore, LCF testing was performed in 5 ksi gaseous hydrogen environment at room temperature at a strain ratio of  $-1$  ( $R = -1$ ) and a total strain of 2% to evaluate the effects of hydrogen on fatigue crack initiation and cycles to failure. The selection of 2% total strain range for LCF test in hydrogen is based on the projection that the maximum total strain the channel wall nozzle experiences during hot firing is around 2% in most cases.<sup>61</sup> Table 13 shows the LCF test results that include inelastic strain range, cycles to crack initiation, and cycles to failure. The LCF samples were heat treated with two different aging cycles. The inelastic strain increased slightly when the aging treatment is switched from 1-step to 2-step. The samples heat treated with 2-step aging cycle exhibit longer crack initiation life ( $N_i = 860 - 865$  cycles) than those heat treated with 1-step aging ( $N_i = 660 - 760$  cycles). Samples in 2-step aged condition also exhibit slightly longer LCF life than that in 1-step aged condition.

Table 13. LCF test results for LP-DED NASA HR-1 in 5 ksi high pressure hydrogen environment at room temperature.

Material	Environment	Strain Range	Aging Treatment	Specimen ID	Inelastic Strain at $N_h$ (%)	Cycles to Crack Initiation ( $N_i$ )	Cycles to Failure ( $N_f$ )
LP-DED NASA HR-1	5 ksi GH <sub>2</sub> , RT	-1% to 1%	1325 °F/16h	38	1.25	≈ 660	789
				39	1.25	≈ 760	918
				40	1.26	≈ 750	922
		-1% to 1%	1275 °F/16h + 1150 °F/16h	73	1.31	≈ 860	878
				74	1.33	≈ 865	884
				75	1.34	≈ 865	993

Table 14 presents the stress amplitudes at the maximum ( $\Delta\sigma_{max}$ ), first cycle ( $\Delta\sigma_{first}$ ) and half-life ( $\Delta\sigma_{half}$ ) cycle for LP-DED NASA HR-1 in both one-step and two-step aged conditions. Strain-controlled LCF life generally depends not only on the strength-ductility properties but also on the cyclic hardening behavior. To quantitatively study the effect of hydrogen on cyclic hardening behavior, the ratios of cyclic hardening ratio (HR) and cyclic softening ratio (SR) were calculated using Equation (5) and (6). HR and SR are two important parameters in characterizing cyclic deformation behavior and the results are shown in Table 14. As shown in Table 14, the 2-step aged specimen exhibited a high HR and a lower HR at 2% total strain in hydrogen. This

is consistent with the LCF test results in ambient air that samples in 2-step aged condition have more pronounced cyclic hardening response than that in 1-step aged condition. The material with a higher HR and a lower SR tends to possess enhanced cyclic hardening capability that can homogenize plastic deformation and prolong LCF life. The 2-step aged specimens having longer crack initiation life can be attributed to the enhanced cyclic hardening ability, which leads to more homogeneous plastic deformation and delayed crack initiation.

Table 14. Comparison of the stress amplitudes at the maximum ( $\Delta\sigma_{\max}$ ), first cycle ( $\Delta\sigma_{\text{first}}$ ) and half-life ( $\Delta\sigma_{\text{half}}$ ) cycles for LP-DED NASA HR-1 tested at 2% total strain in 5 ksi gaseous hydrogen environment. The LCF specimens were heat treated with two different aging cycles. HR and SR values are also given in this Table.

Material	Environment	Strain Range	Aging Treatment	Specimen ID	$\Delta\sigma_{\max}$ (ksi)	$\Delta\sigma_{\text{half}}$ (ksi)	$\Delta\sigma_{\text{first}}$ (ksi)	HR	SR
LP-DED NASA HR-1	5ksi GH <sub>2</sub> , RT	-1% to 1%	1325 °F/16h	38	125.9	108.41	98.83	0.27	0.14
				39	122.1	106.42	98.77	0.24	0.13
				40	119.1	108.62	97.22	0.23	0.09
		-1% to 1%	1275 °F/16h + 1150 °F/16h	73	109.9	99.89	81.47	0.35	0.09
				74	107.1	98.22	79.93	0.34	0.08
				75	104.5	97.71	80.02	0.31	0.06

$\Delta\sigma_{\max}$  (ksi) = the maximum stress amplitude

$\Delta\sigma_{\text{half}}$  (ksi) = the stress amplitude at half life

$\Delta\sigma_{\text{first}}$  (ksi) = the stress amplitude at the first cycle

HR = the hardening ratio

SR = the softening ratio

**3.4.4.1 Hysteresis loops.** Cyclic hardening behavior was analyzed using hysteresis loops to understand the LCF behavior of LP-DED NASA HR-1 in high pressure hydrogen environment. The hysteresis loops of the first cycle, cycle 15, and the half-life cycle for both 1-step and 2-step aged samples are illustrated in Figure 45. The hysteresis loops are nearly symmetrical under both aging conditions. There is significant cyclic hardening in the early cycles and the strain hardening response stabilizes and reaches a steady state near the half-life cycle. One noticeable difference is the level of cyclic hardening varies with aging treatment. As shown in Figure 45, the peak cyclic tensile stress increased by 12.9 ksi from 97.1 ksi in the 1st cycle to 110.0 ksi at the half life cycle in 1-step aged condition. In comparison, the peak tensile stress increased by 19.3 ksi from 80.2 in the 1<sup>st</sup> cycle to 99.5 ksi at the half life cycle in 2-step aged condition. It is evident that 2-step aging enhances cyclic hardening response. This is consistent with the LCF test results in ambient air that samples in 2-step aged condition display more pronounced cyclic hardening response than that in 1-step aged condition.

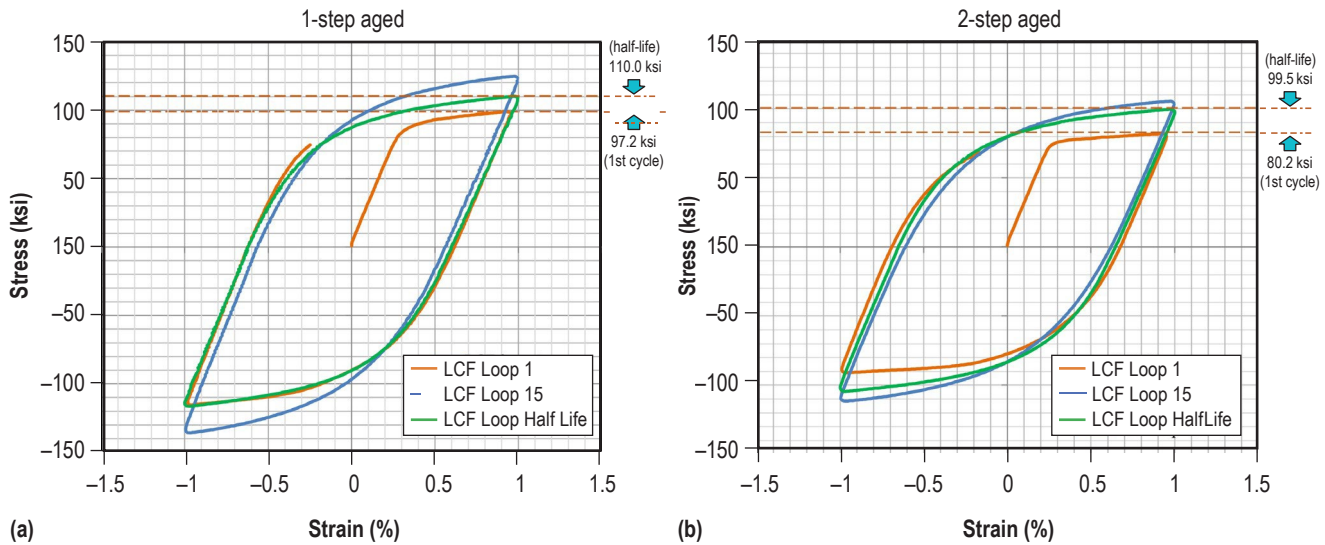


Figure 45. LP-DEN NASA HR-1 LCF tested in 5 ksi gaseous hydrogen environment at 2% total strain showing the typical hysteresis loops of the first cycle, the peak stress cycle (cycle 15), and the half-life cycle in (a) 1-step aged condition and (b) 2-step aged condition.

**34.4.2 Cyclic Stress Response.** The variations in the magnitudes of the peak tensile ( $\sigma_{\max}$ ) and compressive stresses ( $\sigma_{\min}$ ) with number of cycles ( $N$ ) at two different aged conditions are shown in Figure 46. Strain amplitude is held constant throughout the test and peak tensile and compressive stresses are plotted for each aging cycle. Both 1-step and 2-step aged samples display significant cyclic strain hardening in the first 10–15 cycles. The initial cyclic hardening was very brief, and the cyclic hardening response decreased progressively and reached a stable state after approximately 200 cycles. Both crack initiation life and fatigue life can be determined from the stress vs. cycle ( $N$ ) plot. The material maintains a cyclically stable condition for 70%–80% of the fatigue life until the onset of crack initiation ( $N_i$ ), after which accelerated cyclic softening occurred at final LCF stage, approximately within the final 10%–20% of the fatigue life. The growth of fatigue crack accelerated at late stage of LCF testing and cyclic stress amplitude falls rapidly until the final fracture. Failure of the LCF samples was gradual as there is no sign of an abrupt drop in stress amplitude after crack initiation.

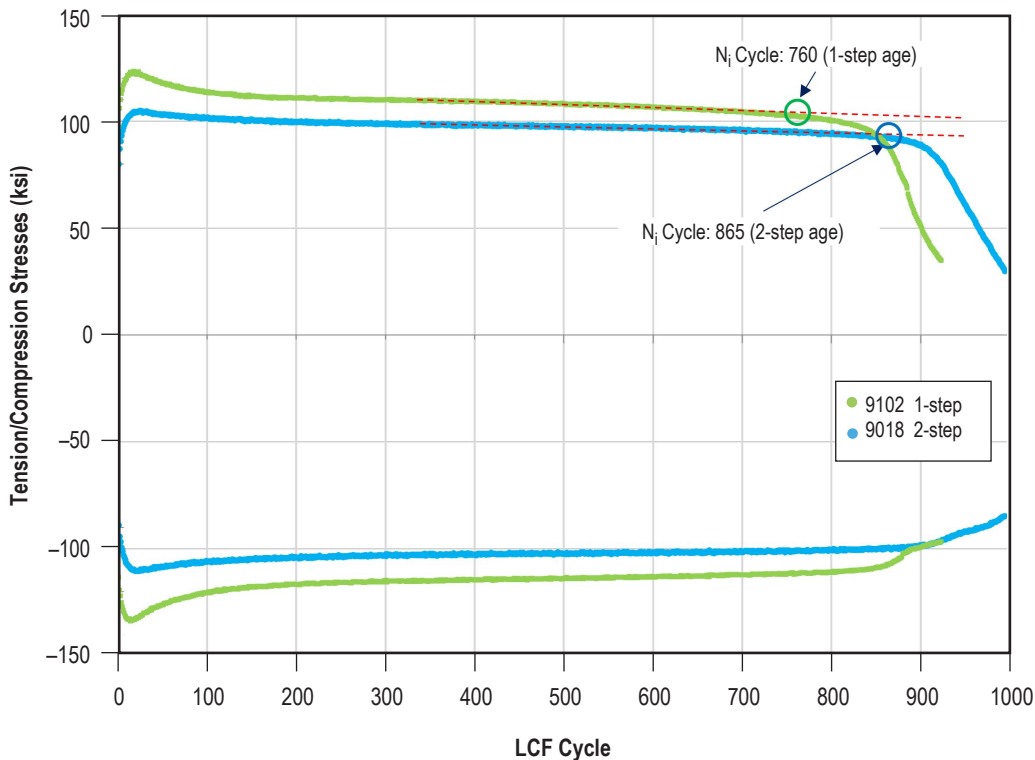


Figure 46. Variations of peak tensile stress ( $\sigma_{\max}$ ) and compressive stress ( $\sigma_{\min}$ ) with number of cycles (N) at 2% total strain (1% strain amplitude) in high pressure gaseous hydrogen environment. The LCF specimens were heat treated with two different aging cycles.

The total LCF life can be divided into two parts: crack initiation life and crack propagation life. It is often considered that the fatigue life is determined by crack initiation cycle, Ni. After the Ni cycle, crack propagation accelerates and the load carrying capability of the component drops quickly. Due to the presence of a sizable crack, the component becomes fracture critical, and its safety and reliability depend on damage tolerance assessment and control. 2-step aging appears to provide a higher resistance to crack initiation that can be attributed to the enhanced cyclic hardening capability (higher HR and lower SR) as shown in Table 14. Therefore, 2-step aging treatment is better suited for components that are to be used for LCF critical applications in high pressure hydrogen environments, such as some HEE sensitive components for LRE applications.

**3.4.4.3 LCF Induced Fracture Features in Hydrogen.** SEM was used to examine the fracture surfaces to observe the effects of hydrogen on LCF fracture behavior. Figure 47 shows the fracture surfaces of LP-DED NASA HR-1 samples in two different aging conditions. There are three distinct regions on the fracture surface that consist of fatigue-crack initiation, crack propagation, and final fast-fracture zones (as indicated by dashed white and yellow lines). It can be seen from Figure 48(a) that the fatigue crack initiated from the specimen surface, caused by localized dislocation slip bands on certain crystallographic planes. Slip bands are a result of the systematic buildup of fine dislocation slip movements. There is no sign that the fatigue cracks initiated from the near surface defects, such as internal pores. Both 1-step and 2-step aged specimens have

multiple crack initiation sites. The small fatigue cracks grew, coalesced, and advanced further in a direction normal to the applied stress, forming a large propagation zone as shown in Figure 47. Both 1-step and 2-step aged specimens exhibit similar fracture surface characteristics. The most noticeable difference between the samples tested in ambient air (see Fig. 36) and in 5 ksi hydrogen environment (see Fig. 47) is in the crack initiation stage. The LCF samples tested in hydrogen exhibit an increase in the crack initiation density (more fatigue crack initiation sites in the initiation zone) than that tested in ambient air. This is consistent with the findings that hydrogen increases the density of fatigue induced surface cracks due to enhanced interaction of dislocation slip bands with hydrogen.<sup>62</sup>

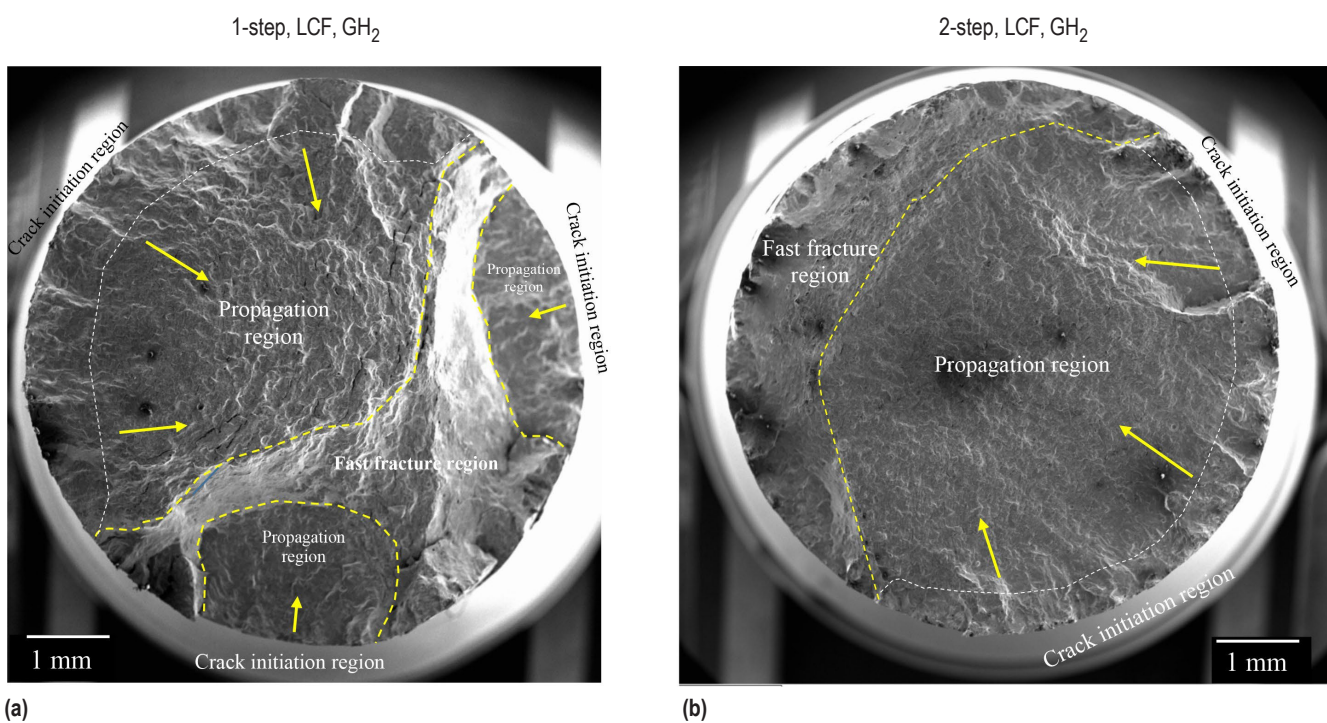


Figure 47. LCF fracture surfaces of LP-DED NASA HR-1 tested at 2.0% total strain in 5 ksi high pressure hydrogen environment in (a) 1-step and (b) 2-step aged condition.

Overall, the fracture surfaces of the LCF specimens tested in hydrogen displays no signs of brittle intergranular fracture. There are distinct striation marks in the fatigue propagation zone as shown in Figure 48. Striations are fatigue propagation marks produced on the fracture surface that show the incremental growth of a fatigue crack. Striations are generally not seen when a crack is small, but begin to appear as the crack becomes larger. Each striation represents fatigue crack growth per cycle and the width of a striation is indicative of the overall crack growth rate. The striation spacing during the early stage of crack propagation ranges from 10 – 20  $\mu\text{m}$ . Fatigue striation mark is the typical characteristic of crack propagation in a very ductile material.<sup>44</sup> Therefore, the presence of distinct fatigue striations indicates LP-DED NASA HR-1 remains very ductile during LCF testing in high pressure hydrogen environment.

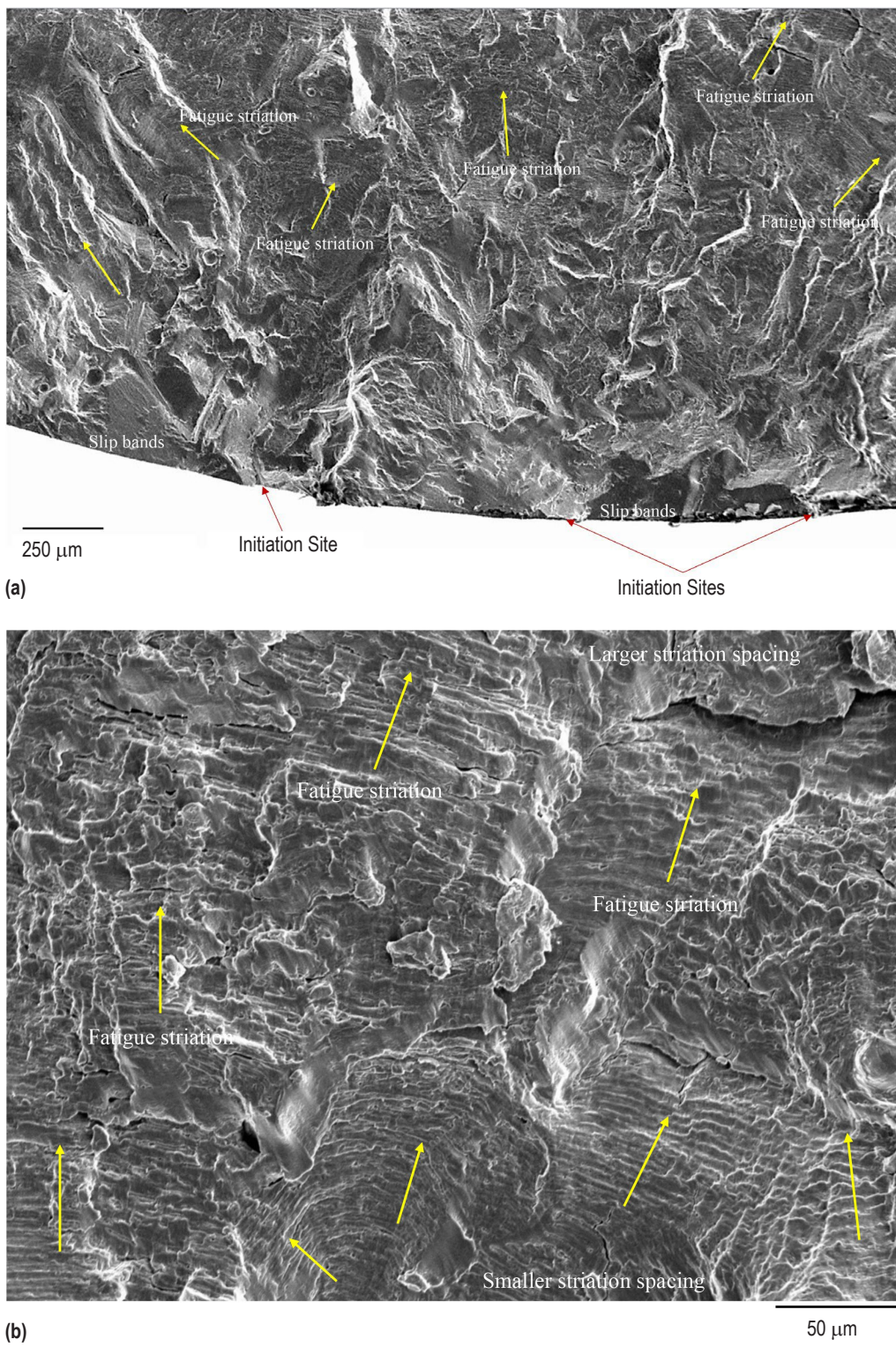


Figure 48. SEM fractographs of a 1-step aged specimen showing (a) LCF crack initiation in multiple sites and (b) distinct striation marks showing directions of early stage of crack propagation in the fatigue crack propagation region.

**3.4.4.4 Comparison of LCF Behavior in Air and Hydrogen.** LCF testing in a high pressure hydrogen environment has little effect on the fatigue life of LP-DED NASA HR-1 as compared to that tested in ambient air. As shown in Figure 49, LCF life of LP-DED NASA HR-1 in hydrogen is comparable to that in air at 2% total strain. In 1-step aged condition, the average LCF life is 870 cycles in ambient air and 876 cycles in hydrogen at 2% total strain amplitude. In 2-step aged condition, the average LCF life is 1053 cycles in air and 918 cycles in hydrogen at 2% total strain. Overall, the 2-step aged material exhibit longer LCF life than the 1-step aged material in both ambient air and hydrogen environments. For LCF testing at 2% total strain, plastic strain component predominates and ductility is more important than strength. Therefore, it is not surprising to see LP-DED NASA HR-1 has excellent LCF resistance at 2% total strain amplitude in both ambient air and hydrogen as it is very ductile and has high strain hardening capability that prolongs fatigue life. The excellent LCF performance in hydrogen makes LP-DED NASA HR-1 an ideal material for LRE structures that are subjected to repeated thermal and mechanical loads in the challenging high pressure hydrogen environment.

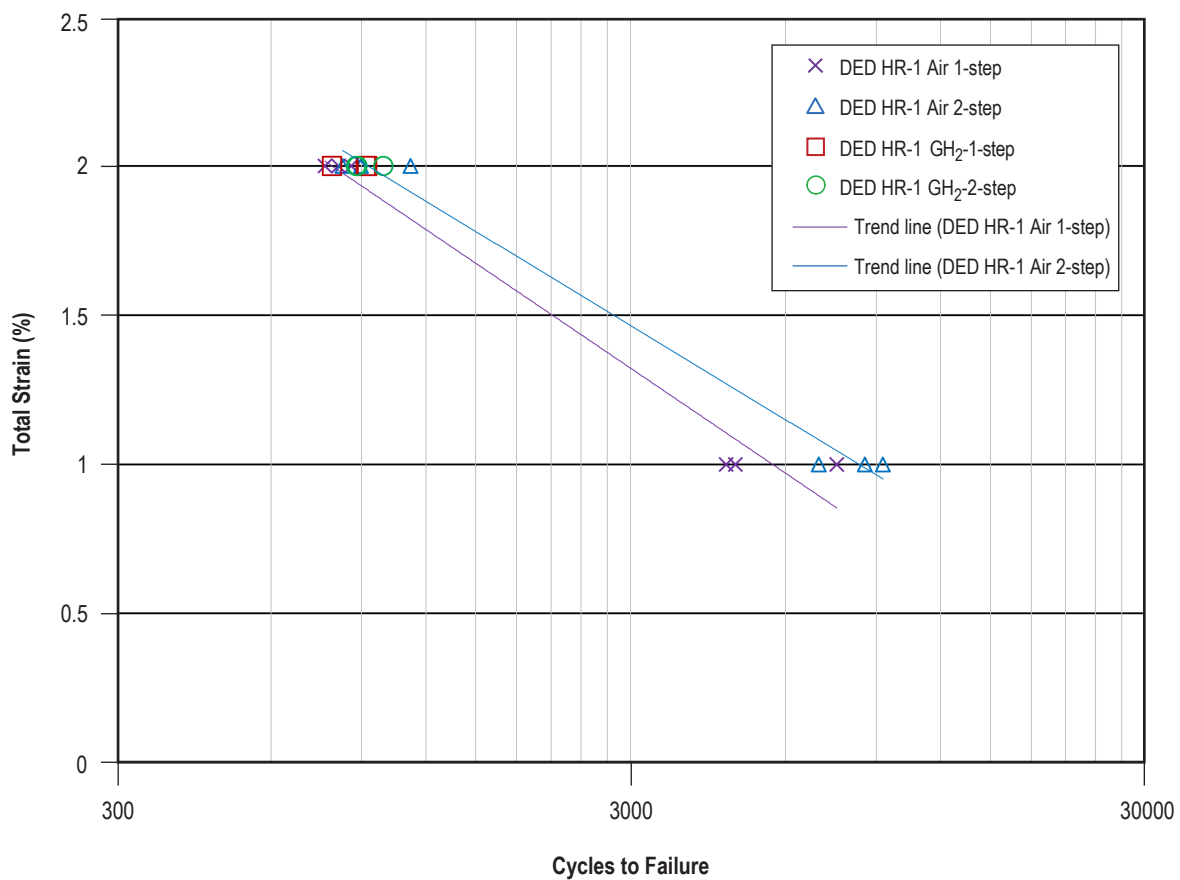


Figure 49. LCF life comparison for LP-DED NASA HR-1 in air vs. in hydrogen. The LP-DED LCF specimens were heat treated using two different aging cycles, 1-step and 2-step aging.

### 3.4.4.5 Comparison of LCF Life in Hydrogen for LP-DED and Wrought NASA HR-1.

Figure 50 shows LCF life comparison for wrought and LP-DED NASA HR-1 tested in high pressure hydrogen environment. Although wrought NASA HR-1 exhibits little or no loss in tensile fracture elongation in 5 ksi gaseous hydrogen environment, the presence of hydrogen significantly degrades its LCF life.<sup>5</sup> In comparison, high pressure hydrogen environment has little effect on the LCF life of LP-DED NASA HR-1. Aging for wrought NASA HR-1 was conducted by the standard 1-step cycle at 1325 °F/16h. LP-DED NASA HR-1 was aged with two different cycles, the standard 1-step aging at 1325 °F/16h and 2-step aging at 1275 °F/16h + 1150 °F/16h. In 1-step aged condition, the average LCF life in hydrogen is 876 cycle for LP-DED NASA HR-1 and 315 cycles for the wrought alloy at 2% total strain. The average LCF life in hydrogen increased to 918 cycles for the 2-step aged material. It is obvious that the LCF resistance of LP-DED NASA HR-1 in high pressure gaseous hydrogen environment is superior to that of the wrought alloy.

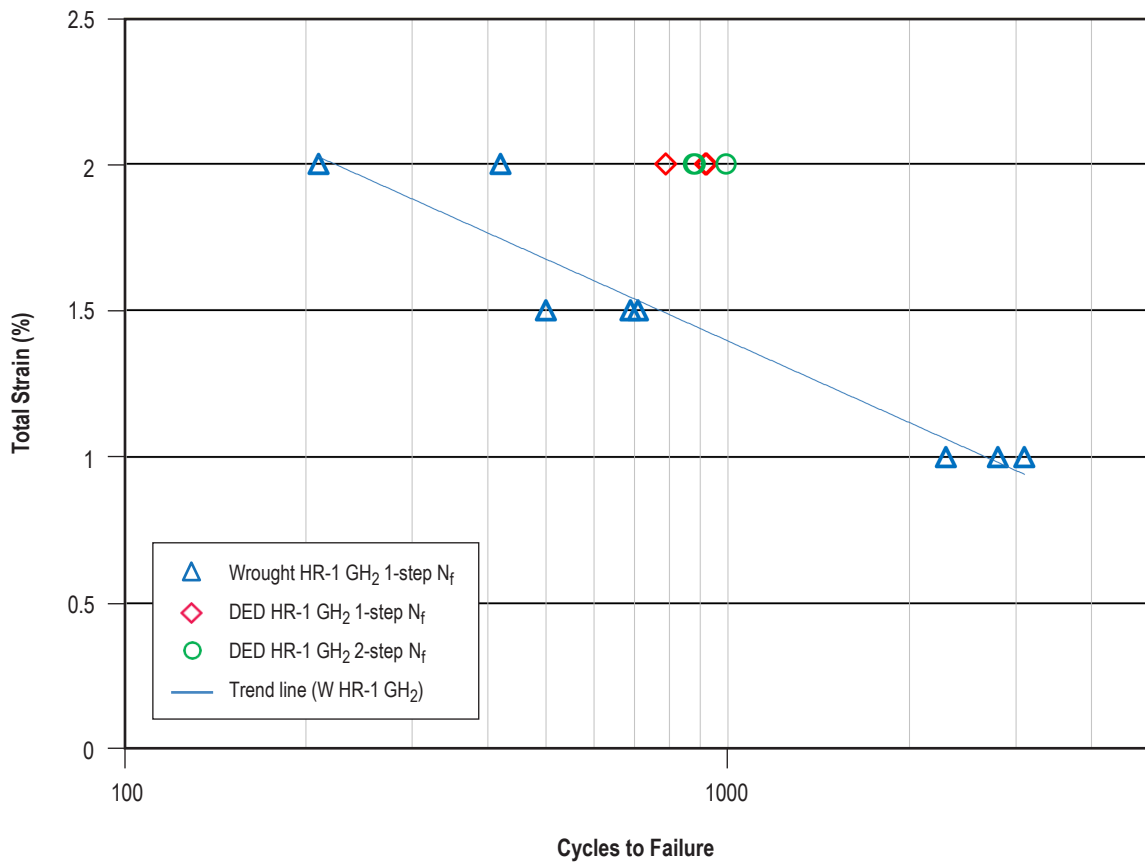


Figure 50. Effects of high pressure hydrogen on LCF life of LP-DED and wrought NASA HR-1. Aging for wrought NASA HR-1 was conducted at 1325 °F/16h. LP-DED NASA HR-1 was aged with two different cycles, 1-step aging at 1325 °F/16h and 2-step aging at 1275 °F/16h + 1,150 °F/16h. LCF resistance of LP-DED NASA HR-1 in hydrogen is significantly better than that of the wrought alloy.

Low cycle fatigue (strain life fatigue) depends on the strength-ductility properties and the cyclic hardening or softening behaviors of the material. The cyclic hardening behavior of wrought NASA HR-1 is not known as the LCF hysteresis loop data is unavailable. However, cyclic hardening behavior can be estimated using the tensile UTS/YS ratio.<sup>63</sup> Table 15 compares the tensile properties and UTS/YS ratio for LP-DED and wrought NASA HR-1 in high pressure helium and hydrogen environments.<sup>64</sup> As shown, wrought NASA HR-1 has lower UTS/YS ratio (1.34 – 1.36) than the LP-DED alloy (1.64 – 1.87) in high pressure hydrogen environment. Having a lower UTS/YS ratio suggests the wrought alloy would have lower cyclic hardening capability than the LP-DED alloy. Dislocation slip character can play an important role in the HEE susceptibility.<sup>60</sup> Microstructure that can homogenization plastic strain and avoid strain concentration generally contributes to higher resistance to fatigue crack initiation. Therefore, LP-DED NASA HR-1 exhibiting better LCF performance than its wrought counterpart in hydrogen can be attributed to cumulative effects of higher ductility and improved cyclic hardening capability.

Table 15. The average tensile properties for LP-DED and wrought NASA HR-1 in high pressure helium and hydrogen environments.

Material	Aging Treatment	Strain Rate (in/in//min)	Test Environment	YS (ksi)	UTS (ksi)	Ductility (%)	UTS/YS Ratio	Strain Hardening Exponent (n)
LP-DED NASA HR-1	1-step	0.05	5 ksi GHe	102.08	170.17	34.50	1.67	0.234
		0.0001	5 ksi GH <sub>2</sub>	98.82	161.81	28.75	1.64	0.237
<hr/>								
LP-DED NASA HR-1	2-step	0.05	5 ksi GHe	86.99	162.26	41.73	1.87	0.279
		0.0001	5 ksi GH <sub>2</sub>	87.55	151.35	33.10	1.73	0.278
<hr/>								
Wrought NASA HR-1	1-step	0.05	5 ksi GHe	136.93	183.07	23.57	1.34	-
		0.005	5 ksi GH <sub>2</sub>	128.83	175.37	23.40	1.36	-

LCF life is often dominated by crack initiation, and microstructure that can homogeneously distribute plastic strain is desirable. The alternating tensile and compressive strains lead to surface intrusions that initiate fatigue cracks. High pressure hydrogen environments can reduce LCF life by promoting planar dislocation slips and forming localized slip bands, which intensify metal/hydrogen interactions and accelerate fatigue crack initiation.<sup>60,62</sup> Higher strength materials are not desirable for LCF critical applications as they generally increase plastic strain localization during LCF testing. The ideal LCF resistant material for structural applications in high pressure hydrogen environment should have the following characteristics: (1) higher ductility and lower strength to accommodate plastic strains at critical locations (notches, inclusions, voids, etc.); (2) a high strain hardening exponent to enhance cyclic hardening and maintain cyclic stability; (3) clean grain boundaries that are free of deleterious  $\eta$  phase to minimize HEE susceptibility.

Therefore, it is postulated that wrought NASA HR-1 having inferior LCF performance in hydrogen can be attributed to its higher strength, lower ductility, and lower cyclic hardening capability. For LP-DED NASA HR-1, the enhanced strain hardening capability minimizes strain localization under the influence of hydrogen, leading to delayed crack initiation and improved LCF performance in high pressure hydrogen environment.

### 3.4.5 Thermal Conductivity

Thermo-physical properties of LP-DED NASA HR-1 (initial formulation) were investigated at Marshall Space Flight Center. Specific heat capacity, thermal diffusivity, and room temperature bulk density were measured to compute thermal conductivity by the following Equation:

$$\lambda = \alpha C_p \rho \quad (8)$$

where  $\lambda$  is the thermal conductivity,  $\alpha$  is the thermal diffusivity, typically in  $\text{mm}^2/\text{s}$ ,  $C_p$  is the specific heat capacity, typically in  $\text{J/gK}$ , and  $\rho$  is the density, typically in  $\text{g/cm}^3$ . The nominal chemical composition and aging cycle for LP-DED NASA HR-1 (initial composition) are shown in Table 16. LP-DED NASA HR-1 (initial formulation) was aged using a 2-step aging cycle at  $1275\text{ }^\circ\text{F}/16\text{h} + 1150\text{ }^\circ\text{F}/16\text{h}$ .

Table 16. Nominal chemical composition (wt%) of wrought and LP-DED NASA HR-1 and the aging cycle used for thermal conductivity analysis.

Alloy	Fe	Ni	Cr	Mo	V	W	Co	Ti	Al	Aging cycle
LP-DED NASA HR-1 (Initial formulation)	39.80	34.00	15.50	2.20	0.32	2.10	3.30	2.50	0.25	$1275\text{ }^\circ\text{F}/16\text{h} + 1150\text{ }^\circ\text{F}/16\text{h}$
Wrought NASA HR-1	38.90	34.10	15.50	2.40	0.30	2.20	3.50	2.80	0.30	$1325\text{ }^\circ\text{F}/16\text{h}$
LP-DED NASA HR-1 (Final formulation)	41.20	34.00	14.60	1.80	0.30	1.60	3.80	2.40	0.25	$1275\text{ }^\circ\text{F}/16\text{h} + 1150\text{ }^\circ\text{F}/16\text{h}$

The thermal diffusivity ( $\alpha$ ) of LP-DED NASA HR-1 (initial formulation) was measured by laser flash method with the Flashline 3050 System from Antercorp. Round sample discs approximately 16mm in diameter and 5mm thick were machined from a fully heat treated LP-DED NASA HR-1 rod. In this method, the front surface of the small disk-shaped sample is subjected to a very short burst of radiant energy from a laser pulse with a radiation time of 1 ms or less. The resulting temperature rise of the rear surface of the sample is measured and thermal diffusivity is calculated from the temperature rise versus time. Once the test is started, the system heats the sample to several temperatures to take a thermal diffusivity measurement at each temperature. Argon gas is purged into the sample chamber continuously during the test to prevent oxidation of the sample. The measurements of the specific heat ( $C_p$ ) were carried out in the range of  $60\text{--}600\text{ }^\circ\text{C}$

by DSC (Differential Scanning Calorimetry) with the DSC-Q20 system from TA Instruments. The specific heat of LP-DED NASA HR-1 was deduced from the numerical fit in the measuring temperature range. The density at different temperature was calculated using linear coefficient of thermal expansion of  $9.2 \times 10^{-6}/\text{°K}$  over a temperature range of 20 °C to 880 °C. The thermo-physical properties of LP-DED NASA HR-1 (initial composition) are shown in Table 17.

Table 17. Thermal diffusivity, thermal conductivity, and specific heat of LP-DED NASA HR-1 (initial formulation) as a function of temperature.

LP-DED NASA HR-1 (initial formulation) – Density: 8.025 g/cm <sup>3</sup>			
Temperature (°C)	Thermal Diffusivity (mm <sup>2</sup> /sec)	Specific Heat (J/gK)	Thermal Conductivity (W/mK)
51	3.45	–	12.67
123	3.34	0.480	12.676
181	3.60	0.499	14.018
276	3.82	0.524	15.488
338	3.99	0.537	16.594
412	4.21	0.544	18.031
487	4.38	0.541	19.308
566	4.50	0.571	20.429
646	4.59	–	21.445
724	4.83	–	23.188
804	4.97	–	24.512
879	5.12	–	25.879

The thermo-physical properties of wrought NASA HR-1 were determined at TPRL (Thermophysical Properties Research Laboratory, Inc.).<sup>64</sup> The nominal chemical composition for wrought NASA HR-1 is given in Table 16. Aging for wrought NASA HR-1 was conducted by the standard 1-step cycle at 1325 °F/16h. Thermal diffusivity was also measured by laser flash method in the temperature range of 23–650 °C. Specific heat capacity was measured from liquid nitrogen (−196 °C) to 990 °C. The push-rod dilatometer method was used to determine coefficient of thermal expansion (CTE) over a temperature range of liquid nitrogen (−196 °C) to 650 °C. The thermo-physical properties of wrought NASA HR-1 are presented in Table 18. As a comparison, the thermophysical properties of LP-DED NASA HR-1 (final formulation) originated from a published reference are given in Table 19.<sup>65</sup> The nominal chemical composition for LP-DED NASA HR-1 (final formulation) is given in Table 16. Aging for LP-DED NASA HR-1 (final formulation) was performed with a 2-step aging cycle at 1275 °F/16h + 1150 °F/16h.

Table 18. Thermal diffusivity, thermal conductivity, and specific heat of wrought NASA HR-1 as a function of temperature.

Wrought NASA HR-1 – Density: 8.07 g/cm <sup>3</sup>			
Temperature (°C)	Thermal Diffusivity (mm <sup>2</sup> /sec)	Specific Heat (J/gK)	Thermal Conductivity (W/mK)
-180	–	–	6.4
-150	–	0.356	7.1
-100	–	0.398	8.4
-50	–	0.431	9.4
0	–	0.451	10.4
23	3.10	0.459	10.7
50	3.21	0.463	11.2
100	3.40	0.470	12
200	3.77	0.478	13.9
300	4.13	0.495	15.7
400	4.46	0.505	17.5
500	4.77	0.515	19.3
600	5.04	0.550	21.2
650	5.14	0.563	22.4

Table 19. Thermal diffusivity, thermal conductivity, and specific heat of LP-DED NASA HR-1 (final formulation) as a function of temperature.<sup>65</sup>

LP-DED NASA HR-1 (final formulation) – Density: 8.09 g/cm <sup>3</sup>			
Temperature (°C)	Thermal Diffusivity (mm <sup>2</sup> /sec)	Specific Hea (J/gK)	Thermal Conductivity (W/mK)
25	3.25	0.509	13.6
100	3.49	0.505	14.5
200	3.82	0.527	16.5
300	4.15	0.547	18.5
400	4.45	0.560	20.2
500	4.74	0.576	22.0
600	5.01	0.611	24.5
700	5.32	0.639	27.1
800	5.39	0.673	28.8
900	5.49	0.71	30.8
1000	5.76	0.74	33.4

Figure 51 shows the comparison of thermal conductivity for LP-DED NASA HR-1 (initial composition), the wrought alloy, and the LP-DED NASA HR-1 final composition.<sup>65</sup> It can be seen that the measured thermal conductivity ( $\lambda$ ) values of LP-DED NASA HR-1 (initial formulation) agree well with the data of the wrought alloy. However, the thermal conductivity values of LP-DED NASA HR-1 (final formulation) are significantly higher than that of LP-DED NASA HR-1 (initial formulation) and the wrought alloy by approximately 15–20 %.<sup>65</sup>

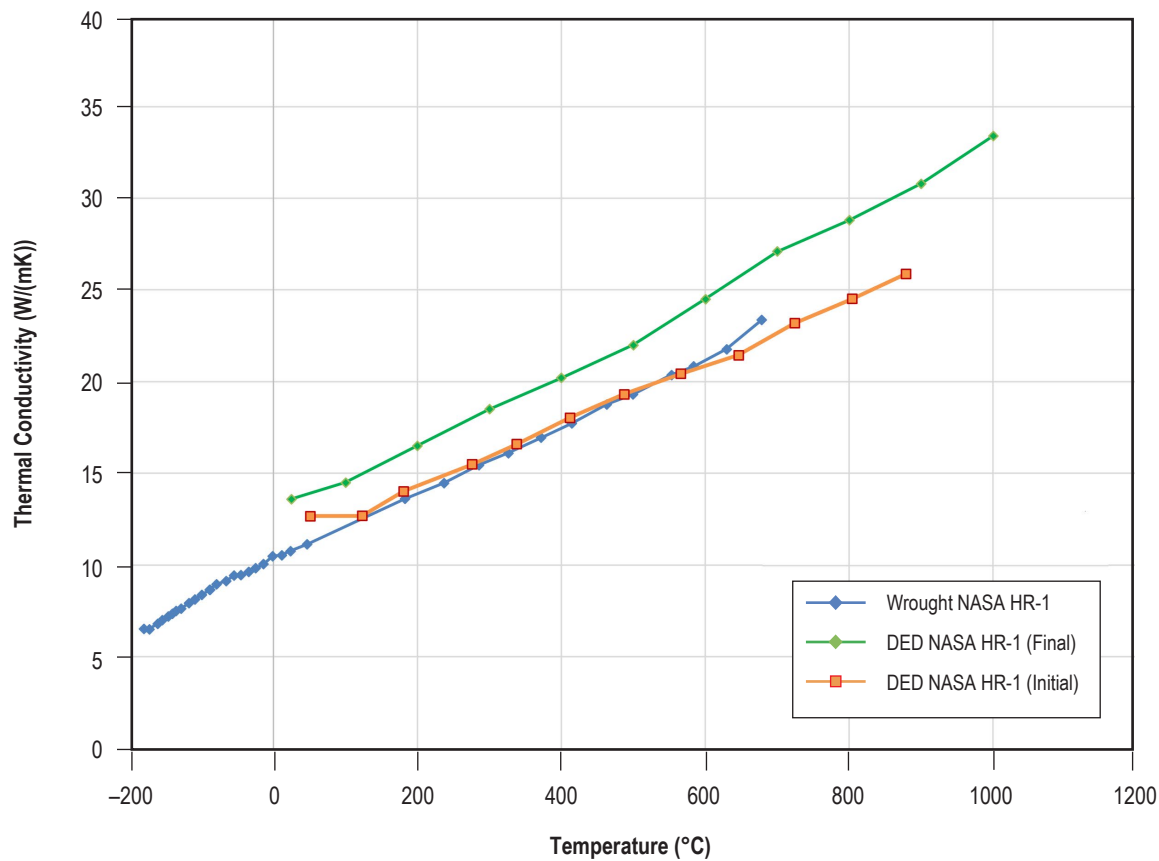


Figure 51. Comparison of thermal conductivity for LP-DED NASA HR-1 (initial composition), the wrought alloy, and the known literature data for LP-DED NASA HR-1 (final composition).<sup>65</sup>

The comparison of thermal diffusivity for LP-DED NASA HR-1 (initial composition), the wrought alloy, and LP-DED NASA HR-1 (final composition) is shown in Figure 52.<sup>65</sup> It can be seen that the thermal diffusivity ( $\alpha$ ) values of wrought NASA HR-1 (initial formulation) agree well with the literature data of LP-DED NASA HR-1 (final composition).<sup>65</sup> The thermal diffusivity values obtained for LP-DED NASA HR-1 (initial formulation) is lower than that of the wrought alloy and the LP-DED NASA HR-1 (final formulation) in the literature by approximately 5 – 15 %.<sup>65</sup> The discrepancy in thermal diffusivity likely results from variation that exists between different testing labs.

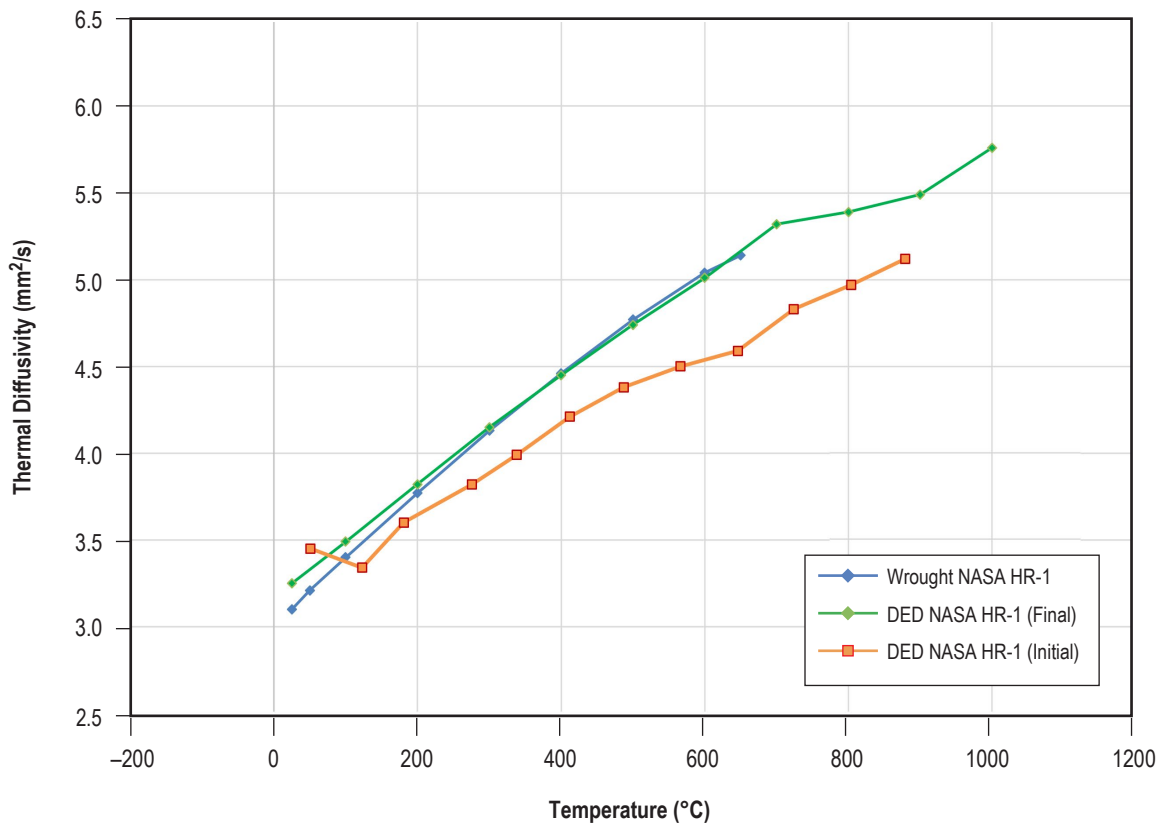


Figure 52. Comparison of thermal diffusivity for LP-DED NASA HR-1 (initial composition), the wrought alloy, and the known literature data for LP-DED NASA HR-1 (final composition).<sup>65</sup>

Figure 53 shows the comparison of heat capacity for LP-DED NASA HR-1 (initial composition), the wrought alloy, and the known literature data for LP-DED NASA HR-1 (final composition).<sup>65</sup> It can be seen that there are noticeable differences in the measured heat capacity ( $C_p$ ) values for LP-DED NASA HR-1 (initial formulation), the wrought alloy, and LP-DED NASA HR-1 (final formulation) in.<sup>65</sup> It is interesting to note that LP-DED NASA HR-1 has higher specific heat capacity than the wrought alloy.

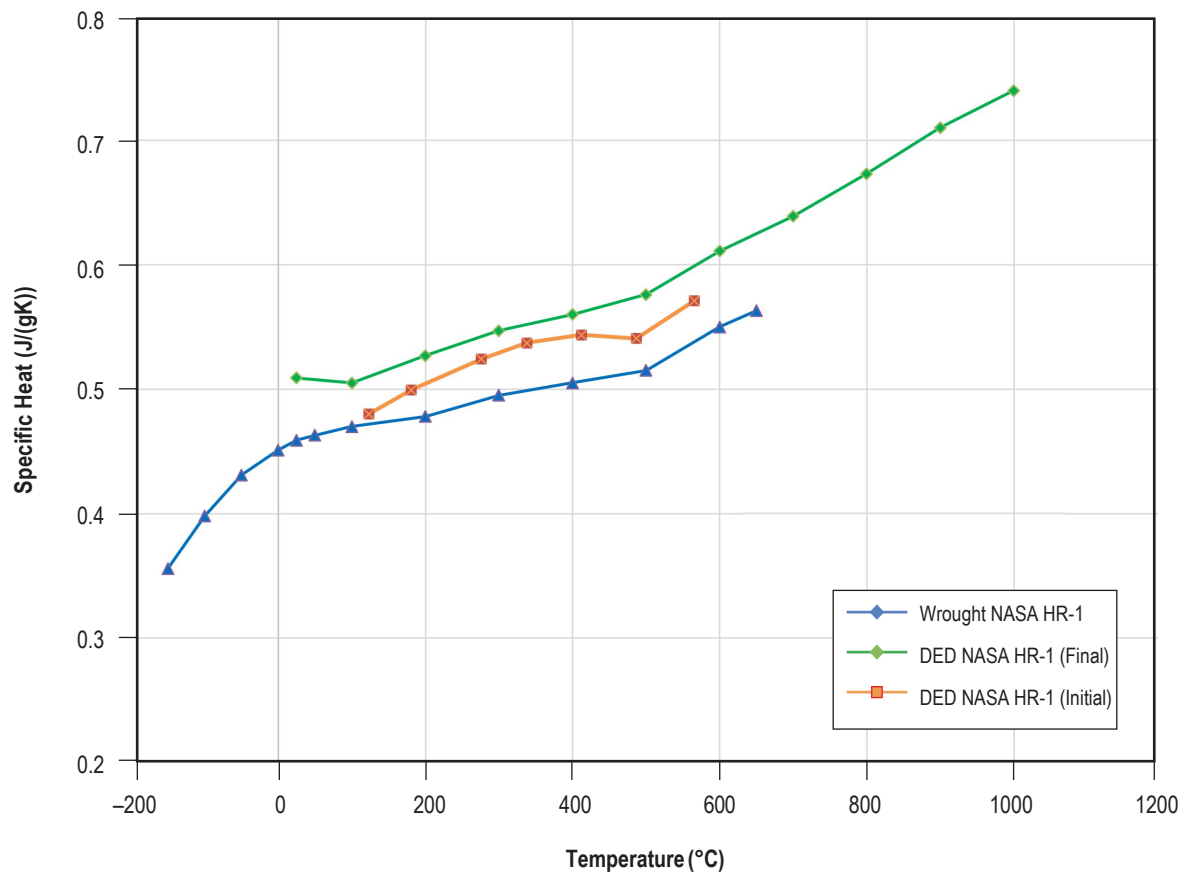


Figure 53. Comparison of specific heat capacity for LP-DED NASA HR-1 (initial composition), the wrought alloy, and the known literature data for LP-DED NASA HR-1 (final composition).<sup>65</sup>

The Neumann-Kopp rule was used to estimate heat capacity of LP-DED NASA HR-1 and the wrought alloy to see whether the predicted heat capacity agrees with the experimental data. The Neumann-Kopp rule expressed that the heat capacity of a compound  $A_xB_y$  (or an alloy) can be obtained by a linear-weighted combination of the  $C_P$  for the constituent elements forming  $A_xB_y$ .<sup>66,67</sup>

$$C_P(A_xB_y) = xC_P(A) + yC_P(B) \quad (9)$$

$C_P$  values of LP-DED NASA HR-1 and the wrought alloy were estimated using the Neumann-Kopp rule. The heat capacity values for the constituent elements were obtained from the thermodynamic properties published in a handbook.<sup>68</sup> As shown in Figure 54, LP-DED NASA HR-1 (final formulation) exhibits slightly higher calculated  $C_P$  values than LP-DED NASA HR-1 (initial formulation) and the wrought alloy. Overall, the difference in the computed  $C_P$  values among the three different NASA HR-1 compositions is small. The heat capacity values for LP-DED NASA HR-1 and the wrought alloy calculated using the Neumann–Kopp rule are in a good agreement with the trend of the experiential data from 100 to 500 °C. The  $C_P$  values obtained by Neumann Kopp rule begin to diverge from the experimental data above 500 °C. The computed  $C_P$  values of multi-component alloys can differ significantly from the experimental result due to the formation of compounds or precipitates at elevated temperatures that change the electronic structure. The discrepancy in the experimental  $C_P$  values for LP-DED NASA HR-1 and the wrought alloy (see Fig. 53) can be attributed to the differences in the chemical composition, micro-structure, the volume fraction of  $\gamma'$  precipitate, and the variability between different laboratories.

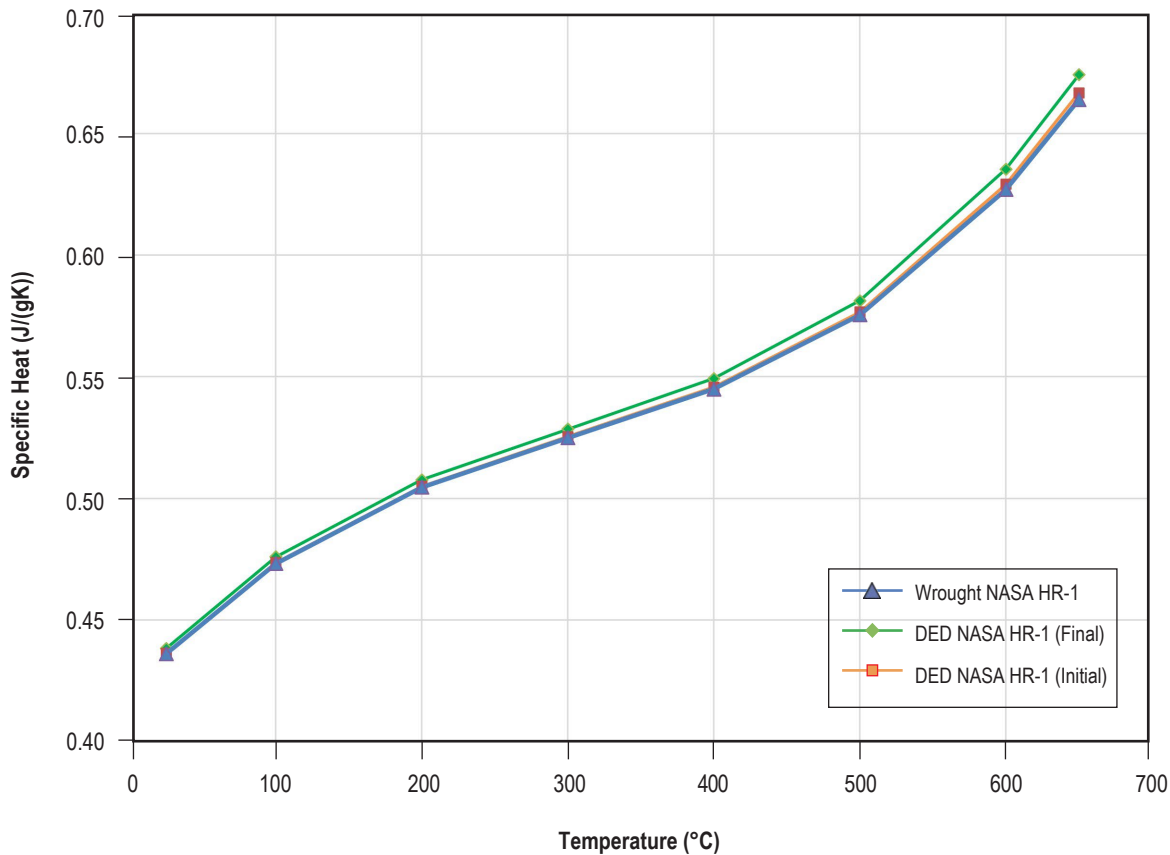


Figure 54. Comparison of predicted specific heat capacity obtained by using the mass-weighted Neumann-Kopp rule (Equation 9) for LP-DED NASA HR-1 (initial composition), the wrought alloy, and the known literature data for LP-DED NASA HR-1 (final composition).

Thermal conductivity determined at MSFC for LP-DED NASA HR-1 (initial composition) is in line with that of the wrought alloy but lower than the literature data for LP-DED NASA HR-1 (final formulation).<sup>6</sup> It is well known that alloying elements decrease the thermal conductivity of superalloys, and the thermal conductivity of superalloys is only 10 to 30% that of pure iron, or pure nickel due to the effect of extensive alloying.<sup>69,70</sup> Wrought NASA HR-1 has higher alloying elements content than the DED alloy, which is expected to contribute to lower values of thermal conductivity. In addition, LP-DED NASA HR-1 powder has tighter chemical composition control and lower impurity level than the wrought alloy. In metals, heat transfer is primarily carried by electrons and impurities will distort crystal lattice, impede electron movement, and reduce conductivity.<sup>71</sup> Comparing to the wrought alloy (having the highest alloying element content), the reduced alloying element content and lower impurity level maybe the reasons that contribute to increased thermal conductivity for LP-DED NASA HR-1. Although there are some variations in the measured thermophysical properties across different testing labs, it can be concluded that LP-DED NASA HR-1 (final formulation) has higher thermal conductivity than the wrought alloy. The increase in thermal conductivity can be attributed to the optimization of chemical composition and heat treatment LP-DED NASA HR-1 to obtain an optimal balance of key material properties.

### **3.5 Hardware manufacturing**

NASA, along with industry partners, has manufactured various components using the NASA HR-1 alloy. These components have been fabricated as manufacturing technology demonstrators (MTD's) and completed various hot-fire testing campaigns to demonstrate in the actual hydrogen environment (Fig. 55). Several components were deposited using 350W, 1070W, and 2620W power parameters using LP-DED. The lower power allows for thin walls deposited at approximately 1 mm generally used for channel wall nozzles. The higher power increases the deposition rates for thicker wall components that are often final machined and have limited internal features. The components demonstrated include powerhead half shells used for the RS-25 powerhead, manifolds for nozzles and chambers, transfer tubes, domes, and other pressure loaded components that are used in hydrogen environments. The LP-DED process was also used to build a MTD at 1.52 meter diameter and 1.78 meter height, approximately a 65% scale RS-25 channel wall nozzle (Fig. 55(c)).



Figure 55. Examples of various NASA HR-1 LP-DED components. (a) Domes for powerhead, (b) 35K-lbf nozzle with integral channels and welded manifolds, (c) Integral channel wall nozzle, (d) Powerhead half shell, (e) Hot-fire testing of regeneratively-cooled nozzle for LLAMA, (f) 7K-lbf nozzle for LLAMA, (g) High duty cycle testing of integral channel nozzle to 207 starts.

NASA has completed several test campaigns to demonstrate nozzles manufactured using the NASA HR-1 alloy with the LP-DED process. Testing of a 7000-lbf thrust regeneratively-cooled nozzle under the Long Life Additive Manufacturing Assembly (LLAMA) project (PK058) demonstrated 40 starts and 568 seconds in a LOX/Methane environment. The chamber pressure of this assembly was 750 psig and mixture ratio of about 3.2. Another test campaign (PJ062, LOX/Hydrogen) demonstrated high duty cycle hot-fire testing of a single NASA HR-1 LP-DED nozzle at 2000-lbf thrust and achieved 207 starts and almost 6,800 seconds at a chamber pressure of 1080 psig and mixture up to 7.4. This demonstrated temperatures exceeding 1400 °F on the nozzle hot-wall with a chamber pressure of approximately 1100 psig and mixture ratios up to 7.5 using LOX/hydrogen propellants. Additional NASA HR-1 LP-DED units were tested under this campaign with unique design features including a scalloped hotwall (tube-like) and spiral channels. All units performed as intended and met performance predictions. Two additional NASA HR-1 LP-DED channel wall nozzle units completed manufacturing and were tested at the 35000-lbf thrust level (PJ051, LOX/Hydrogen) and accumulated 8 starts and over 160 seconds. These units included a spiraled channel design and incorporated NASA HR-1 LP-DED manifolds. The deposition time for the nozzles were approximately 14 days and the manifolds were about 3 days each. NASA has manufactured multiple LP-DED components using NASA HR-1 and successfully tested accumulating over 280 starts and 8914 seconds in hydrogen environments on integral channel wall nozzles.

#### 4. CONCLUSIONS

(1) The Fe-Ni-Cr hydrogen-resistant NASA HR-1 alloy using additive manufactured (AM) laser powder directed energy deposition (LP-DED) has matured through process development, material characterization, and optimization of chemical composition and heat treatment. NASA HR-1 meets materials requirements for liquid rocket engine components and NASA has completed fabrication of several subscale and full-scale channel wall nozzles in LP-DED NASA HR-1 and completed hot-fire testing.

(2) The chemical composition of wrought NASA HR-1 was modified for AM using the PHACOMP method. An optimal composition (final formulation) has been determined by decreasing the overall Md value to retard precipitation of undesirable  $\eta$  phase and obtain an optimal balance of key materials properties. The optimized final formulation is shown below:

Alloy	Fe	Ni	Cr	Mo	V	W	Co	Ti	Al
LP-DED NASA HR-1 (Final Formulation)	41.20	34.00	14.60	1.80	0.30	1.60	3.80	2.40	0.25

(3) A new post-processing heat treatment has been successfully developed for LP-DED NASA HR-1. The optimized stress relief and homogenization treatments can effectively mitigate elemental segregation and produce highly recrystallized microstructure. The subsequent solution anneal and aging treatment help control precipitation kinetics of  $\gamma'$  and mitigate precipitation of undesirable grain boundary  $\eta$  phase. The optimized heat treatment process consists of the following steps:

- Stress relief at 1950 °F/1.5 hours with slow furnace cool,
- Homogenization at 2125 °F/6 hours with argon quench,
- Solution annealing at 1950 °F/1 hour with argon quench or faster,
- 2-step Aging at 1275 °F/16 hours + 1150 °F/16 hours (total time is 32 hours).

(4) Comparing with the wrought alloy, LP-DED NASA HR-1 exhibits lower strength, but significantly higher ductility and strain hardening capability. Strength reduction is part of the trade to obtain an optimal balance of key material properties when using AM. Ductility of LP-DED NASA HR-1 is slightly impacted when tensile tested at a very slow strain rate of 0.0001 in/in/min in hydrogen. However, the 2-step aged material remains very ductile and has more than 33% fracture elongation after tensile testing in hydrogen for 8–10 hours.

(5) The combined effects of chemical composition and heat treatment optimization enable high quality NASA HR-1 components to be fabricated via the LP-DED method. Changes

from the standard single step aging cycle to a lower temperature two step aging cycle alter the characteristics of LP-DED NASA HR-1 by decreasing the size and volume fraction of  $\gamma'$  precipitate and retarding precipitation of the detrimental  $\eta$  phase. As a result, LP-DED NASA HR-1 becomes more ductile and LCF resistant, which is important for low cycle fatigue critical components such as the LRE nozzles.

(6) The LCF performance of LP-DED NASA HR-1 in 2-step aged condition is comparable to that of the wrought alloy in ambient air. However, LP-DED NASA HR-1 performs much better than the wrought alloy when LCF testing is conducted in a high-pressure gaseous hydrogen environment. Due to its exceptional ductility and enhanced strain hardening capability, the LCF life of LP-DED NASA HR-1 is only slightly influenced by hydrogen, which is vital for the success and safety of LRE nozzles.

## REFERENCES

1. Gradl, P.; Tinker, D.; Park, A.; Mireles, O.; Garcia, M.; Wilkerson, R.; and McKinney, C.: Robust Metal Additive Manufacturing Process Selection and Development for Aerospace Components. *Journal of Materials Engineering and Performance*, Springer, 2021, <https://doi.org/10.1007/s11665-022-06850-0>.
2. Katsarelis, C.; Chen, P.S.; Gradl, P.R.; Protz, C.S.; Jones, Z.; Ellis, D.; and Evans L.: “Additive Manufacturing of NASA HR-1 for Liquid Engine Component Applications”, JANNFAF, United States, December 2019.
3. Gradl, P.R.; Teasley, T.; Protz, C.; Katsarelis, C.; and Chen, P.S.: “Process Development and Hot-fire Testing of Additively Manufactured NASA HR-1 for Liquid Rocket Engine Applications,” AIAA Propulsion and Energy Forum, 2021.
4. Chen, P.S.; Katsarelis, C.C.; Medders, W.M.; and Gradl, P.R.: “Segregation Evolution and Diffusion of Titanium in DED NASA HR-1”, NASA/TM 20210013649, May 2021.
5. Chen, P.S.; Panda, B.; and Bhat, B.N.: “NASA HR-1, A New Hydrogen Resistant Fe-Ni Base Superalloy”, *Hydrogen Effects in Materials*, A.W. Thompson and N.R. Moody (eds.), *Minerals, Metals, and Materials Society (TMS)*, 1994.
6. Gradl, P.R.: “Rapid Fabrication Techniques for Liquid Rocket Channel Wall Nozzles.” AIAA-2016-4771, Paper presented at 52nd AIAA/SAE/ASEE Joint Propulsion Conference, Salt Lake City, UT, July 27, 2016.
7. Gradl, P.R.; and Protz, C.S.: “Technology advancements for channel wall nozzle manufacturing in liquid rocket engines”, *Acta Astronautica*, Vol. 174, pp. 148–158, <https://doi.org/10.1016/j.actaastro.2020.04.067>, 2020.
8. Gradl, P.R.; Greene, S.E.; Brandsmeier, W.; and Johnston, I.: “Hot-fire Testing and Large-scale Deposition Manufacturing Development Supporting Liquid Rocket Engine Channel Wall Nozzle Fabrication,” Paper presented at 65th JANNFAF Propulsion Meeting/10th Liquid Propulsion Subcommittee. Long Beach, CA., May 21–24, 2018.
9. Kerstens, F.; Cervone, A.; and Gradl, P.R.: “End to end process evaluation for additively manufactured liquid rocket engine thrust chambers,” *Acta Astronautica*, 182, 454–465. <https://doi.org/10.1016/j.actaastro.2021.02.034>, 2021.
10. Gradl, P.R.; Greene, S.; Protz, C.S.; Bullard, B.; Buzzell, J.; Garcia, C.; Wood, J.; Osborne, R.; Hulka, J.; and Cooper, K.: “Additive Manufacturing of Liquid Rocket Engine Combustion

- Devices: A Summary of Process Developments and Hot-Fire Testing Results," 54th AIAA/SAE/ASEE Joint Propulsion Conference, *AIAA Propulsion and Energy Forum*, (AIAA 2018-4625). Cincinnati, OH., July 9–12, 2018.
11. Gradl, P.R.; Protz, C.S.; Cooper, K.; Garcia, C.; Ellis, D.; and Evans, L.: "GRCop-42 Development and Hot-fire Testing using Additive Manufacturing Powder Bed Fusion for Channel-cooled Combustion Chambers," 55th AIAA/SAE/ASEE Joint Propulsion Conference, *AIAA Propulsion and Energy Forum*, Indianapolis, IN., AIAA-2019-4228, August 19–21, 2019.
  12. Gradl, P.R.; Protz, C.S.; and Wammen, T.: "Additive Manufacturing Development and Hot-fire Testing of Liquid Rocket Channel Wall Nozzles using Blown Powder Directed Energy Deposition Inconel 625 and JBK-75 Alloys," 55th AIAA/SAE/ASEE Joint Propulsion Conference, *AIAA Propulsion and Energy Forum*, Indianapolis, IN., AIAA-2019-4362, August 19–21, 2019.
  13. Gradl, P.R.; Protz, C.S.; Fikes, J.; Clark, A.; Evans, L.; Miller, S.; Ellis, D.L.; and Hudson, T.: "Lightweight Thrust Chamber Assemblies using Multi-Alloy Additive Manufacturing and Composite Overwrap," *AIAA Propulsion and Energy Forum*. Virtual. (2020). AIAA-2020-3787, August 24–26, 2020.
  14. David, S.A.; Siefert, J.A.; DuPont J.N.; and Shingledecker, P.: "Weldability and Weld Performance of Candidate Nickel Based Superalloys for Advanced Ultrasupercritical Fossil Power Plants Part I: Fundamentals", *Science and Technology of Welding and Joining*, Vol. 20, No. 7, pp. 532 – 552, 2015.
  15. Shaikh, A.S.: "Development of a  $\gamma'$  Precipitation Hardening Ni-Base Superalloy for Additive Manufacturing," Thesis for Master of Science in Materials Engineering, Chalmers University of Technology, July 2018.
  16. Neghlani, P.K.: "SLM additive manufacturing of Alloy 718 Effect of process parameters on microstructure and properties," M.S. Thesis, University West, pp. 48, doi:10.13140/RG.2.2.25434.64963, August 2016.
  17. Fencheng, L.; Xin, L.; Gaolin, Y.; et al.: "Recrystallization and its influence on microstructures and mechanical properties of laser solid formed nickel base superalloy Inconel 718," *Rare Metals*, Vol. 30, No. 1, pp. 433–438, doi:10.1007/s12598-011-0319-0, March 2011.
  18. Zhang, F; Levine, L.E.; Allen, A.J.; et al.: "Effect of heat treatment on the microstructural evolution of a nickel-based superalloy additive-manufactured by laser powder bed fusion," *Acta Materialia*, Vol. 152, pp. 200–214, June 2018.
  19. Cao, J; Liu, F; Lin, X.; et al.: "Effect of overlap rate on recrystallization behaviors of Laser Solid Formed Inconel 718 superalloy," *Optics & Laser Technology*, Vol. 45, pp. 228–235, February 2013.

20. Bouse, G.K.: “Eta (h) and Platelet Phases in Investment Cast Superalloys,” pp. 163–172, Superalloys, Minerals, Metals, and Materials Society (TMS), 1996.
21. Seifollahi, M.; Kheirandish, S.; Razavi, S.H.; and Abbasi, S.M.: “The Precipitation of h phase in an Fe-Ni-Based Superalloy with Different Ti/Al Ratios”, pp. 1– 6, *International Journal of Materials Research*, April 2013.
22. Halchak, J.A.; Cannon, J.L.; and Brown, C.D.: “Chapter 12: Materials for Liquid Propulsion Systems,” DOI:10.2514/5.9781624104893.0641.0698Corpus ID: 4255669.
23. Song, J.; and Sun, B.: “Thermal-structural analysis of regeneratively cooled thrust chamber wall in reusable LOX/Methane rocket engines,” *Chinese Journal of Aeronautics*, Vol. 30, Issue 3, pp. 1043-1053, June 2017.
24. Babu1, A.; Asraff, A.K.; and Philip, N.: “Fatigue Life Prediction of a Rocket Combustion Chamber,” *IOSR Journal of Mechanical and Civil Engineering (IOSR-JMCE)*, e-ISSN: 2278-1684,p-ISSN: 2320-334X, Vol. 11, Issue 5, Ver. II, pp. 12–20, Sep–Oct. 2014.
25. Cheng, C.; Yibai, W.; Yu, L.; Dawei, L.; and Xingyu, L.: “Thermal-structural response and low-cycle fatigue damage of channel wall nozzle,” *Chinese Journal of Aeronautics*, Vol. 26, Issue 6, pp. 1449–1458, December 2013.
26. Lee, J.A.: “Hydrogen Embrittlement”, NASA Technical Memorandum, 2016.
27. Menoua, E.; Ramec, J.; Desgrangesc, C.; Ramsteinb, G.; and Tancreta, F.: “Computational design of a single crystal nickel-based superalloy with improved specific creep endurance at high temperature,” *Computational Materials Science*, Vol. 170, 109194, <https://doi.org/10.1016/j.commatsci.2019.109194>, December 2019.
28. Morinaga, M.; Yukawa, N.; Ezaki, H.; and Adachi, H.: “Solid Solubilities in Transition- Metal-Based f.c.c. Alloys.” *Philosophical Magazine A*, Vol. 51, No. 2, pp. 223–246. doi:10.108%1 418610.1985.12069159, 1985.
29. Morinaga, M.; Murata, Y.; and Yukawa, H.: “Recent Progress in Molecular Orbital Approach to Alloy Design,” 2004.
30. Morinaga, M.; and Yukawa, H.: “Alloy Design with the Aid of Molecular Orbital Method.” *Bulletin of Materials Science*. doi:10.1007/BF02747420, 1997.
31. Morinaga, M.; Yukawa, N.; and Adachi, H.: “Alloying Effect on the Electronic Structure of Ni<sub>3</sub>Al ( $\gamma'$ )”, *Journal of the Physical Society of Japan*, Vol. 53, No. 2, pp. 653–663, 1984.
32. Morinaga, M.; Yukawa, N.; Adachi, H.; and Ezaki, H.: “Superalloys,” E.A. Loria (eds), *The Minerals, Metals & Materials Society*, Warrendale, PA, pp. 523–532, 1984.

33. Morinaga, M.; Yukawa, N.; and Adachi, H.: “Alloying effect on the electronic structure of BCC Fe,” *Journal of Physics F: Metal Physics*, Vol. 15, No. 5, pp. 1071–1084, 1985.
34. Ducki, K.J.: “Analysis of the Precipitation and Growth Processes of the Intermetallic Phases in an Fe-Ni superalloy,” *Superalloys*, M. Aliofkhazraei (ed.), InTechOpen, doi: 10.5772/61159, November 2015.
35. Sheikh, S.; Klement, U.; and Guo S.: “Predicting the solid solubility limit in high-entropy alloys using the molecular orbital approach,” *Journal of Applied Physics*, Vol. 118, No. 19402 doi:10.1063/1.4935620, 2015.
36. Lee, J.A.: ”A Theory for Hydrogen Embrittlement of Transition Metals and Their Alloys”, *Hydrogen Effects in Materials*, A.W. Thompson and N.R. Moody (eds.), Minerals, Metals, and Materials Scity (TMS), 1994.
37. Lee, J.A.: “Effects of the Density of States on the Stacking Fault Energy And Hydrogen Embrittlement of Transition Metals And Alloys,” Effects of Hydrogen on Materials Proceedings of the International Hydrogen Conference, B. Somerday, P. Sofronis, R. Jones, (eds.), pp. 678–685, 2008.
38. Morinaga, M.; Yukawa, N.; Adachi, H.; and Ezaki, H.: “New PHACOMP and Its Application to Alloy Design,” *Superalloys*, 1984, M. Gell (eds.), MC.S. Kortovich, R.H. Bricknell, W. B. Kent and J.F. Radavich, The Metallurgical Society of AIME, pp. 523–532, 1984.
39. “TTP Development for DED NASA HR-1,” Internal Research, NASA Marshall Space Flight Center, Huntsville, AL.
40. “Progress in Thermal Process Development for AM NASA HR-1,” Internal Research, NASA Marshall Space Flight Center, Huntsville, AL.
41. Richard, B.F.: “Age-Hardenable Superalloys,” *Advanced Materials & Processes*, Vol. 163, No. 6, pp. 37–42, June 2005.
42. Papadaki, C.; Li, W.; and Korsunsky, A.M.: “On the Dependence of  $\gamma'$  Precipitate Size in a Nickel-Based Superalloy on the Cooling Rate from Super-Solvus Temperature Heat Treatment,” *Materials (Basel)*, Vol. 11, No. 9:1528, 10 pp., doi:10.3390/ma11091528, September 2018.
43. Bassini, E.; Cattano, G.; Marchese, G.; et al.: “Study of the Effects of Aging Treatment on Astroloy Processed via Hot Isostatic Pressing,” *Materials*, Vol. 12, No. 9:1517, pp. 17, doi:10.3390/ma12091517, May 2019.
44. “Two-Step Aging Treatment Development for DED NASA HR-1,” Internal Research, NASA Marshall Space Flight Center, Huntsville, AL.

45. Nandy, S.; Sekhar, A.P.; Kar, T.; Ray, K.K.; and Das, D.: "Influence of ageing on the low cycle fatigue behaviour of an Al–Mg–Si alloy," *Philosophical Magazine*, <https://doi.org/10.1080/14786435.2017.1322729>, 2017.
46. Saravanan, K.; Chakravadhanula, V.S.K.; Manwatkar, S.K.; Narayana, S.V.S.; and Narayanan, P.R.: "Dynamic Strain Aging and Embrittlement Behavior of IN718 During High-Temperature Deformation," *Metallurgical and Materials Transactions*, Vol. 51A, pp. 5691–5703, November 2020.
47. Cui, C.Y.; Tian, C.G.; Zhou, Y.Z.; Jin, T.; and Sun, X.F.: "Dynamic Strain Aging in Ni Base Alloys with Different Stacking Fault Energy," *Superalloys 2012: 12<sup>th</sup> International Symposium on Superalloys*.
48. Ottersböck, M.J.; Leitner, M.; Stoschka, M.; and Maurer, W.: "Crack Initiation and Propagation Fatigue Life of Ultra High-Strength Steel Butt Joints," *Appl. Sci.*, 9, 4590; doi:10.3390/app9214590, 2019.
49. El-sayed, H.M.; Lotfy, M.; El-din Zohny, H.N.; and Ria, H.S.: "Prediction of fatigue crack initiation life in railheads using finite element analysis," *Ain Shams Engineering Journal*, Vol. 9, Issue 4, pp. 2329–2342, December 2018.
50. Kim Y.; and Hwang, W.: "High-Cycle, Low-Cycle, Extremely Low-Cycle Fatigue and Monotonic Fracture Behaviors of Low-Carbon Steel and Its Welded Joint," *Materials*, 12, 4111; doi:10.3390/ma12244111, 2019.
51. Zhang1, Z.; Obasis, G.; Morana, R.; and Preuss, M.: "Hydrogen assisted crack initiation and propagation in a nickel-based superalloy," *Acta Materialia*, Vol. 113, pp. 272–283. <https://doi.org/10.1016/j.actamat.2016.05.003>, 2006.
52. Li, X.; Li, Q.; Wang, T.; and Zhang, J.; "Hydrogen-assisted failure of laser melting additive manufactured IN718 superalloy," *Corrosion Science* 160(Part 3):108171, DOI:10.1016/j.corsci.2019.108171, 2019.
53. Raoa, G.S.; Yagodzinskyy, Y.; Quea, Z.; Spätiaga, P.; and Seifert, H.P.: "Study on hydrogen embrittlement and dynamic strain ageing on low-alloy reactor pressure vessel steels," *Journal of Nuclear Materials*, Vol. 556, 153161, December 1, 2021.
54. Tugluca, I.B.; Koyama, M.; Shimomura, Y.; Bal, B.; Canadinc, D.; Akiyama, E.; and Tsuzaki, K.: "Lowering Strain Rate Simultaneously Enhances Carbon- and Hydrogen-Induced Mechanical Degradation in an Fe-33Mn-1.1C Steel," *Metallurgical and Materials Transactions*, Vol. 50A, pp. 1137, March 2019.
55. Wada, Y.; Ishigaki, R.; Tanaka, Y.; Iwadate, T.; and Ohnishi, K.: "Evaluation of metal materials for hydrogen fuel stations," *Proceedings of the 1992 Annual Meeting of JSME/MMD 2005*, DOI:10.1299/jsmezairiki.2005.0\_185, November 2005.

56. Michler, T.; Wackermann, K.; and Schweizer, F.: "Review and Assessment of the Effect of Hydrogen Gas Pressure on the Embrittlement of Steels in Gaseous Hydrogen Environment," *Metals*, Vol. 11, Issue 4, pp. 637, <https://doi.org/10.3390/met11040637>, 2021.
57. Li, X.; Li, Q.; Wang, T.; and Zhang, J.: "Hydrogen-assisted failure in Inconel 718 fabricated by laser powder bed fusion: The role of solidification substructure in the embrittlement," *Scripta Materialia*, Vol. 207, 114308, January 15, 2022.
58. Marchi, C.S.: "Gaseous Hydrogen Embrittlement of High Performance Metals in Energy System," *Gaseous Hydrogen Embrittlement of Materials in Energy Technologies Mechanisms, Modelling and Future Developments*, Volume 1 in *Woodhead Publishing Series in Metals and Surface Engineering*, pp. 471–484, 2012.
59. Kagay, B.J.: "Hydrogen Embrittlement Testing of Alloy 718 for Oil and Gas Application," Masters Theses, Colorado School of Mines, <http://hdl.handle.net/11124/170301>, 2016.
60. Kim, Y.; Kim, Y.; Kim, D.; Kim, S.; Nam, W.; and Choe, H.: "Effects of Hydrogen Diffusion on the Mechanical Properties of Austenite 316L Steel at Ambient Temperature," *Materials Transactions*, Vol. 52, No. 3, pp. 507–513, 2011.
61. Cook, B.M.: "Structural Assessment for JBK-75 Nozzle," Internal Research, NASA Marshall Space Flight Center, Huntsville, AL.
62. Puydebois, S.; Oudriss, A.; Bernard, P.; Briottet, L.; and Feaugas, X.: "Hydrogen Effect on the Fatigue Behavior of LBM Inconel 718," MATEC Web of Conferences 165, 02010, <https://doi.org/10.1051/matecconf/201816502010>, 2018.
63. Bucci, R.J.; Nordmark, G.; and Starke, Jr., E.A.: "Selecting Aluminum Alloys to Resist Failure by Fracture Mechanisms," ASM Handbook, Volume 19: Fatigue and Fracture, 1996.
64. Chen, P.S.; and Mitchell, M.: Aerospace Structural Metals Handbook, August 2005.
65. Zeng, C.; Guo, S.; Gradl, P.; and Belcher, T.: Thermophysical Properties of Select AM Alloys. In *Metal Additive Manufacturing for Propulsion Applications*, Reston, VA: American Institute of Aeronautics and Astronautics, Inc., pp. 775–824. <https://doi.org/10.2514/5.9781624106279.0775.0824>, 2022.
66. Grimvall, G.: "Thermophysical Properties of Materials," The Royal Institute of Technology Stockholm, Sweden, ISBN 978-0-444-82794-4, 1999.
67. Gupta, A.; Tas, B.; Korbmacher, D.; Dutta, B.; Neitzel, Y.; Grabowski, B.; Hickel, T.; Esin, V.; Divinski, S.V.; Wilde, G.; and Neugebauer, J.: "A Combined Experimental and First-Principles Based Assessment of Finite-Temperature Thermodynamic Properties of Intermetallic Al<sub>3</sub>Sc," *Materials*, 14, 1837. <https://doi.org/10.3390/ma14081837>, 2021.

68. Stull, D.R.; and Sinke, G.C.: "Thermodynamic Properties of the Elements," Vol. 18, American Chemistry Society, January 1, 1956.
69. Zielińska, M.; Yavorska, M.; Poręba, M.; and Sieniawski, J.: "Thermal properties of cast nickel based superalloys," Archives of Materials Science and Engineering, Vol. 44, Issue 1, pp. 35–38, July 2010.
70. Sims C.; and Hagel, W.C.: "The Superalloys - Vital High Temperature Gas Turbine Materials for Aerospace and Industrial Power," John Wiley & Sons, 1972.
71. Wee, S.; Do, J.; Kim, K.; Lee, C.; Seok, C.; Choi, B.G.; Choi, Y.; and Kim, W.: "Review on Mechanical Thermal Properties of Superalloys and Thermal Barrier Coating Used in Gas Turbines," Appl. Sci., 10, 5476; doi:10.3390/app10165476, 2020.

National Aeronautics and  
Space Administration  
IS63

**George C. Marshall Space Flight Center**  
Huntsville, Alabama 35812